

MULTI-CHANNEL ANALYSIS OF SURFACE WAVES (MASW) IN KARST
TERRAIN: IMPLICATIONS FOR DETECTING SUBSIDENCE FEATURES AND
LINEAMENTS

by

ELIAS HORRY PARKER JR.

(Under the Direction of Robert B. Hawman)

ABSTRACT

Multi-Channel Analysis of Surface Waves (MASW) has been employed in covered, karst terrain near Albany, GA to investigate potential subsidence features and fracture trends within bedrock. Surface wave data were obtained with a 24-channel recording system along seven parallel lines and two perpendicular cross-lines. Active-source (hammer) and passive-source (moving van) seismic surveys were conducted to image depth ranges of 4, 12, and 23 meters. The steep shear-wave velocity gradient at 9-10 meters is interpreted as the soil-bedrock interface, in agreement with coincident borehole data. Velocities of soil overburden range from 150-350 m/s, and velocities for fractured limestone bedrock range from 350-700 m/s. Distinct changes in apparent velocity across certain shot gathers are consistent with anomalous zones identified on the 2-D shear-wave velocity models. The low-velocity zone at the intersection of Lines A and Z is interpreted to be a potential collapse feature associated with a north-south trending fracture zone.

INDEX WORDS: MASW, karst, subsidence, lineament, Ocala limestone

MULTI-CHANNEL ANALYSIS OF SURFACE WAVES (MASW) IN KARST
TERRAIN: IMPLICATIONS FOR DETECTING SUBSIDENCE FEATURES AND
LINEAMENTS

by

ELIAS HORRY PARKER JR.

B.S., The University of the South, 2002

A Thesis Submitted to the Graduate Faculty of The University of Georgia in Partial
Fulfillment of the Requirements for the Degree

MASTER OF SCIENCE

ATHENS, GEORGIA

2010

© 2010

ELIAS HORRY PARKER JR.

All Rights Reserved

MULTI-CHANNEL ANALYSIS OF SURFACE WAVES (MASW) IN KARST
TERRAIN: IMPLICATIONS FOR DETECTING SUBSIDENCE FEATURES AND
LINEAMENTS

by

ELIAS HORRY PARKER JR.

Major Professor: Robert B. Hawman

Committee: John Dowd
Ervan Garrison

Electronic Version Approved:

Maureen Grasso
Dean of the Graduate School
The University of Georgia
August 2010

ACKNOWLEDGEMENTS

I am very grateful to Rob Hawman for his insight, enthusiasm, and guidance throughout the course of this project.

I would also like to thank the following individuals for their contributions to the study: Woody Hicks for arranging access to the Albany Water, Gas, and Light (AWGL) well field; Gary Morefield (AWGL) and Lee Daniel (AWGL) for their assistance at the site; Debbie W. Gordon (USGS) for providing site information including borehole logs, sinkhole coordinates, and maps; and Will Stephens and Brian Price (UGA) for their invaluable field assistance.

Financial support was provided by the Geological Society of America, the Wheeler-Watts fund (UGA), the Gilles and Bernadette Allard fund (UGA), and the Joseph W. Berg fund (UGA). The UGA Department of Geology also provided transportation for the trips to Albany.

TABLE OF CONTENTS

	Page
ACKNOWLEDGEMENTS	<i>iv</i>
LIST OF TABLES	<i>viii</i>
LIST OF FIGURES	<i>ix</i>
CHAPTER	
1 INTRODUCTION	1
Importance of karst and objectives of the study	1
Geophysical investigations of karst	2
Geologic setting of the study area.....	4
Multi-channel analysis of surface waves (MASW).....	6
Field Acquisition.....	10
Active Survey.....	11
Passive survey	12
Typical Processing Flow	12
2 SHEAR-WAVE VELOCITY MODELS - LINES A-G	23
Data Processing: Dispersion curve picking and muting procedures.....	23
Conservative Models: Lines A-G	26
Line A	27
Line B.....	27
Line C.....	28

	Line D	29
	Line E.....	30
	Line F.....	31
	Line G	33
	Comparison of models with topographic profiles.....	33
3	ALTERNATIVE SHEAR-WAVE VELOCITY MODELS FOR LINE A: EXPERIMENTATION WITH SPATIAL WINDOWING AND THE USE OF HALF-SPREADS.....	67
	Model 1A	67
	Model 2A	69
	Model 3A	70
	Model 4A	72
	Model 5A	72
	Model 6A	73
	Model 7A	74
	Model 8A	75
	Discussion: Line A.....	75
4	SHEAR-WAVE VELOCITY MODELS: LINES Y AND Z	95
	Line Y	95
	Line Z.....	95
	Comparison of models with topographic profiles.....	96
5	HALF-SPREAD ANALYSIS: LINES A-G AND Y-Z.....	105

6	DISCUSSION	113
	Processing issues and recommendations for future work	113
	Shear-wave velocities for geologic materials	115
	Potential subsidence features	116
	Fracture zones and lineaments	117
	Regional joint sets and fracture mechanics	119
7	CONCLUSIONS	126
	REFERENCES	128
	APPENDICES	
A	Processing Details	137
B	1-D shear-wave velocity models for intersection points	142

LIST OF TABLES

	Page
Table 1.1: Inversion Parameters	14
Table 1.2: Active-source seismic lines	14
Table 1.3: Passive-source seismic lines	15
Table 1.4: Recording parameters	15
Table 2.1: Display parameters for conservative models.....	34
Table 2.2: Processing parameters for conservative models	34
Table 3.1: Display parameters for Line A	77
Table 3.2: Processing parameters for Line A.....	77
Table 3.3: Spatial windowing: Analyzing subsets of traces	78
Table 4.1: Intersection points of seismic lines.....	97
Table 6.1: Interpreted shear-wave velocities for geologic materials	120

LIST OF FIGURES

	Page
Figure 1.1: Dougherty Plain physiographic province	16
Figure 1.2: Extent of the Upper Floridan Aquifer in the southeastern United States	16
Figure 1.3: Stratigraphic column for the Dougherty Plain physiographic province	17
Figure 1.4: Borehole log for Well #44 obtained from the USGS Water Science Center in Atlanta, Georgia	18
Figure 1.5: Sinkhole formation at the Albany WGL well field	19
Figure 1.6: Group velocity (U) and phase velocity (V) for the fundamental mode and two higher mode surface waves	19
Figure 1.7: Seismic lines in Albany, GA	20
Figure 1.8: Schematic diagram of array geometry for the roll-along seismic survey	21
Figure 1.9: Processing flow diagram	22
Figure 2.1: Typical frequency spectra for shot gathers	35
Figure 2.2: Shot gathers for STA 52 on Line G	36
Figure 2.3: Overtone images (amplitude contour plots) and dispersion curve picks (squares) for STA 52 on Line G	37
Figure 2.4: 1-D shear-wave velocity models for STA 52 on Line G	38
Figure 2.5: Alternate models for Line G using different frequency ranges for dispersion curve picking	39
Figure 2.6: Active-source models for Lines A (VE = 1.3), B (VE = 1.2),	

and C (VE = 1.2).....	40
Figure 2.7: Active-source models for Lines D (VE = 1.1), E (VE = 1.2), F (VE = 1.1), and G (VE = 1.2).....	41
Figure 2.8: Passive-source models for Lines A (VE = 0.7), B (VE = 0.9), and C (VE = 0.7).....	42
Figure 2.9: Passive-source models for Lines D (VE = 0.8), E (VE = 0.7), F (VE = 0.8), and G (VE = 0.8).....	43
Figure 2.10: Active-source (A) and passive-source (B) models for Line A.....	44
Figure 2.11: Active-source (A) and passive-source (B) models for Line B.....	45
Figure 2.12: Active-source (A) and passive-source (B) models for Line C.....	45
Figure 2.13: Active-source (A) and passive-source (B) models for Line D.....	46
Figure 2.14: Active-source (A) and passive-source (B) models for Line E.....	46
Figure 2.15: Active-source (A) and passive-source (B) models for Line F.....	47
Figure 2.16: Active-source (A) and passive-source (B) models for Line G.....	47
Figure 2.17: Active-source overtone image (amplitude contour plot) and dispersion curve picks (squares) for STA 19 on Line B.....	48
Figure 2.18: Overtone images (amplitude contour plots) and dispersion curve picks (squares) for STA 37 on Line B.....	49
Figure 2.19: Overtone images (amplitude contour plot) and dispersion curve picks (squares) for STA 69 on Line B.....	50
Figure 2.20: Overtone images (amplitude contour plots) and dispersion curve picks (squares) for STA 39 on Line C.....	51

Figure 2.21: Overtone images (amplitude contour plots) and dispersion curve picks (squares) for STA 89 on Line C.....	52
Figure 2.22: Passive-source overtone image (amplitude contour plot) and dispersion curve picks (squares) for STA 63 on Line C	53
Figure 2.23: Overtone images (amplitude contour plots) and dispersion curve picks (squares) for STA 45 on Line D	54
Figure 2.24: Overtone images (amplitude contour plots) and dispersion curve picks (squares) for STA 31 on Line D	55
Figure 2.25: Passive-source overtone image (amplitude contour plot) and dispersion curve picks (squares) for STA 35 on Line D	56
Figure 2.26: Active-source overtone image (amplitude contour plot) and dispersion curve picks (squares) for STA 63 on Line E	56
Figure 2.27: Active-source overtone image (amplitude contour plot) and dispersion curve picks (squares) for STA 65 on Line E	57
Figure 2.28: Active-source overtone image (amplitude contour plot) and dispersion curve picks (squares) for STA 53 on Line E	57
Figure 2.29: (A) Passive-source overtone image (amplitude contour plot) and dispersion curve picks (squares) for STA 67 on Line E. (B) 1-D shear-wave velocity model for STA 67 on Line E.....	58
Figure 2.30: (A) Passive-source overtone image (amplitude contour plot) and dispersion curve picks (squares) for STA 39 on Line E; (B) 1-D shear-wave velocity model for STA 39 on Line E.....	59
Figure 2.31: Passive-source models for Line F	60

Figure 2.32: Passive-source overtone images (amplitude contour plots) and dispersion curve picks (squares) for STA 55 on Line F	61
Figure 2.33: (A) Passive-source overtone record (amplitude contour plot) and dispersion curve picks (squares) for STA 65 on Line G; (B) 1-D shear-wave velocity model for STA 65 on Line G	62
Figure 2.34: Active-source model (VE = 1.3) and topographic profile (VE = 5.3) for Line A.....	63
Figure 2.35: Active-source model (VE = 1.2) and topographic profile (VE = 5.3) for Line B.....	64
Figure 2.36: Active-source model (VE = 1.2) and topographic profile (VE = 5.3) for Line C.....	64
Figure 2.37: Active-source model (VE = 1.04) and topographic profile (VE = 5.3) for Line D.....	65
Figure 2.38: Active-source model (VE = 1.2) and topographic profile (VE = 5.3) for Line E	65
Figure 2.39: Active-source model (VE = 1.08) and topographic profile (VE = 5.3) for Line F	66
Figure 2.40: Active-source model (VE = 1.2) and topographic profile (VE = 5.3) for Line G.....	66
Figure 3.1: Alternative models for Line A (1A-3A).....	79
Figure 3.2: Alternative models for Line A (4A-5A).....	80
Figure 3.3: Alternative passive-source models for Line A using different processing parameters for dispersion curve picking (VE = 0.6).....	81

Figure 3.4: Shot gathers for STA 152 on Line A.....	82
Figure 3.5: Active-source overtone image (amplitude contour plot) and dispersion curve picks (squares) for STA 152 on Model 1A without pre-processing (muting).....	83
Figure 3.6: Active-source overtone image (amplitude contour plot) for STA 28 showing the fundamental mode and a higher-mode surface-wave merged together	83
Figure 3.7: Active-source overtone image (amplitude contour plot) for STA 83 on Line A showing a branching effect at high frequencies (30-90 Hz).....	84
Figure 3.8: Active-source overtone image (amplitude contour plot) for STA 96 on Line A showing the disruption of the fundamental mode signal at low frequencies (10-30 Hz).....	84
Figure 3.9: Active-source overtone images (amplitude contour plots) and dispersion curve picks (squares) for STA 48 Line A	85
Figure 3.10: Active-source overtone images (amplitude contour plots) and dispersion curve picks (squares) for STA 100 for Line A	86
Figure 3.11: Active-source overtone images (amplitude contour plots) and dispersion curve picks (squares) for STA 117 on Line A	87
Figure 3.12: Active-source overtone image (amplitude contour plot) and dispersion curve picks (squares) for STA 125 on Line A	88
Figure 3.13: Active-source overtone images (amplitude contour plots) and dispersion curve picks (squares) for STA 138 on Line A	89
Figure 3.14: Active-source overtone images (amplitude contour plot) and dispersion curve picks (squares) for STA 152 on Line A	90
Figure 3.15: Shot gather and overtone record for STA 82 on Line A	91

Figure 3.16: (A) Passive-source shot gather for STA 65 on Line A. (B) Passive-source shot gather for STA 65 on Line A showing only the first 1000 ms of the record	92
Figure 3.17: Passive-source overtone image (amplitude contour plot) and dispersion curve picks (squares) for STA 65 (Model 6A)	93
Figure 3.18: Passive-source overtone image (amplitude contour plot) and dispersion curve picks (squares) for STA 65 (Model 7A)	93
Figure 3.19: Passive-source overtone image (amplitude contour plot) and dispersion curve picks (squares) for STA 65 (Model 8A)	94
Figure 4.1: (A) Active-source (VE = 3.5) and (B) passive-source (VE = 2.2) models for Line Y	98
Figure 4.2: (A) Active-source (VE = 1.3) and (B) passive-source (VE = 0.78) models for Line Z	99
Figure 4.3: Shot gathers across the LVZ on Line Z.....	100
Figure 4.4: Shot gather for STA 82 on Line A	101
Figure 4.5: 1-D shear-wave velocity models for the intersection of Line A and Z	102
Figure 4.6: Active-source model (VE = 3.5) and topographic profile (VE = 10.5) for Line Y	103
Figure 4.7: Active-source model (VE = 1.3) and topographic profile (VE = 5.3) for Line Z	104
Figure 5.1: Active-source models for Line A; (A) full spread (VE = 1.3), (B) half spread (VE = 4.5)	107
Figure 5.2: Active-source models for Line B; (A) full spread (VE = 1.1), (B) half spread (VE = 4.9)	108

Figure 5.3: Active-source models for Line C; (A) full spread (VE = 1.1), (B) half spread (VE = 4.6)	108
Figure 5.4: Active-source models for Line D; (A) full spread (VE = 1.1), (B) half spread (VE = 4.9)	109
Figure 5.5: Active-source models for Line E; (A) full spread (VE = 1.3), (B) half spread (VE = 5.7)	109
Figure 5.6: Active-source models for Line F; (A) full spread (VE = 1.1), (B) half spread (VE = 4.7)	110
Figure 5.7: Active-source models for Line G; (A) full spread (VE = 1.2), (B) half spread (VE = 4.6)	110
Figure 5.8: Active-source models for Line Y; (A) full spread (VE = 3.4), (B) half spread (VE = 14.2)	111
Figure 5.9: Active-source models for Line Z; (A) full spread (VE = 1.3), (B) half spread (VE = 5.8)	112
Figure 6.1: (A) Active-source overtone image (amplitude contour plot) and dispersion curve picks (squares) for STA 131 on Line A. (B) Passive-source overtone image (amplitude contour plot) and dispersion curve picks (squares) for STA 131 on Line A	121
Figure 6.2: (A) Active-source overtone record (amplitude contour plot) and dispersion curve picks (squares) for STA 30 on Line A. (B) Passive-source overtone image (amplitude contour plot) and dispersion curve picks (squares) for STA 31 on Line A	122

Figure 6.3: (A) Active-source overtone image (amplitude contour plot) and dispersion curve picks (squares) for STA 79 within the LVZ on Line A. (B) Passive-source overtone image (amplitude contour plot) and dispersion curve picks (squares) for STA 79 within the LVZ on Line A.....	123
Figure 6.4: Shear-wave velocity models for Lines A-G with arrows indicating apparent trends in bedrock topography.....	124
Figure 6.5: Suspected fracture trends based on sinkhole formation and the low-velocity zone at the intersection of Line A and Z.....	125
Figure A1: Shot gather showing noisy first trace	137
Figure A2: Overtone images (amplitude contour plots) generated with Dispersion 1	140
Figure A3: Overtone images (amplitude contour plots) generated with Dispersion 2	141
Figure B1: 1-D shear-wave velocity models for the intersection of Lines Y and C.....	143
Figure B2: 1-D shear-wave velocity models for the intersection of Lines Y and B.....	144
Figure B3: 1-D shear-wave velocity models for the intersection of Lines Y and A	145
Figure B4: 1-D shear-wave velocity models for the intersection of Lines Y and D	146
Figure B5: 1-D shear-wave velocity models for the intersection of Lines Y and E.....	147
Figure B6: 1-D shear-wave velocity models for the intersection of Lines Y and F	148
Figure B7: 1-D shear-wave velocity models for the intersection of Lines Y and G	149
Figure B8: 1-D shear-wave velocity models for the intersection of Lines Z and C.....	150
Figure B9: 1-D shear-wave velocity models for the intersection of Lines Z and B.....	151
Figure B10: 1-D shear-wave velocity models for the intersection of Lines Z and A.....	152

Figure B11: 1-D shear-wave velocity models for the intersection of Lines Z and D.....153
Figure B12: 1-D shear-wave velocity models for the intersection of Lines Z and E154
Figure B13: 1-D shear-wave velocity models for the intersection of Lines Z and F.....155

CHAPTER 1

INTRODUCTION

Importance of karst and objectives of the study

Karst topography is characterized by the presence of sinkholes, caves, solution channels, and complicated underground drainage networks (Ford and Williams, 2007). The complex morphology results from the chemical weathering of carbonate and other soluble rocks, and the formation of karst features is controlled in part by pre-existing fractures within the bedrock (Ford and Williams, 2007). Sinkhole formation is also controlled by overburden thickness, fluctuation of the water table, soil type, and the presence of recharge/discharge zones (Denizman, 2003).

Karst terrains are particularly susceptible to groundwater contamination because sinkholes can rapidly introduce pollutants into the subsurface and contaminate aquifers. In Albany, Georgia, the Upper Floridan Aquifer is particularly susceptible to nitrate contamination due to the high density of sinkholes in the area (Gordon, 2008). Furthermore, de-watering and lowering of the water table associated with aquifer pumping can actually initiate sinkhole formation (Hicks et al., 1987). Contaminants can also become concentrated in karst depressions, so knowledge of bedrock topography can be useful in remediation work (Higuera-Diaz et al., 2007). Wells are also placed along lineaments or fracture traces due to high yields, so improved knowledge of subsurface-conditions can aid in well placement (Parizek, 1976, Tam et al., 2004).

Although karst features are often manifested at the ground surface, the local extent of karstification is difficult to determine without more detailed subsurface investigations. For engineering and environmental studies, site-specific characterizations are typically necessary to address concerns about potential hazards. The goal of this investigation is to determine whether or not models of shear-wave velocity derived from analysis of seismic surface waves can effectively resolve variations in bedrock depth, cavities within bedrock, and the orientation of major fractures at a site near Albany, Georgia. Numerical and field studies have established the usefulness of the technique, but Rayleigh-wave dispersion characteristics have not been established for every geologic setting (Nasseri-Moghaddam et al., 2007). Therefore, this study is designed to establish base-line geophysical data (including shear-wave velocities for near-surface materials), determine resolution limits, and improve the understanding of sinkhole development with respect to fracture systems.

The geophysical results will be compared with known fracture orientations and observed sinkhole patterns in the area. Correlation of geophysical data and morphological observations will provide a better understanding of the shear-wave velocity structure associated with potential subsidence features. In particular, establishing velocity information for geologic materials will be indispensable in future investigations without the aid of borehole logs.

Geophysical investigations of karst

Numerous techniques have been used to characterize karst terrain. In morphometric studies combined with remote sensing techniques, identification of linear features has been useful in describing regional patterns of sinkhole formation along

prominent fractures (Brinkmann et al., 2008; Galve et al., 2008). However, lineament mapping can be a subjective process (Tam et al., 2004), and many features cannot be identified with these techniques (Parizek, 1976).

More detailed investigations of the shallow subsurface often rely on boreholes to characterize subsurface conditions. Due to the spatial variability of karst features, information from individual boreholes may be insufficient for a complete site evaluation. Geophysical profiles provide continuous coverage between boreholes, and a number of geophysical techniques including seismic, micro-gravity, electrical resistivity, ground-penetrating radar, and electro-magnetic methods have been successfully employed to characterize the subsurface in karst regions (Doolittle et al., 1998; Miller et al., 2005; Thierry et al., 2005; He et al., 2006; Schrott and Sass, 2008). Because each technique has inherent advantages and drawbacks, a combination of methods is often used to constrain the interpretation.

In recent years, Multi-Channel Analysis of Surface Waves (MASW) has emerged as a popular field method for investigations of the shallow subsurface. The technique uses dispersion of Rayleigh waves to construct 2-D models of shear-wave velocity structure of the subsurface. Shear-wave velocity is directly related to the shear modulus (rigidity), which is the ratio of shear stress to corresponding shear strain. The relationship is given by the following equation:

$$V_s = \beta = (\mu/\rho)^{1/2},$$

where β is shear-wave velocity, μ is the shear modulus, and ρ is material density.

Because shear-wave velocity can be used to differentiate between solid bedrock and

different types of overburden, engineers can make informed decisions regarding structural designs.

Shear-wave velocity information is also important in the evaluation of earthquake hazards. The relationship between velocity and shear modulus allows engineers to assess the susceptibility of a site to ground motion and soil liquefaction (Andrus and Stokoe, 2000). In tectonically active areas, MASW has been utilized in site-response studies and planning efforts (Luke et al., 2008). Lin et al. (2004) also demonstrated the applicability of MASW in assessing soil liquefaction potential.

Geologic setting of the study area

The development of sinkholes and other karst features in areas underlain by limestone bedrock is widespread throughout the Atlantic and Gulf Coastal Plains. The study area is located in the Dougherty Plain physiographic province of southwest Georgia (Figure 1.1), which can be classified as covered, karst terrain (Hicks et al., 1987). In this region, unconsolidated Quaternary sediment ranging in thickness from 6 to 24 meters covers the Ocala Formation, which is Eocene in age (55.8-33.9 Ma). The Ocala Limestone hosts the Upper Floridan Aquifer (Figure 1.2), which supplies large quantities of water for agricultural, industrial, and domestic uses in the southeast United States (Hicks et al., 1987; Gaswirth et al., 2006). A stratigraphic column for the Dougherty Plain physiographic province is shown in Figure 1.3.

The Ocala Limestone consists of three separate units; the middle unit represents the top of the formation in the study area (Stewart et al., 1999). This unit consists of light tan, friable, clayey, fossiliferous, weathered, dense limestone (Stewart et al., 1999). The

aquifer is confined below by the middle Eocene Lisbon formation, which is composed of glauconitic, argillaceous limestone (Hicks et al., 1987).

The Quaternary sediment that overlies the Ocala formation consists of sands and calcareous clays representing fluvial deposits or residuum from erosion of bedrock (Hicks et al., 1987). USGS borehole logs indicate that the depth to the Ocala Formation is approximately 9 meters in the survey area (Figure 1.4), and the thickness of the sediment cover generally increases moving east toward the Flint River. The sediments have variable permeability, which influences direct recharge of the aquifer (Hayes et al., 1983).

Sinkholes and topographic depressions are common features across the Dougherty Plain because of dissolution of limestone beneath the overburden (Hicks et al., 1987; Hyatt and Jacobs, 1996). Voids form when sediment is eroded and transported downward through fractures and cavities in the bedrock. Eventually, overlying sediment will collapse into the void when cohesion is insufficient to support the soil arch. The sinkholes in the region of Albany, GA are classified as either suffosion or collapse sinkholes (Hyatt and Jacobs, 1996). Collapse sinkholes form relatively rapidly from the sudden collapse of overburden, while suffosion sinkholes develop gradually as the ground slowly subsides (Waltham et al., 2005). Groundwater flow is the primary agent of erosion, and soil type is an important factor controlling sinkhole development. Voids can form beneath clay layers leading to sudden collapse, while relatively sandy soils will subside more slowly (Hicks et al., 1987). Figure 1.5 shows the locations of sinkholes in the study area.

Sinkhole formation is controlled by regional structural lineaments as well as more localized fracture systems (Parizek, 1976; Brook and Allison, 1983). Preferential weathering due to increased groundwater flow slowly enlarges the vertical fractures, thereby creating void space. Weathering along bedding planes also forms horizontal solution channels in the bedrock. The overlying sediment is thus susceptible to erosion or collapse into the void space. Although spacing of fractures in the Ocala formation is unknown, fracture orientations of 325, 5, and 40 degrees have been identified in Dougherty County, Georgia (Brook and Allison, 1983), and a correlation has been found between the orientation of sinkhole development and fracture trends along the Flint River (Hyatt and Jacobs, 1996).

Multi-channel analysis of surface waves (MASW)

The dispersive property of Rayleigh waves (i.e. the dependence of velocity on frequency) provides extremely useful information about the properties of near-surface materials. Longer wavelength energy propagates to greater depths, while higher frequency energy is attenuated in the near-surface. This frequency dependence can be used to derive models of shear-wave velocity as a function of depth, which in turn can be used to characterize subsurface geology.

Multi-Channel Analysis of Surface Waves is a non-invasive, near-surface geophysical method typically applied in investigations of the upper 30 meters of the ground surface (Park et al., 2005). It was developed to address the limitations of the spectral analysis of surface waves (SASW) technique developed by Nazarian and others (1983). SASW utilizes two receivers to measure Rayleigh-wave phase velocity, but noise can be difficult to distinguish when using only one pair of receivers (Park et al., 1999).

Therefore, an array of receivers is employed with MASW to reduce the influence of noise on the measurement of phase velocity as a function of frequency. The phase velocities are then inverted for models of shear-wave velocity as a function of depth. Depth to bedrock, fracture zones, cavities, and paleo-karst can be located by analyzing changes in shear-wave velocity in the subsurface (Miller et al., 2005). As noted earlier, shear-wave velocity is related to shear modulus, which is a measure of stiffness commonly used in geotechnical studies (Stokoe et al., 1994). Shear-wave velocity can be used to differentiate various types of unconsolidated soils and bedrock (Odum et al., 2007). For carbonate rocks, shear-wave velocity is affected by porosity and pore structure (Baechle et al., 2009). Competent bedrock typically exhibits higher velocities than soil, fractured rock, or cavities.

There are three main steps associated with the technique: data acquisition, generation of dispersion curves, and inversion (Park et al., 1999). Data acquisition can be accomplished using either an “active” or “passive” survey. “Active” refers to the use of an artificial impact source such as a sledge-hammer, accelerated weight-drop, or vibroseis deployed in-line with the array (Park et al., 2005). “Passive” refers to the use of lower-frequency cultural or natural energy such as traffic or tidal motion. This type of energy is more difficult to use because it can come from any direction; to obtain accurate measurements of phase velocity, these directions must be determined and taken into account (Park et al., 2007). The depth of the investigation is limited by the lowest frequency generated by the seismic source and length of the geophone (sensor) array. Appropriate geophones, such as 4.5 Hz, are therefore necessary to record the lowest frequencies. In general, active surveys are effective to depths of up to 30 meters, and

passive surveys can penetrate to depths up to 100 meters (Park et al., 1999). The following equation can be used to determine the approximate depth of penetration (Rix and Leipski, 1991; Park et al., 1999):

$$D = V_p / (2 * f),$$

where D is the depth of penetration and V_p is the phase velocity measured for frequency, f.

Ultimately, the maximum depth of penetration is determined by the maximum wavelength resolved by the geophone array. This is equal to the array aperture; the maximum depth of investigation is generally considered to be half of this length. The array aperture also controls lateral resolution, and features smaller than half the array width cannot be fully resolved (O'Neill et al., 2008).

A trade-off between lateral resolution and depth penetration is inherent with the MASW method. Longer wavelength energy propagates to greater depths. Therefore, the frequency range constrains the depth of shear-wave velocity investigations. Greater depth penetration is achieved by recording longer wavelength energy, but spatial resolution decreases as a result. A common approach is to combine the active and passive methods to optimize spatial resolution over a range of depths.

The software used for processing and inverting data for this study was Surfseis, a program developed by the Kansas Geological Survey. The generation of dispersion curves is accomplished by a slant-stack (normalized summation of amplitudes along linear trajectories across a shot gather) followed by a Fourier transformation and computation of the amplitude spectrum of the stack. The time-space domain is effectively transformed to produce a contour plot of phase velocity (apparent velocity of coherent

energy across an array) versus frequency (McMechan and Yedlin, 1981). The contour plot, referred to as an overtone record, often shows dispersion for several modes of surface waves (Aki and Richards, 2002; Xia et al., 2009). Figure 1.6 shows the relationship between group/phase velocity and frequency for different modes. The dispersion curve is determined by picking the phase-velocity for a range of frequencies; for this study, only the fundamental mode was used. A dispersion curve is generated for each shot gather; each curve represents an average across the receiver spread (Lin et al., 2004).

The final step in MASW is the inversion of the dispersion curves for models of shear-wave velocity as a function of depth. The algorithm used for the inversion was developed by Xia et al.(1999). Linearized inversion involves the calculation of partial derivatives that measure the change in phase velocity at a certain frequency given a small change in shear-wave velocity (Aki and Richards, 2002).

The inversion procedure is based upon an initial velocity model generated from the dispersion curve, and model parameters are adjusted until the velocity model corresponds with the dispersion curve. The P-wave and S-wave velocities used in the inversion process are approximated from the dispersion curve, and additional parameters are shown in Table 1.1. An iterative procedure is used to finalize the model; the analysis is complete when the root-mean-square (RMS) misfit between the observed phase velocities and the phase velocities predicted by the model fall below a specified threshold, or when the number of iterations reaches a specified maximum value. Each dispersion curve is inverted to generate a 1-D shear-wave velocity model that represents an averaged velocity function at the mid-point of the geophone spread. Consequently,

each vertical profile represents shear-wave velocity averaged across a given geophone array (Lin et al., 2004). In the following chapters, the station number for a given shot gather or dispersion curve refers to the mid-station location, not the source location. The 1-D velocity models derived from individual shot points can be combined to construct a pseudo-2-D model of the subsurface. A pseudo-3-D shear-wave velocity model can be generated by collecting data along closely spaced, parallel profiles.

Field Acquisition

The field site was located on the Albany Water, Gas, and Light Commission well-field southwest of Albany, Georgia (Figure 1.5). Extensive sinkhole development in this area is a natural consequence of the geologic setting, but anthropogenic disturbance has likely exacerbated the problem. The Albany well-field was constructed to extract water from the Upper Floridan Aquifer in order to supplement water supplies for agricultural and other uses (Gordon, 2008). The shallow depth to bedrock is well suited for the MASW technique, and borehole logs from the well installations provide control for the geophysical interpretations. The field site was situated in an open, grassy area with little topography near well # 44. A possible fracture zone was identified based upon a prominent N-S line of sinkholes formed in 2007. Fracture data also supports this interpretation (Brook and Allison, 1983). Many of the sinkholes have been backfilled, but one recently formed sink indicated that erosion was still active.

The locations of the seismic lines are shown in Figure 1.7. The initial data set was collected in April 2009. Line A was established perpendicular to the prominent N-S trend of sinkholes in the vicinity of well #44. In November 2009, surface wave data were collected along six additional lines. The additional lines were oriented parallel to Line A

and spaced 20 meters apart. The east-west orientation of the lines was established to analyze the N-S lineament orientation inferred from sinkhole alignment and fracture data. In March of 2010, surface wave data were collected along two cross-lines. Lines Y and Z intersect Lines A-G at approximately station 63 and 83, respectively. The lines were established to assess prominent shear-wave velocity anomalies identified in the previous surveys.

The lengths of the active-source and passive-source seismic lines are shown in Tables 1.2 and 1.3, and Figure 1.8 illustrates the array geometry. Each station was flagged at one-meter intervals, and the elevation for each station was surveyed in relation to the top of the concrete pad for well # 44 to establish topographic profiles for each line. Station 1 is located at the east end of Lines A-G and the north end of Lines Y and Z. Coordinates for the end-points of the lines were obtained using a GPS receiver.

Active Survey

The receiver spacing and source-receiver offset for the active survey was one meter in order to achieve adequate lateral resolution. Station 1 was designated as the first shot station, so station 2 was the first receiver station. Twenty-four channels were recorded for each shot, so the recording aperture of the geophone spread for each shot record was 23 meters. Maximum depth of penetration and minimum resolution width are therefore equal to approximately 12 meters. Lateral resolution can be improved by including only half of the traces (half the array width) in computation of the overtone records (Chapter 5). Channel one was located nearest to the shot location.

The surface wave data were collected using a Bison 9000 Series Digital Instantaneous Floating Point (DIFP) seismograph and 4.5 Hz geophones. A 'roll-along

survey' was conducted, so the source and active 24 geophone sub-set were moved down the line one meter at a time. A sledge-hammer with piezo-electric trigger was used as the seismic source, and four hammer blows were typically stacked for each record. Stacking is used to improve the signal-to-noise ratio. For random noise, the ratio of signal to noise improves by roughly the square root of N, where N is the number of records stacked (Aki and Richards, 2002).

Passive survey

The passive survey was conducted to generate lower frequency energy for increased depth penetration. A moving van was used as the seismic source; the van moved in line with the array to avoid complications due to variations in azimuth of incoming planar waves. The MASW data analysis is not dependent on absolute time, so the van proved to be a viable seismic source. The geophone spread length was increased to 46 meters by increasing the geophone spacing to two meters. Continuous surface wave data was recorded for 10 seconds, so multiple surface waves are incorporated into the overtone analysis.

Typical Processing Flow

The seismic data was initially processed using Winseis and Eavesdropper software (Kansas Geological Survey; 1989, 1992). Output files for the active and passive surveys were generated for processing using Surfseis, a surface-wave analysis software package developed by the Kansas Geological Survey (Park et al., 2000). Surfseis was used to generate overtone records, pick dispersion curves, and invert the dispersion picks to produce models of shear-wave velocity as a function of depth. The typical processing flow is shown in Figure 1.9, and the recording parameters are shown in Table 1.4.

Slightly different processing techniques were used for the active and passive surveys as outlined below. More details regarding the data processing can be found in Appendix A.

The Dispersion (1) and Dispersion (2) functions within Surfseis were used for data processing. The principal difference is that Dispersion (2) allows the user to specify upper and lower bounds to constrain the automatic picking of phase velocity dispersion curves and, in particular, to avoid branches corresponding to higher modes. Dispersion 2 was adopted as the primary processing tool for both the active and passive surveys. This option reduced processing time and minimized the number of files generated.

First, an input file consisting of individual trace gathers was chosen for processing. At this point, additional muting could be performed for each record to minimize interference with the direct P-wave, higher mode surface waves, and other noise. Muting was not attempted for records generated with the passive source because of the high-degree of overlap between P-waves and surface waves over the 10-second recording window. The muting procedure was typically tested for each record to determine its effectiveness, and the mute was not always employed. The effects of muting are discussed in more detail in Chapter 2.

The optimum frequency and phase velocity range was established by analyzing the characteristics of the overtone records. After the overtone record was generated, Surfseis automatically picked the dispersion curve for the fundamental mode and displayed the signal-to-noise ratio. The user could then manually edit the curve if the frequency range was questionable or if contamination by a higher mode was suspected. A smoothing function (3-point or 5-point running average) was also applied to the frequency-phase velocity curve to suppress oscillations of the overtone record due to

noise. Overtone records lacking clear expression of the fundamental mode were excluded from the final inversion. The 1-D models generated in the inversion process were automatically combined to create a 2-D shear-wave velocity model.

Table 1.1: Inversion Parameters

<u>Inversion Parameters</u>	
Poisson's Ratio	0.4
Density	2.0 g/cc
Layers	10
Maximum Iterations	12
RMSE (in phase velocity)	5 m/s

Table 1.2: Active-source seismic lines

<u>Active-source Seismic Lines</u>			
	<u>Distance spanned by recording stations (m)</u>	<u>Distance spanned by mid-point of 24-channel arrays (m)</u>	<u>Station numbers of mid-points</u>
Line A	173	143	13-156
Line B	101	76	13-89
Line C	120	93	13-107
Line D	92	73	13-86
Line E	89	70	13-83
Line F	89	70	13-83
Line G	89	70	13-83
Line Y	240	215	13-228
Line Z	155	130	13-153

Table 1.3: Passive-source seismic lines

Passive-source Seismic Lines			
	<u>Distance spanned by recording stations (m)</u>	<u>Distance spanned by mid-point of 24-channel arrays (m)</u>	<u>Station numbers of mid-points</u>
Line A	173	122	25-147
Line B	101	52	25-77
Line C	120	72	25-97
Line D	92	46	25-71
Line E	89	46	25-71
Line F	89	46	25-71
Line G	89	46	25-71
Line Y	240	190	25-215
Line Z	155	94	25-119

Table 1.4: Recording Parameters

Recording Parameters		
	<u>Active</u>	<u>Passive</u>
Seismic Source	Hammer	Van
Geophones	4.5 Hz	4.5 Hz
Sampling Rate	0.002 s	0.002 s
Number of Samples	500	5000
Record Length	1.0 s	10.0 s
Geophone Spacing	1.0 m	2.0 m
Source Spacing	1.0 m	Variable
High-cut Filter	250 Hz	250 Hz
Low-cut Filter	4 Hz	4 Hz



Figure 1.1: Dougherty Plain physiographic province (modified from Alhadeff et al., 2001).

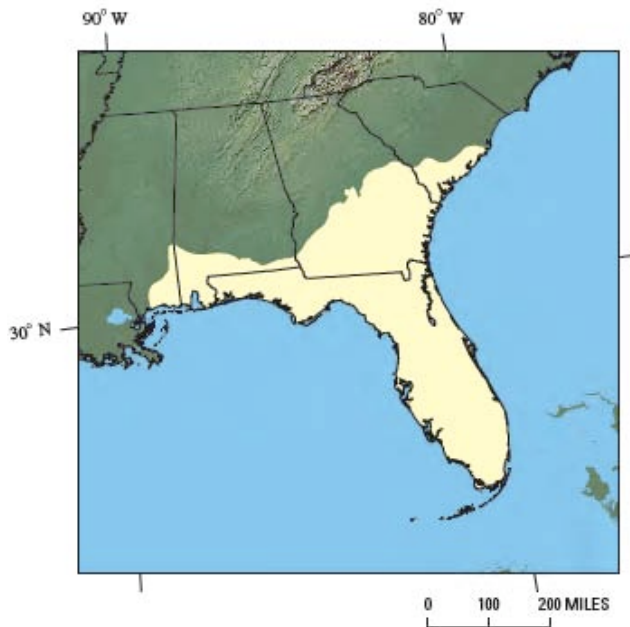


Figure 1.2: Extent of the Upper Floridan Aquifer in the southeastern United States (Maupin and Barber, 2005).

ERA-THEM	SYSTEM	SERIES	GULF COAST STAGE	GROUP AND FORMATION			
				Northwest Area	Southeast Area		
Cenozoic	Quaternary	Holocene	Wisconsin to Nebraskan	Undifferentiated overburden	Undifferentiated overburden		
		Pleistocene					
	Tertiary	Eocene	Pliocene	Foleyan	[Hatched pattern]	[Hatched pattern]	
			Miocene	Clovellian		[Hatched pattern]	Undifferentiated sediments
				Ducklakin			[Hatched pattern]
				Napoleonvillian (restricted)			[Hatched pattern]
			Anahuacian	[Hatched pattern]		[Hatched pattern]	
			Oligocene	Chickasawhayan (restricted)		[Hatched pattern]	Suwannee Limestone
		Vicksburgian		[Hatched pattern]	[Hatched pattern]		
		Eocene	Late Eocene	Jacksonian	Ocala Limestone	Ocala Limestone	
					Clinchfield Sand	[Hatched pattern]	
			Middle Eocene	Claibornian	Claiborne Group	Lisbon Formation	Lisbon Formation
	Tallahatta Formation					Tallahatta Formation	

Figure 1.3: Stratigraphic column of the Dougherty Plain physiographic province (Hicks et al., 1987).



Figure 1.4: Borehole log for Well #44 obtained from the USGS Water Science Center in Atlanta, Georgia.

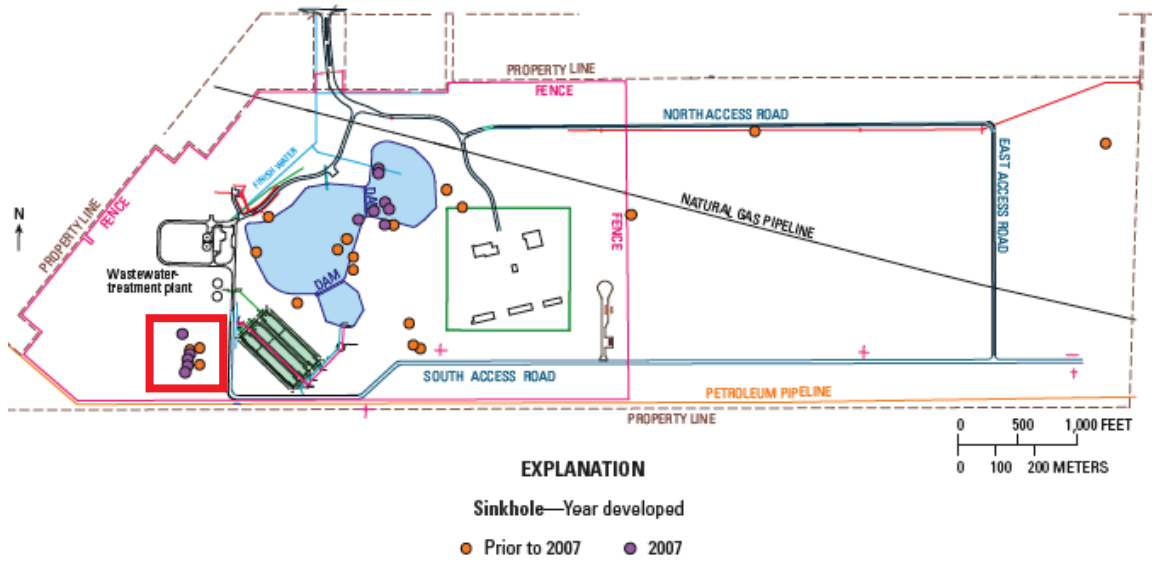


Figure 1.5: Sinkhole formation at the Albany WGL well field (Gordon, 2008). The approximate limits of the study area are outlined in red.

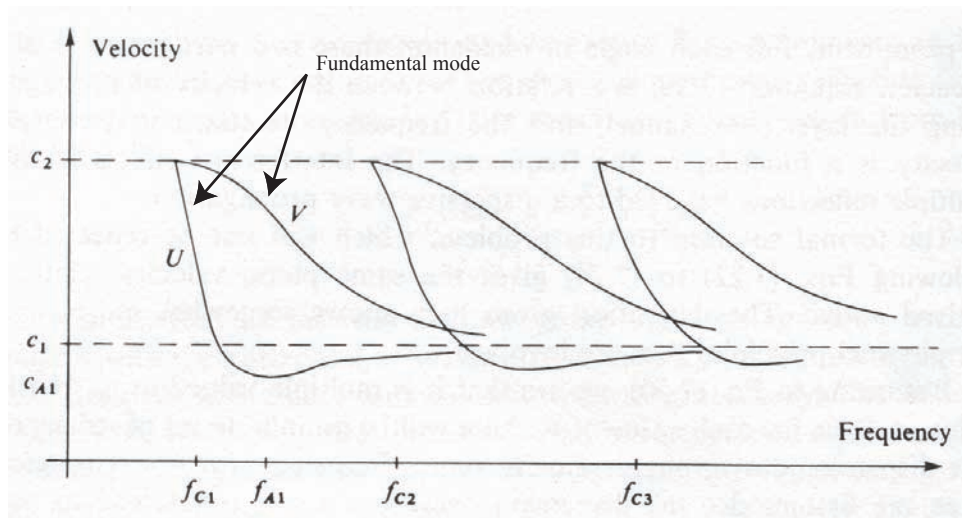


Figure 1.6: Group velocity (U) and phase velocity (V) for the fundamental mode and two higher mode surface waves. The frequency ranges for each mode are different, but certain frequency components for each mode have the same group and phase velocity. Therefore, all modes arrive over the same time window. The implications for trace muting are discussed in Chapter 2. (diagram taken from Officer, 1974)

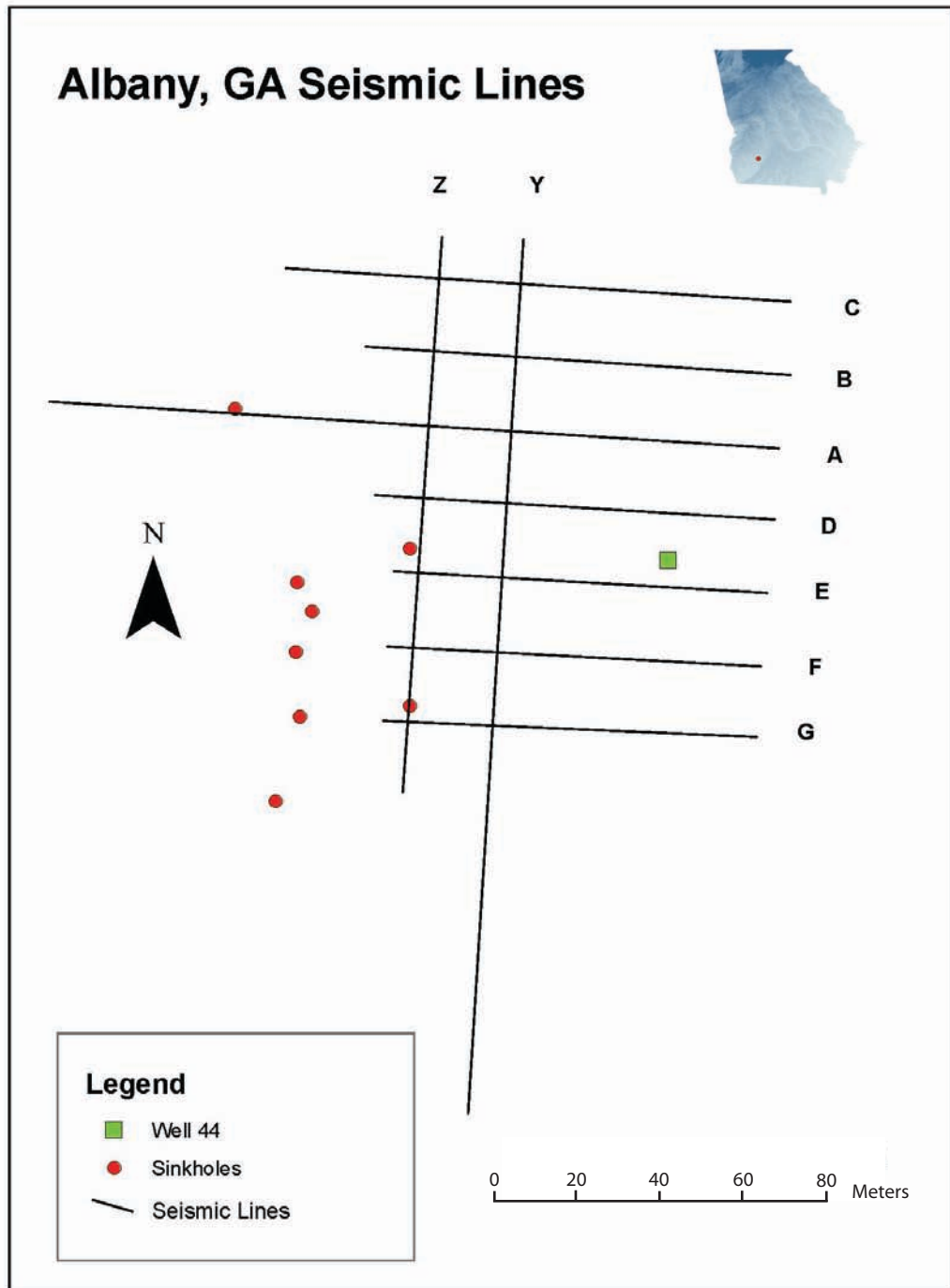


Figure 1.7: The location of seismic lines in relation to well #44 and past sinkhole development (inset map from Alhadeff et al., 2001).

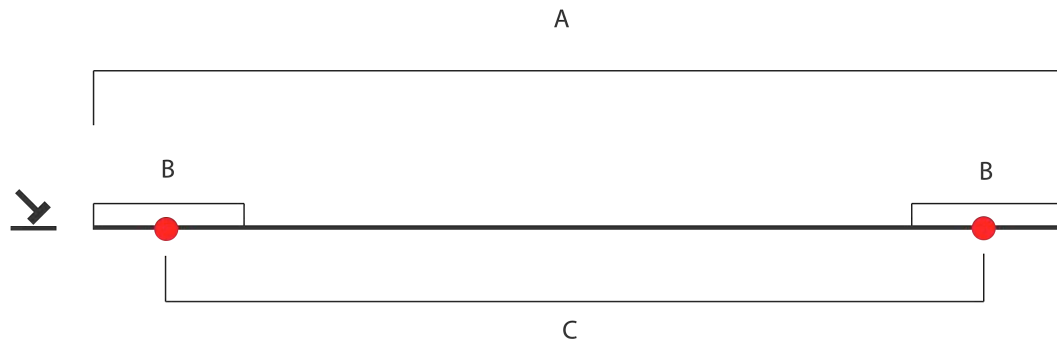


Figure 1.8: Schematic diagram of array geometry for the roll-along seismic survey. (A) Distance spanned by the recording stations; (B) Distance spanned by one 24-channel array; (C) Distance spanned by mid-points of 24-channel arrays.

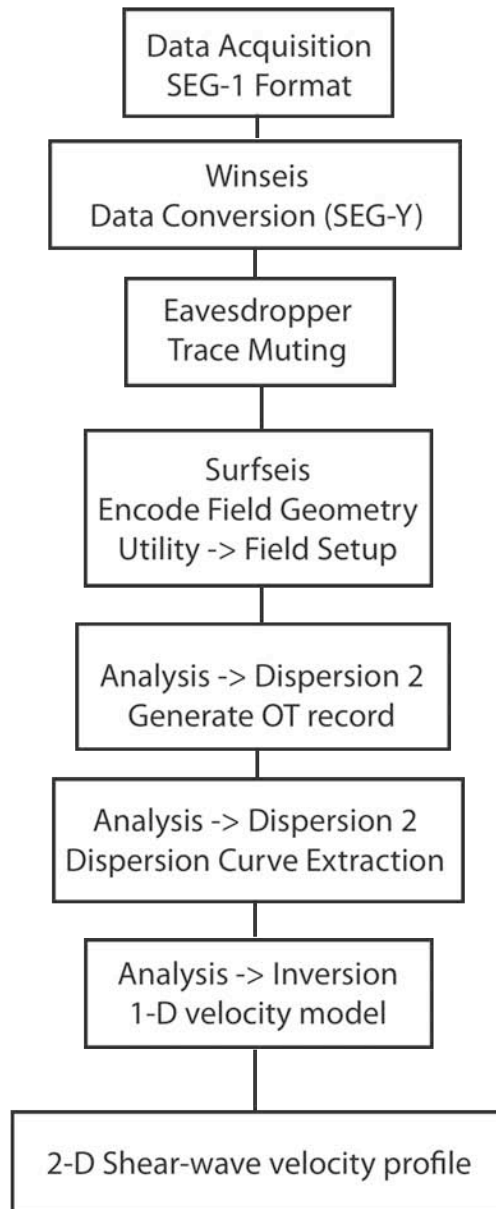


Figure 1.9: Processing Flow Diagram. Surface-wave analysis consists of three main steps; data acquisition, dispersion curve picking from overtone (OT) or amplitude contour plots, and inversion of the dispersion curve picks for models of shear-wave velocity.

CHAPTER 2

SHEAR WAVE VELOCITY MODELS – LINES A-G

The following set of models for Lines A-G represent “conservative” models of the subsurface. The term “conservative” implies that overtone records were derived from shot records with a minimum of pre-processing applied (e.g. no muting) and that the phase velocity picks used in the inversions were restricted to frequency ranges that showed a clear separation from higher modes. The display and processing parameters are shown in Tables 2.1 and 2.2, and additional details can be found in Appendix A.

Data Processing: Dispersion curve picking and muting procedures

The frequency range used for dispersion curve picking depended on the array length, seismic source, target geology, and quality of the fundamental mode image on individual overtone records. As noted earlier, the maximum depth for shear-wave velocity calculation is generally considered to be half of the longest wavelength measured (Rix and Leipski, 1991; Park et al., 1999). The longest wavelength, in turn, is equal to the length of the 24-channel geophone spread. Therefore, the maximum depth penetration and resolution width are approximately 12 meters for the active array and 23 meters for the passive array.

Figure 2.1 shows the typical frequency spectra for the active and passive shot gathers. The typical low-frequency cut-off was 10 Hz, but the minimum frequency chosen for each dispersion curve depended on the amplitude peaks on the overtone image. The maximum frequency for dispersion curve picking also depended on the target

depth and quality of the overtone records. For the passive survey, the frequency range was restricted to 10-20 Hz in order to focus on the geology below the bedrock surface. The frequency range for the active survey was restricted to 13-25 Hz to image the upper 12.5 meters of the subsurface for reasons outlined below.

A close examination of dispersion curves and corresponding inversion models for Line G yields significant insight concerning the appropriate frequency range for dispersion curve picking. The confidence in dispersion curve picking is directly influenced by the quality of the fundamental mode surface wave image. Figures 2.2A and 2.3A show a shot gather and overtone image where the fundamental mode and another higher mode surface wave are clearly evident. For the overtone record, 10-40 Hz appears to be a reasonable frequency range given the consistent amplitude peak of the fundamental mode and the high signal-to-noise ratio. The 1-D inversion model and 2-D shear-wave velocity profile are shown in Figures 2.4A and 2.5A.

Muting of the shot record reveals that the up-warping of the dispersion curve at high frequencies (30-45 Hz) may be due to contamination by higher modes and therefore contribute to distortion of the velocity model. Figures 2.2B and 2.3B show the muted shot gather and corresponding overtone record. The higher mode surface wave is almost completely eliminated, and the up-warping of the fundamental mode at higher frequencies disappears. The new 1-D velocity model (Figure 2.4B) is shown for comparison.

Muting is always accompanied by unavoidable trade-offs. Since all modes arrive over the same time window, application of a mute to suppress energy at higher modes will always result in some loss of energy in the fundamental mode. In particular, if the

mute targets the early portion of the surface wave train, then energy at the lowermost frequencies of the fundamental mode will be lost because this propagates at the highest group velocities (Figure 1.6). As a result, this portion of the dispersion curve may be distorted (see also Chapter 3). The benefit is seen at the higher frequencies, where muting eliminates high-amplitude phase-velocity branches of the higher mode, making the lower-amplitude branches of the fundamental mode at lower phase velocities easier to observe.

Figure 2.5B shows the model for Line G using a restricted frequency range of 13-25 Hz for picking dispersion curves on overtone records derived from un-muted shot gathers. The low-velocity anomaly at STA 52 is characterized by a depression in the shear-wave velocity structure (i.e. thickened section of low velocities). In Figure 2.5A, the same anomaly can be characterized as a closed, circular feature. Thus, the bull's-eye characteristic and high-velocity layer in the upper 5 meters of the initial model (Figure 2.5A) are interpreted to be distortions of the shear-wave velocity structure due to contamination by higher modes.

Two options are available for addressing contamination by higher modes. As demonstrated above, the frequency range can be restricted to lower frequencies, where the dispersion curve monotonically decreases. This option ultimately provides a more “conservative” model (as defined above) of the subsurface, so the likelihood of introducing false anomalies decreases. The alternative is to apply the wedge mute to each shot gather to suppress contamination by higher modes at higher frequencies. Ivanov et al. (2005) have isolated the higher-frequency portion of the fundamental mode from higher mode surface waves using this muting procedure. For this data set, preliminary

tests indicate that muting is effective when the tail end of the fundamental mode surface wave is prominent on the shot gathers. The results of the first processing technique are presented below, and the profiles generated using muted shot gathers are presented in Chapters 3 and 5.

Conservative Models: Line A-G

The following set of models was generated using un-muted records and a restricted frequency range to avoid distortion associated with higher-mode contamination of the fundamental mode. The active and passive-source models for Lines A-G are shown in Figures 2.6-2.9. Comparisons between active and passive models for each line are also shown in Figures 2.10-2.16. The locations of the lines are indicated in Figure 1.7.

The prominent features on Lines A-G are described in the following sections, and correlations between the active and passive profiles on each line are noted. In each of the profiles, the depth at which shear-wave velocity exceeds 350 m/s is used to define the depth to bedrock. This criterion is based on the depth to bedrock from the borehole log as well as the steep velocity gradient evident on the passive profiles at the same depth. The more gradual variations in shear-wave velocity below the bedrock surface (steep velocity gradient) are interpreted as variations in fracture volume. For the models derived from the active-source data, the resolution width (again, the width of the narrowest feature resolvable by the survey) is about 12 meters; for the passive-source models, the resolution width is about 23 meters. A comprehensive analysis of potential subsidence features and lineament trends will be provided in Chapter 6.

Line A

Figure 2.10 shows the active and passive-source shear-wave velocity models for Line A. In the active model, the depth to bedrock is 10-12 meters, and prominent velocity anomalies are located at STA 15, 48, 75, and 80-120. For the passive-source model, the depth to bedrock ranges from 10-12 meters, and a significant low-velocity zone extends from STA 110 to 147. The most prominent region of lower shear-wave velocities is located at STA 115. The anomalies from the active model are not visible on the passive model, but the section from STA 70-95 is characterized by relatively low shear-wave velocity (400-500 m/s). Several alternative models for Line A are discussed in Chapter 3.

Line B

Figure 2.11 shows the active and passive-source shear-wave velocity models for Line B. For the active-source model, the depth to bedrock is 8-12 meters. Lateral variation is significant, and zones of lower shear-wave velocity extend from STA 20-30 and 38-40. There is a broad low-velocity zone (LVZ) at STA 60-80, and a prominent anomaly is centered at STA 70. For the passive-source profile, the depth to bedrock is 8-10 meters. Although it is narrower than the resolution width, the LVZ at STA 63-76 clearly correlates with the active model.

Figure 2.17 shows the dispersion curve for STA 19 on the active model. The signal is particularly strong, and the fundamental mode is well-defined. This curve can be compared with dispersion curves corresponding with the observed anomalies at STA 37 and STA 69. Figure 2.18A and 2.19A show the dispersion curves for STA 37 and STA 69 on the active model. The signal is strong at low frequencies, and the amplitude peaks

at approximately 13 Hz correspond with lower phase velocities compared with Figure 2.17.

In general, for all profiles, the mode branches in the overtone records for the passive profiles are less continuous than those for the active profiles. The gaps in frequency are generated by the repetition of the source signal over the 10-second recording window. A similar effect is seen for seismic waves generated by ripple-fired quarry blasts (Pollack, 1963).

For the passive survey dispersion curves, the amplitude peaks on the overtone records for STA 37 and 39 on Line B (Figures 2.18B and 2.19B) show the same general trend as those for the active survey, but they are generally more erratic. Therefore, confidence in the dispersion curve picks is relatively lower. Nonetheless, the remarkable correlation between the active and passive models at STA 70 indicates that the curves are still valid. The depressions in the shear-wave velocity structure are therefore considered to be representative of anomalous geology.

Line C

Figure 2.12 shows the active and passive-source models for Line C. The active-source model shows a depth to bedrock of 7-13 meters. A broad low-velocity zone exists from STA 35-60, and a prominent anomaly is evident at STA 38-42. High-velocity structure is evident between STA 85-100 where shear-wave velocity exceeds 400 m/s. On the passive model, the depth to bedrock is 9-11 meters. Variable shear-wave velocity structure is evident from STA 25-80, and the most prominent LVZ is located at STA 63. The low-velocity zone at STA 40-45 roughly corresponds with the anomaly at STA 38-

42 on the active model. The high velocity zone at STA 90 also correlates with the active model.

Figure 2.20A shows the dispersion curve for STA 39 on the active profile, and the curve for STA 89 in the high-velocity area is shown for comparison (Figure 2.21A). The strength of the signal is high at low frequencies on both overtone images, and confidence in the data is particularly high. The anomalous zone at STA 38-45 likely represents a fractured zone or potential subsidence feature. The data from the passive survey also supports this interpretation. Figures 2.20B and 2.21B show the dispersion curves for STA 39 and 89. The signal on both overtone records is equally strong, so a fundamental discrepancy in the data quality is not an issue.

The correlations between the two independent data sets indicate that the models are representative of geologic structure. A broad low-velocity zone between STA 30-80 and a high-velocity zone between STA 80-100 are evident on both profiles. However, it is also important to note that every anomaly on the passive profiles does not have a corresponding signature on the active profiles. For example, the most prominent anomaly on the passive profile at STA 63 is not defined by any obvious feature on the active profile. This is to be expected, given the factor-of-two difference in the resolution widths for the two data sets. The dispersion curve for this location is shown in Figure 2.22.

Line D

The active and passive-source models for Line D are shown in Figure 2.13. For the active-source model, depth to bedrock is 9-13 meters. A broad low-velocity zone exists at STA 40-60, and other prominent low-velocity regions exist at STA 13-20 and 45-50. The disrupted velocity structure at the end of the line (STA 70-88) may result

from end effects associated with data processing. Starting with the record for STA 69, the number of traces on the shot gathers decreases by one. The final record consists of only 12 traces, so the low frequencies and depth of penetration are lost.

The depth to bedrock in the passive-source model is 9-10 meters (Figure 2.13). The shear-wave velocity structure is variable across the entire profile, but noticeable depressions are evident at STA 34-35, 40-45, 50-55, and 65-68. The broad area of low-velocity on the active profile corresponds with the anomalies at STA 40-45 and 50-55.

Figure 2.23A shows the dispersion curve associated with the low-velocity anomaly at STA 45. The dispersion curve for the high-velocity zone at STA 31 is shown for comparison (Figure 2.24A). The amplitude peak for the latter dispersion curve indicates higher shear-wave velocity. The model from the passive survey shows high lateral variation below the bedrock surface, and there are no definitive correlations with the active survey. Figure 2.23B and 2.24B show the corresponding passive-source dispersion curves for comparison. The dispersion curve for the prominent anomaly at STA 35 on the passive profile is also shown (Figure 2.25), and the more gradual slope of the curve may be indicative of an area of lower shear -wave velocity. However, the erratic signal for the fundamental mode could also introduce a false anomaly if the dispersion curve is not picked carefully.

Line E

The active and passive-source models for Line E are shown in Figure 2.14. For the active model, the depth to bedrock (7-12 meters) and shear-wave velocity structure is variable across the entire profile, but there is a prominent anomaly at STA 55-72 at depths shallower than 5 meters and STA 58-65 at depths greater than 5 meters. The

passive-source model shows depth to bedrock of 9-10 meters. There is a circular velocity anomaly at STA 35, and down-warpings of the velocity contours are evident at STA 55 and 65-67. The latter anomaly roughly corresponds with the down-warping at STA 58-65 on the active profile.

Figure 2.26 and 2.27 show dispersion curves for STA 63 and 65 on the active model, and the curve for STA 53 is shown for comparison (Figure 2.28). The quality of the overtone records is equivalent for the three records, so the anomaly does not appear to be a result of unreliable dispersion curves. The prominent anomaly on the passive profile is offset slightly at STA 67, and Figure 2.29A shows the dispersion curve. The dispersion curve for the high velocity zone at STA 39 is shown for comparison (Figure 2.30A). Although the frequency ranges are different, the appearance of the curve from 14-20 Hz is very similar. Figure 2.29B and 2.30B show the 1-D inversion records for STA 67 and 39, respectively.

Line F

The active and passive-source models for Line F are shown in Figure 2.15. Depth to bedrock on the active profile is 7-10 meters. Low-velocity zones occur at STA 13-15 and STA 35-45, and a high-velocity zone (below the bedrock surface at a depth of 10-15 meters) is located at STA 55-65. The depth to bedrock on the passive profile is 8-10 meters, and low velocity zones occur at STA 25-29, 37, 41, 47, 52-59, and 67-71. The high-velocity zone at STA 60-65 corresponds with the active model. These anomalous zones are smaller than the resolution width (11.5 m), so they do not represent fully resolved structures.

The final passive-source model was generated after examining dispersion curves from anomalous features on the initial model (Figure 2.31A). The bull's eye anomaly at STA 55 on the initial passive model represents a potential subsidence feature. This feature is also smaller than the 23-meter resolution width for the passive survey. The dispersion curve is shown in Figure 2.32A. The highest velocities (500 to 600 m/s) do not correspond to distinct amplitude peaks, and it is arguable whether or not the signal is reliable at these frequencies. Therefore, a new dispersion curve was picked for this record, as well as the records for STA 53 and 57. Figure 2.32B shows the alternate dispersion curve for STA 55. After replacing the original dispersion curves with more conservative picks, the bull's eye feature does not appear in the new 2-D velocity model (Figure 2.31B). Although this section of the profile is still characterized by low velocity, it seems that the bull's-eye characteristic is primarily a function of using unreliable frequency ranges when picking dispersion curves. The high-velocity region between STA 60-67 in the passive source model is now in better agreement with the high-velocity region in the active-source model.

Automated dispersion curve picking expedites processing, but this example illustrates the sensitivity of the inversion process. Subtle changes in the shape of the dispersion curve can dramatically alter the shear-wave velocity profile, so it is imperative to ensure that models are derived using reliable picks of the dispersion curve. Particular care must be taken when extracting picks for the passive data because the mode peaks are not continuous.

Line G

The active and passive-source models for Line G are shown in Figure 2.16. The depth of the bedrock surface on the active model is highly variable, but the general depth range is 8-12 meters. Precise locations of low velocity zones are difficult to determine, but a prominent region of lower velocities occurs at STA 35-37. On the passive model, the depth to bedrock is 10-11 meters (even the slight dip to the east is discernable), and regions of lower velocity and depressions in the velocity contours are evident at STA 25-30, 37-40, 46-49, and 58-68. The latter region contains a circular anomaly centered at STA 65.

Figure 2.33 shows the dispersion curve and 1-D inversion model for STA 65, where there is a bull's-eye feature. Since the frequency range was restricted to avoid contamination of the fundamental mode, it is likely that this anomaly is representative of a low-velocity zone within the bedrock rather than an artifact.

Comparison of models with topographic profiles

Karst features are often exhibited as topographic depressions (Denizman, 2003), so shear-wave velocity models were compared with topographic profiles for each line. The comparisons are shown in Figures 2.34-2.40. It is important to note that construction of Well #44 has resulted in alteration of the natural landscape, and several man-made drainage features are evident in the topographic profiles. The natural depressions are very subtle on the profiles, so correlations are also based on field observations of circular depressions across the landscape.

Comparisons between the shear-wave velocity models and topographic profiles indicate that surface depressions alone are not always reliable indicators of subsidence.

Subtle topographic depressions at STA 70 on Line B, STA 63 on Line D, and STA 64 on Line E can be correlated with low-velocity zones at depth. However, observations from Line A indicate that potential collapse features are not always associated with relatively low topography. The initial “conservative” shear-wave velocity model indicates that the section from STA 70-115 is characterized by a broad low-velocity zone in the subsurface, but there is a relatively high point at STA 78. Simple observations from the shot gathers and more intensive modeling indicate that a prominent low-velocity zone is located at STA 78-87. The modeling results supporting this interpretation are discussed in more detail in the next chapter.

Table 2.1: Display Parameters for conservative models. Contrast refers to the relative emphasis of the dominant mode in comparison to other energy on the overtone plot (Park et al., 2000). A value of two signifies a relatively high emphasis of higher mode energy.

<u>Display Parameters for Overtone Records</u>	
Frequency Range	5-50 Hz
Phase Velocity Range	50-1000 m/s
Contrast	2

Table 2.2: Processing Parameters for conservative models

<u>Processing Parameters</u>	
Analysis	Dispersion 2
Data Points	50
Smoothing	5 points

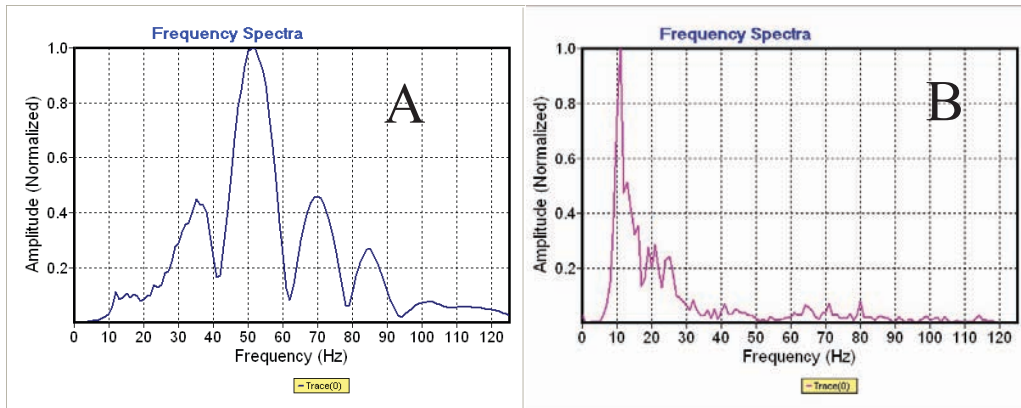
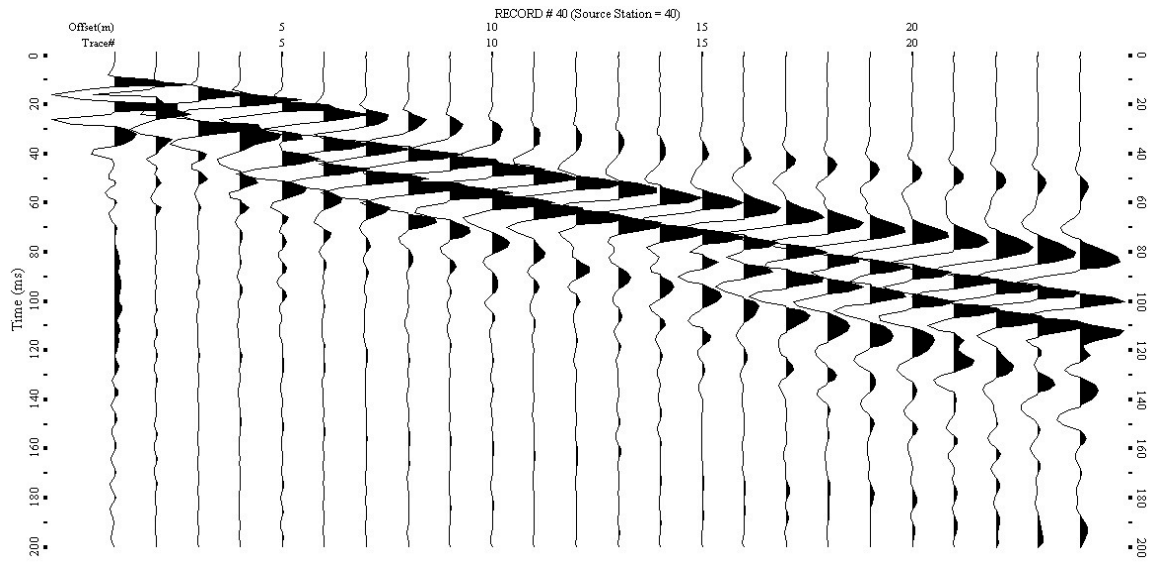


Figure 2.1: Typical frequency spectra for shot gathers; (A) active-source, (B) passive-source.

A)



B)

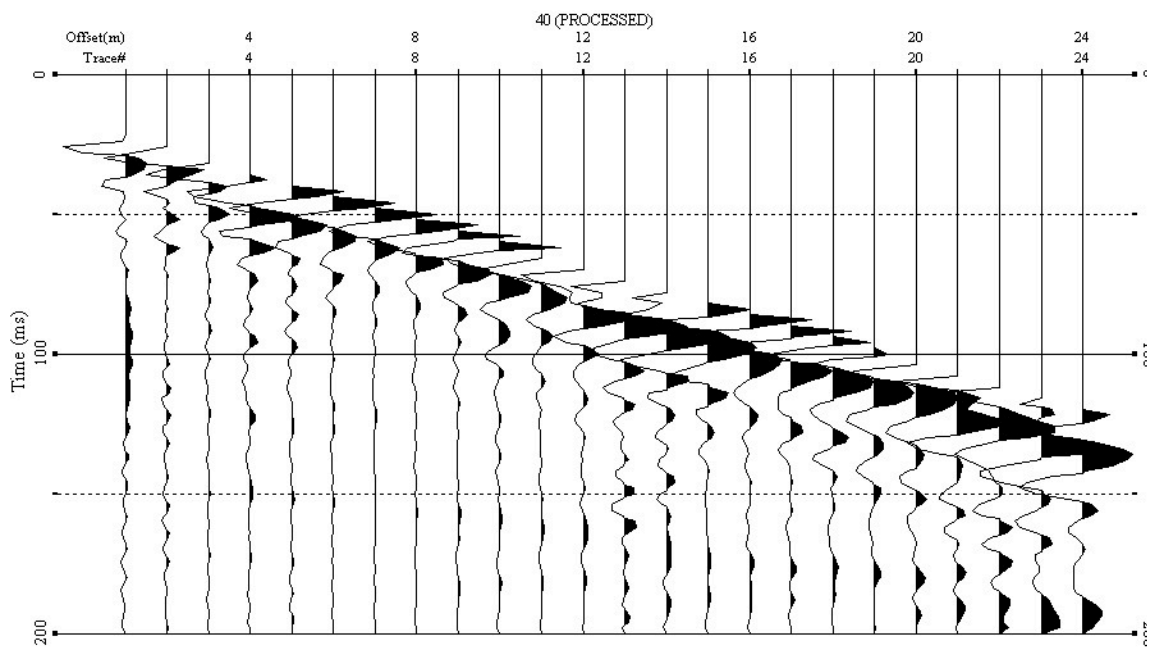
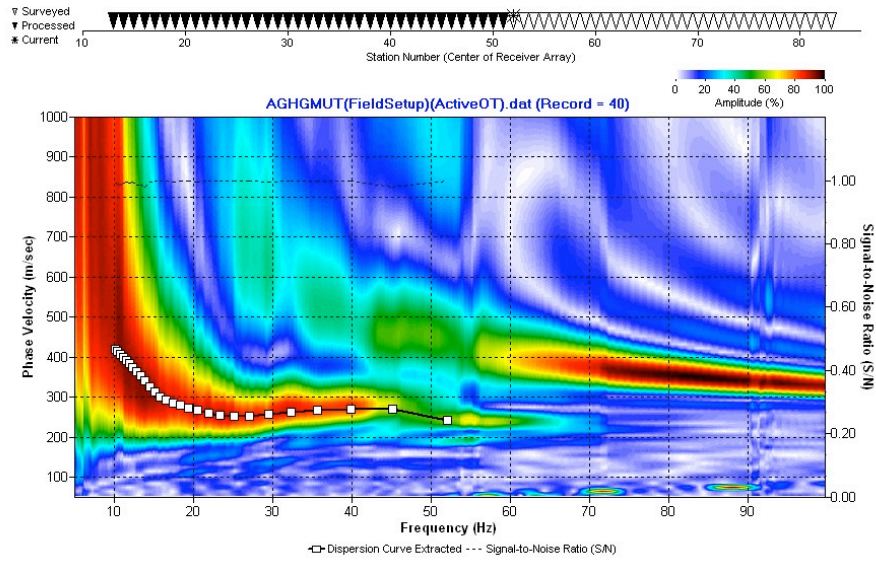


Figure 2.2: Shot gathers for STA 52 on Line G. A) No muting; B) Wedge mute applied to remove energy associated with the direct wave and higher mode surface waves.

A)



B)

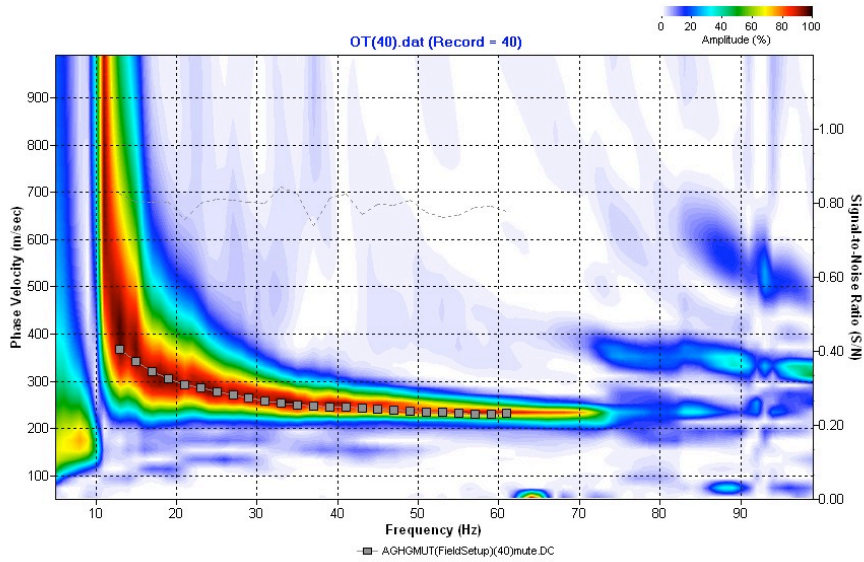
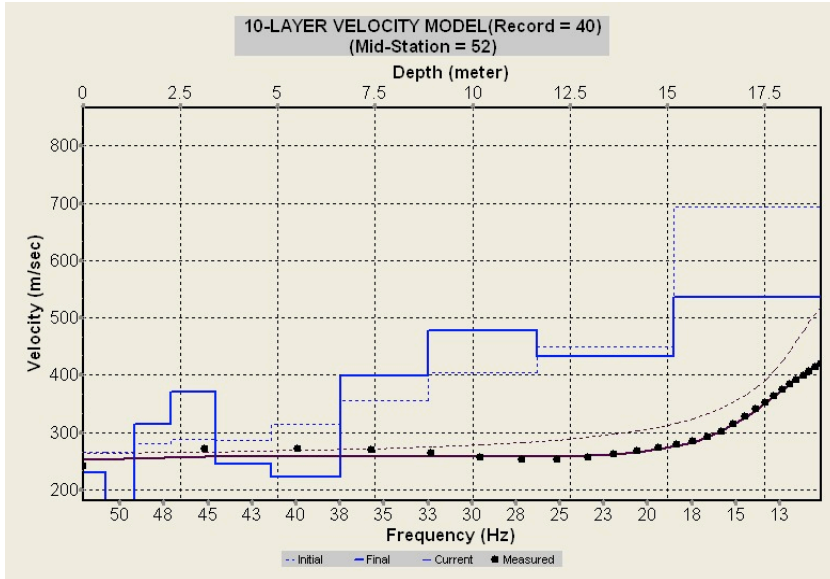


Figure 2.3: Overtone images (amplitude contour plots) and dispersion curve picks (squares) for STA 52 on Line G. A) No muting; B) wedge mute

A)



B)

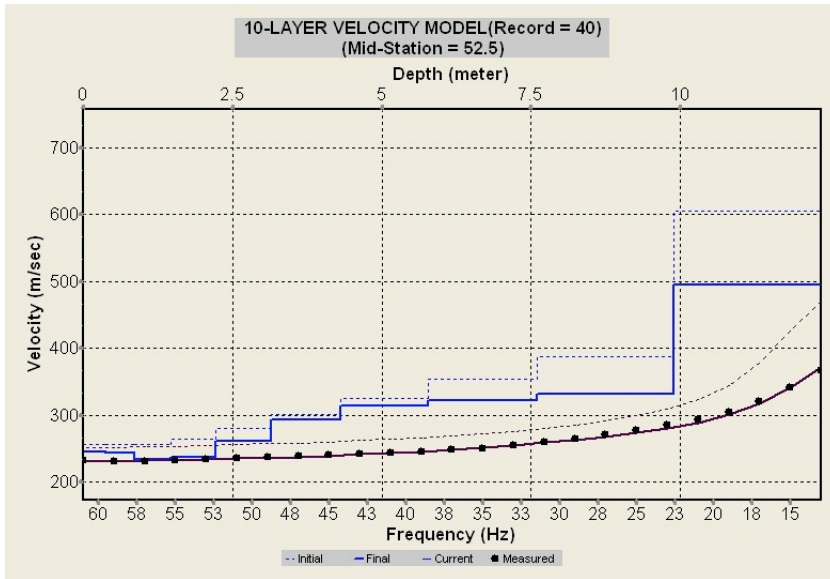


Figure 2.4: 1-D shear-wave velocity models for STA 52 on Line G. A) No muting; B) Wedge mute.

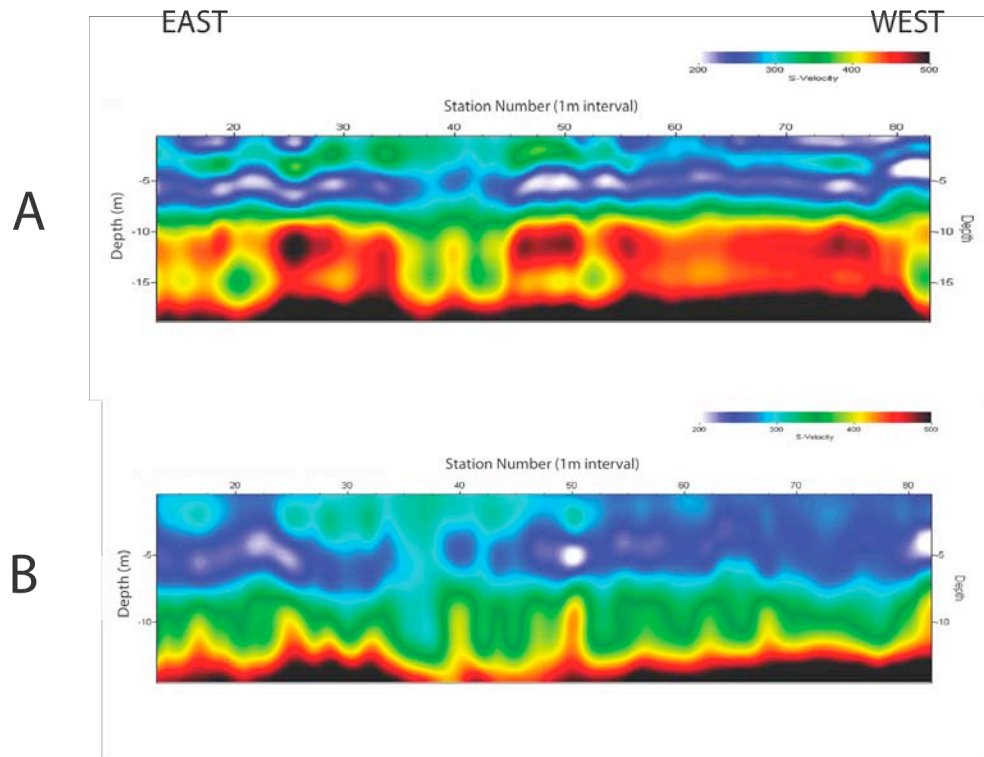


Figure 2.5: Alternate models for Line G using different frequency ranges for dispersion curve picking. A) Unrestricted frequency range: 10-100 Hz (VE = 0.92); (B) Frequency range restricted to 12-25 Hz (VE = 1.18). Overtone records used for dispersion curve picking were derived from un-muted shot gathers. Note that increasing the minimum frequency from 10 to 12 Hz decreases the depth of penetration from 17 to 14 meters.

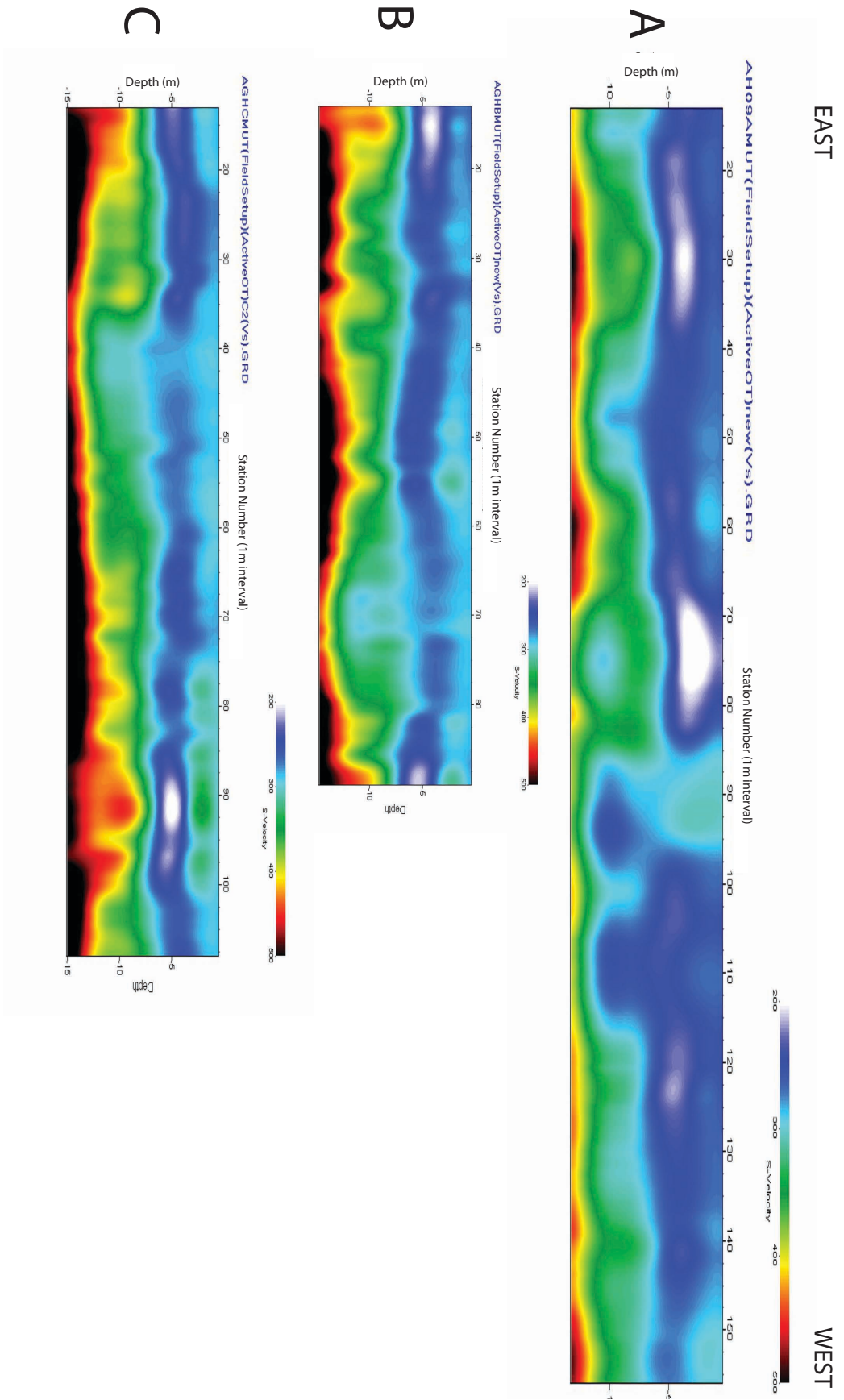


Figure 2.6: Active-source models for Lines A (VE = 1.3), B (VE = 1.2), and C (VE = 1.2).

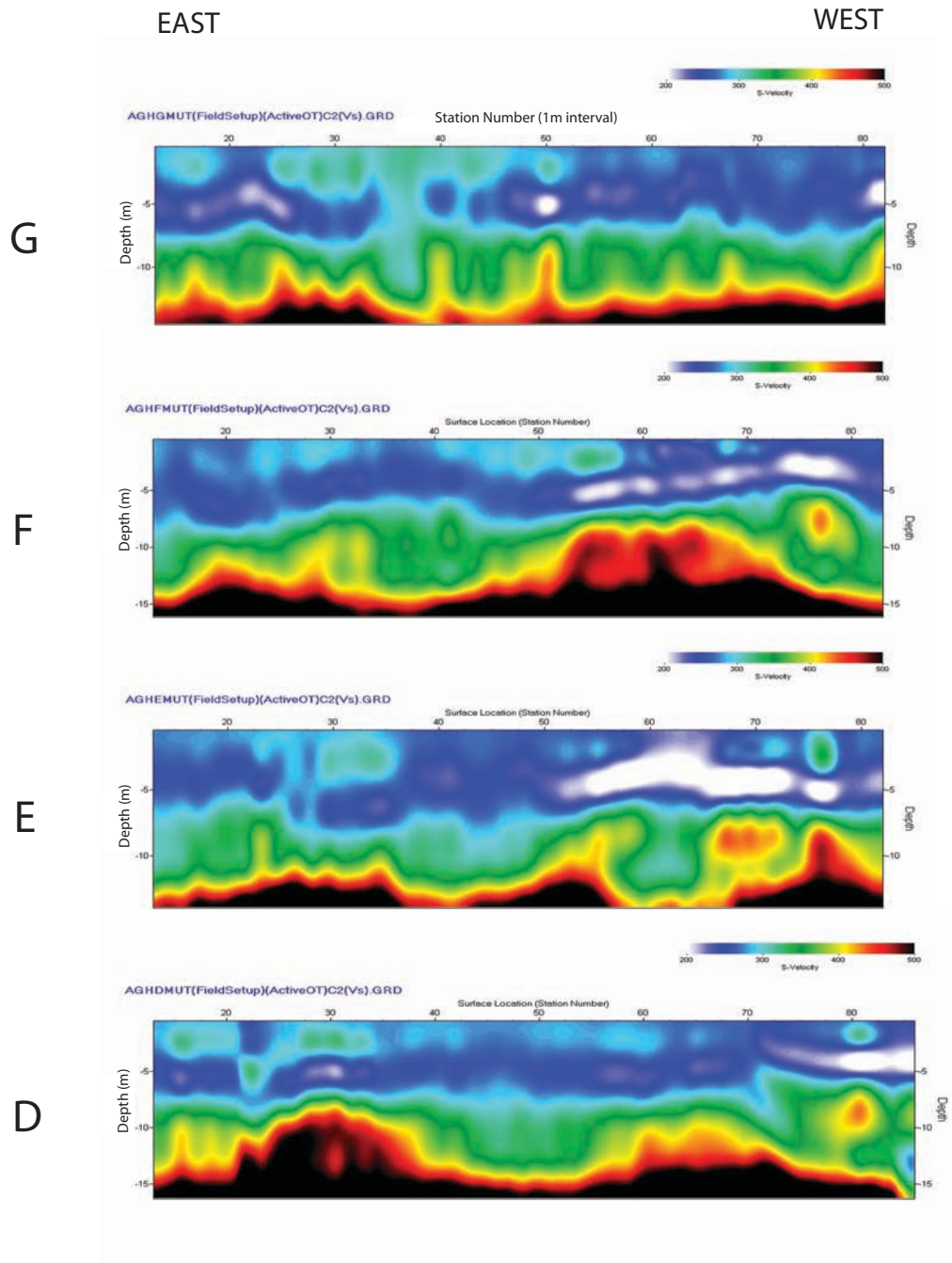


Figure 2.7: Active-source models for Lines D (VE = 1.1), E (VE = 1.2), F (VE = 1.1), and G (VE = 1.2).

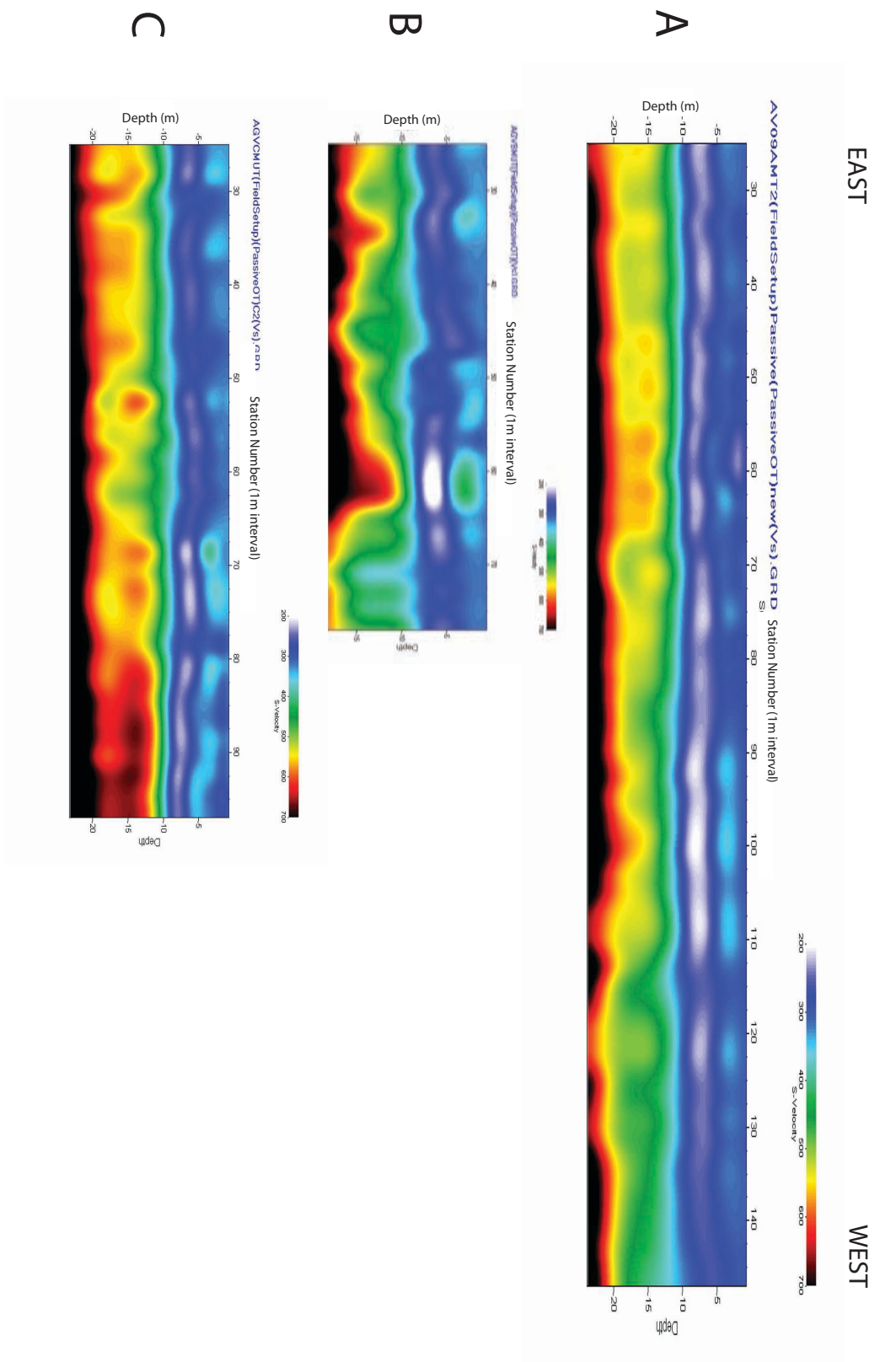


Figure 2.8: Passive-source models for Lines A (VE = 0.7), B (VE = 0.9), and C (VE = 0.7).

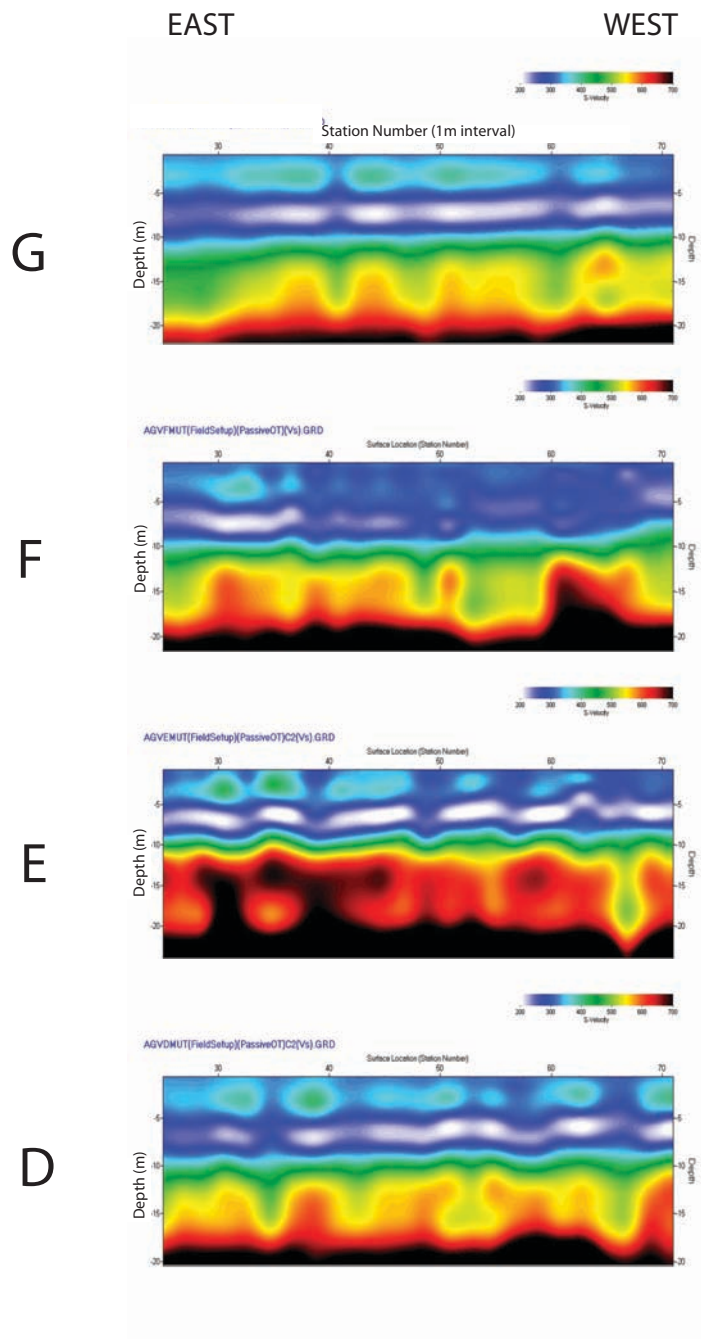


Figure 2.9: Passive-source models for Lines D (VE = 0.8), E (VE = 0.7), F (VE = 0.8), and G (VE = 0.8).

EAST

WEST

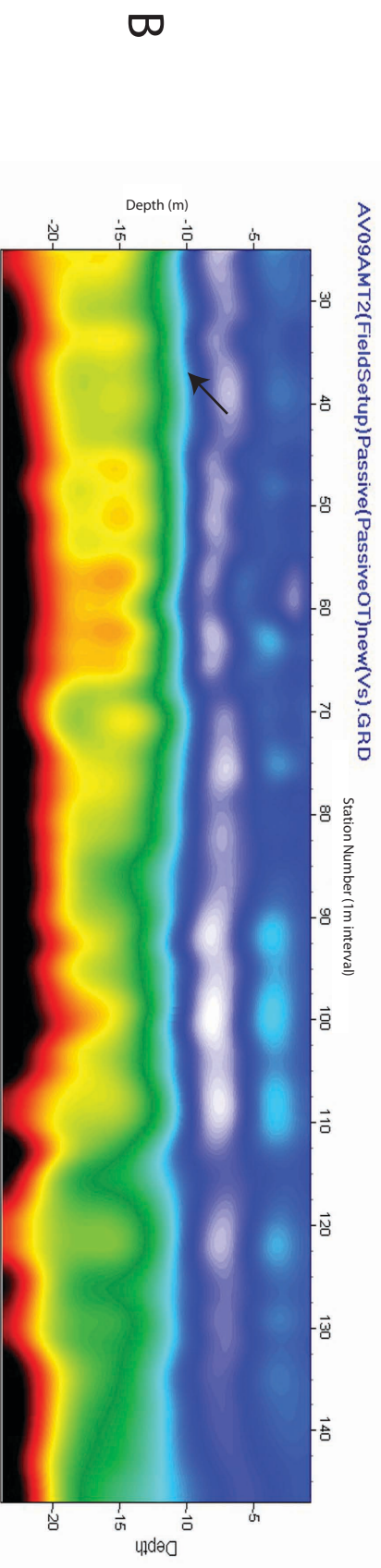
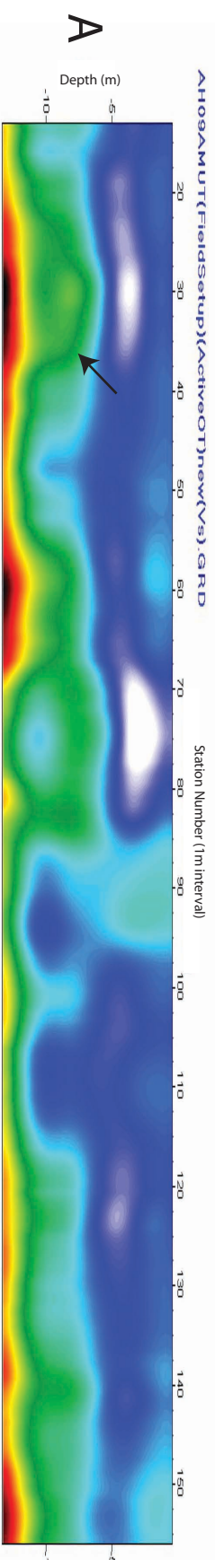


Figure 2.10: The active-source (A) and passive-source (B) models for Line A (VE = 1.3). Arrow indicates 350 m/s contour line.

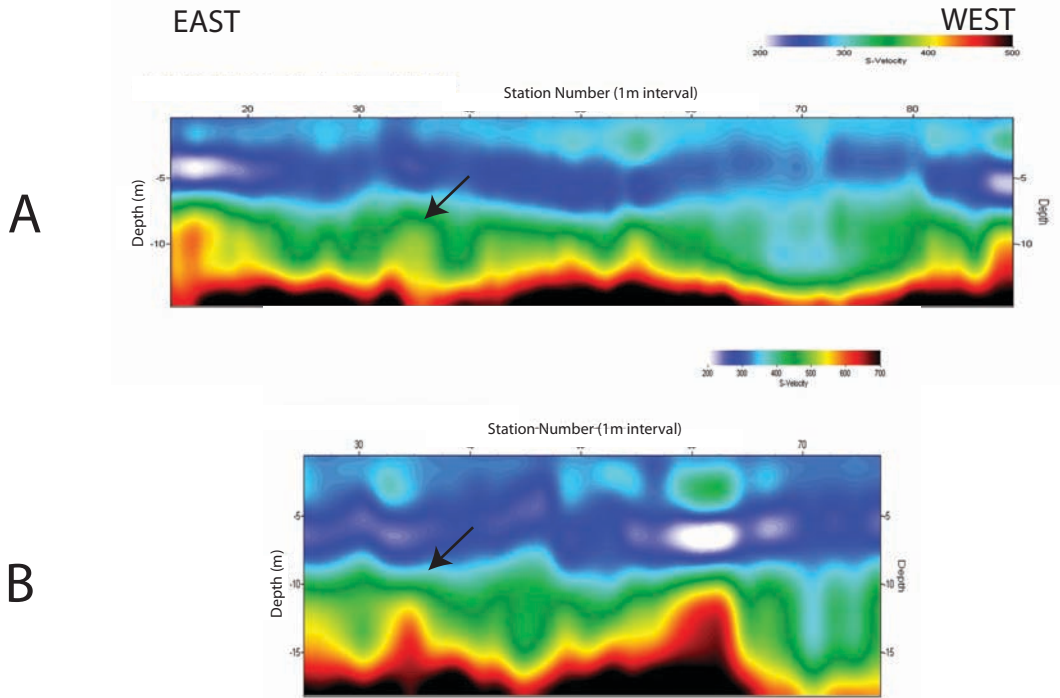


Figure 2.11: Active-source (A) and passive-source (B) models for Line B (VE = 1.2). The arrow indicates the 350 m/s contour.

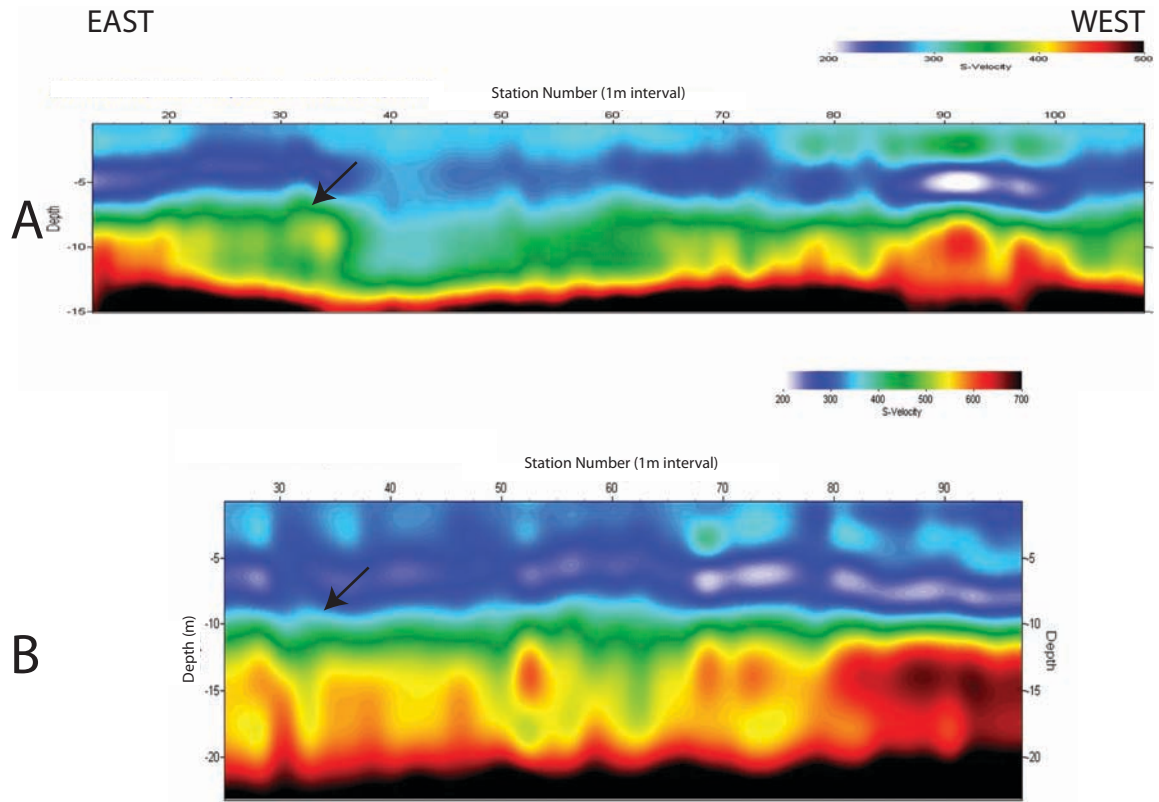


Figure 2.12: Active-source (A) and passive-source (B) models for Line C (VE = 1.2). The arrow indicates the 350 m/s contour.

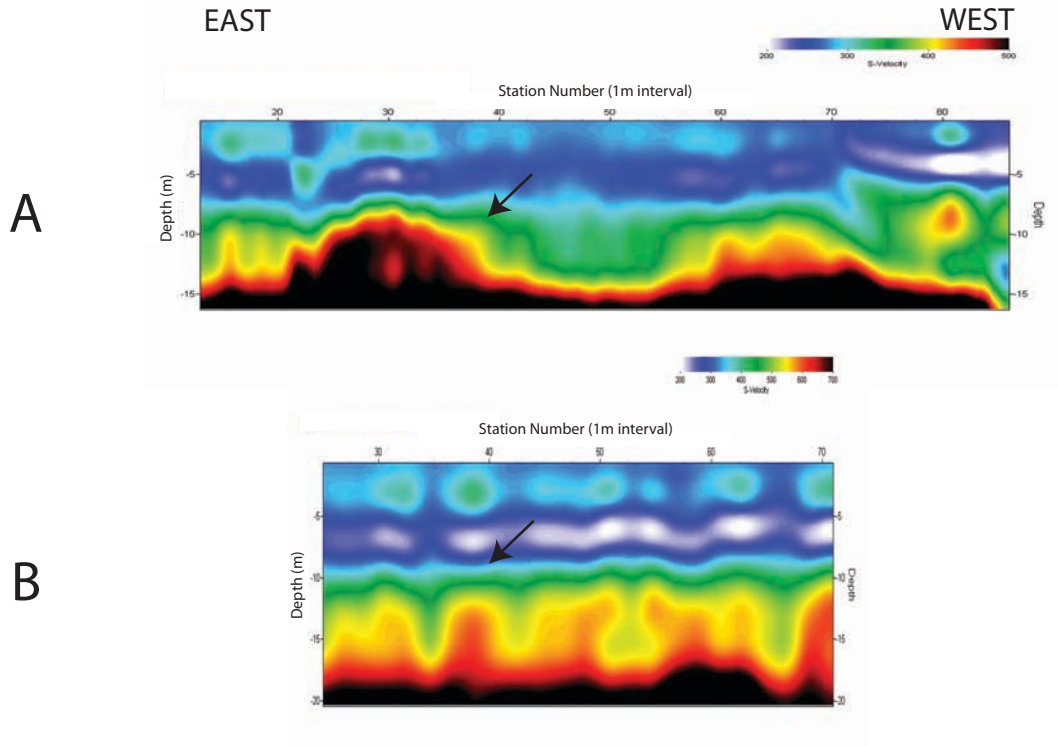


Figure 2.13: Active-source (A) and passive-source (B) models for Line D (VE = 1.1). The arrow indicates the 350 m/s contour.

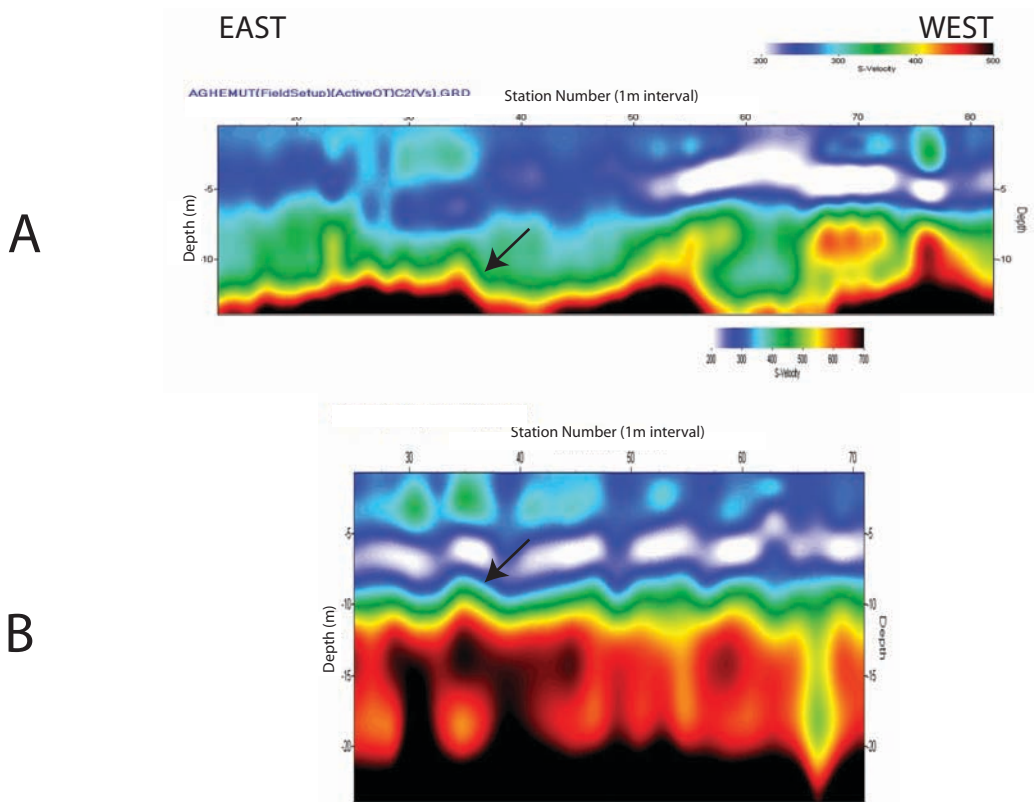


Figure 2.14: Active-source (A) and passive-source (B) models for Line E (VE = 1.2). The arrow indicates the 350 m/s contour.

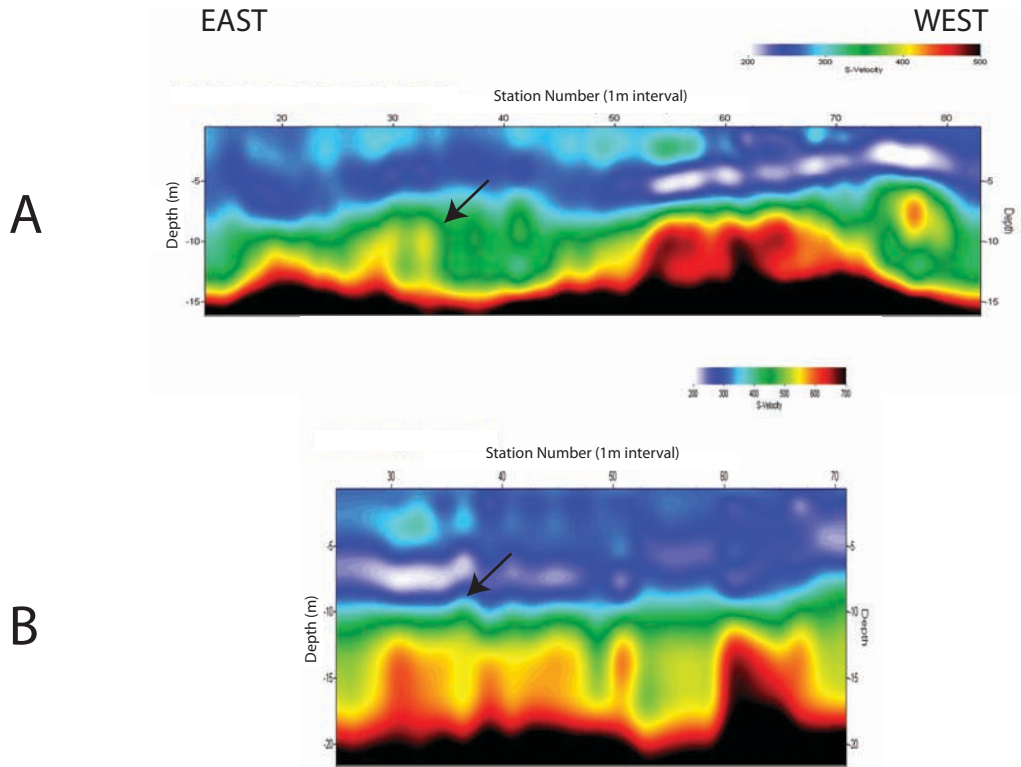


Figure 2.15: Active-source (A) and final passive-source (B) models for Line F (VE = 1.1) The arrow indicates the 350 m/s contour.

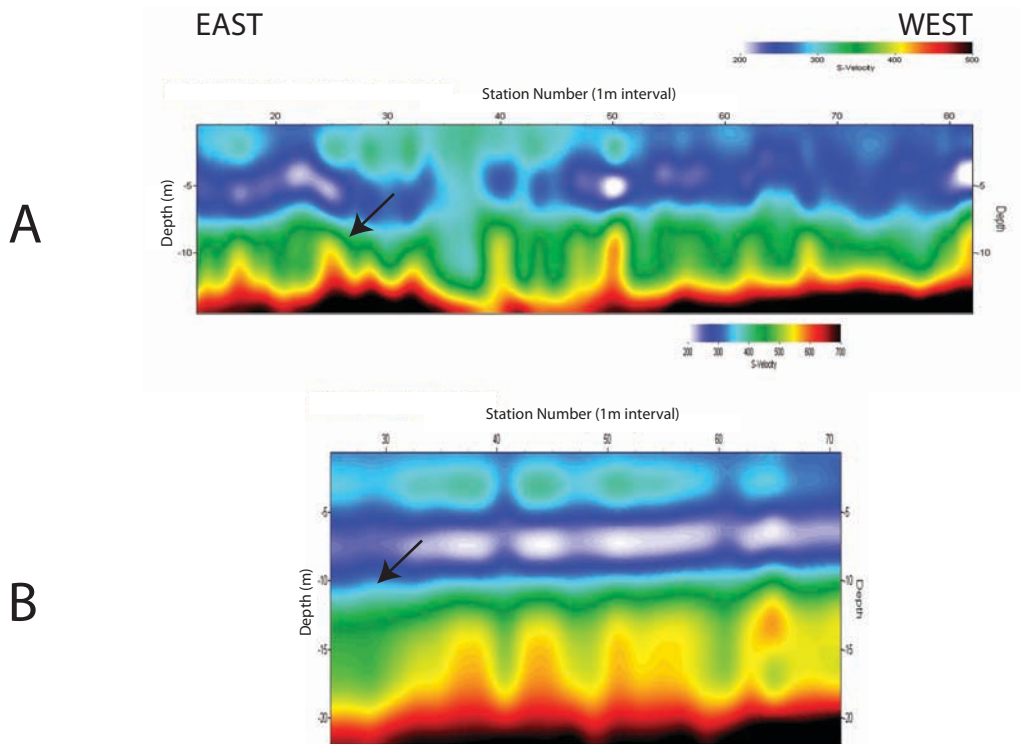


Figure 2.16: Active-source (A) and passive-source (B) models for Line G (VE = 1.2). The arrow indicates the 350 m/s contour.

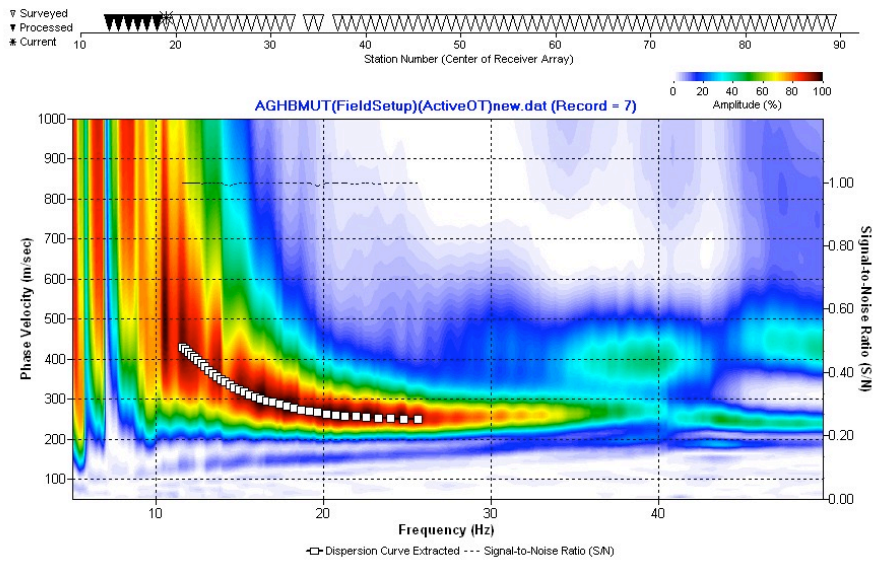
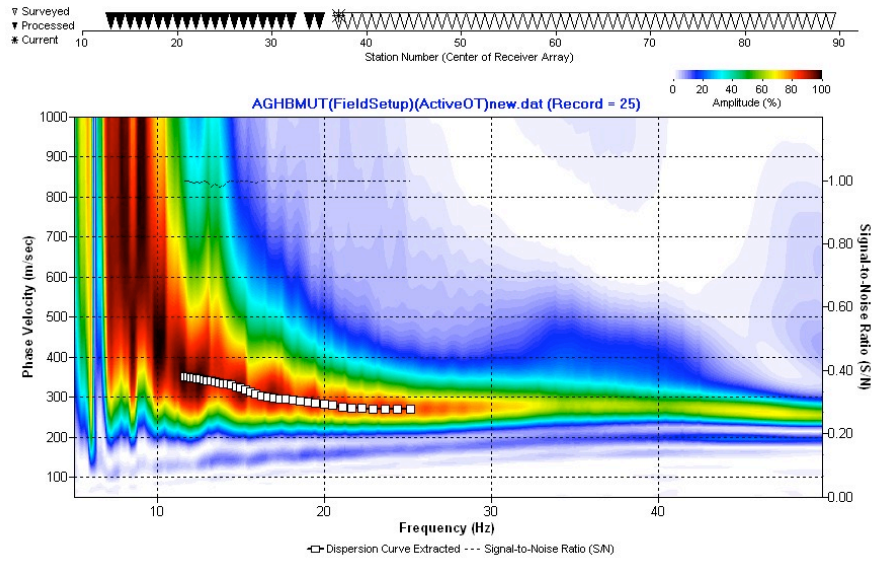


Figure 2.17: Active-source overtone image (amplitude contour plot) and dispersion curve picks (squares) for STA 19 on Line B.

A)



B)

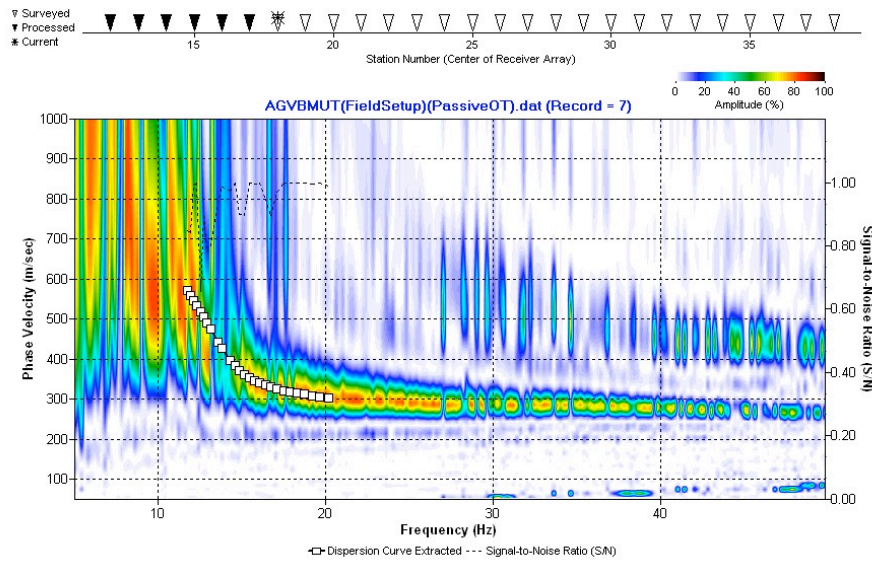
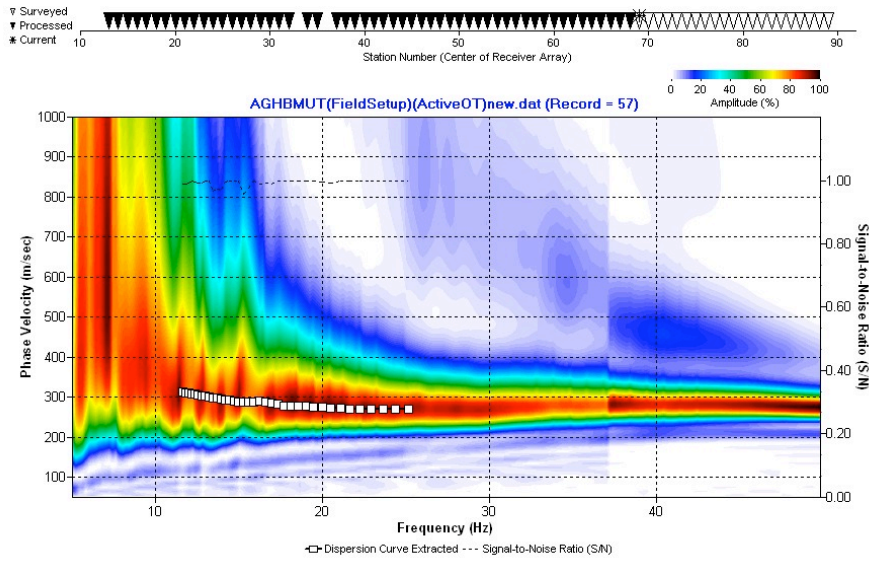


Figure 2.18: Overtone images (amplitude contour plots) and dispersion curve picks (squares) for STA 37 on Line B; A) active-source, B) passive-source

A)



B)

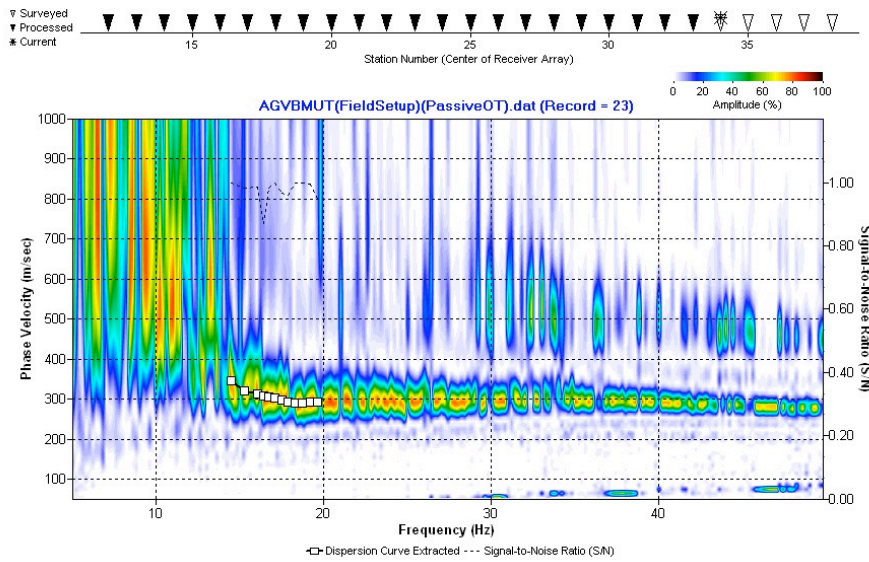
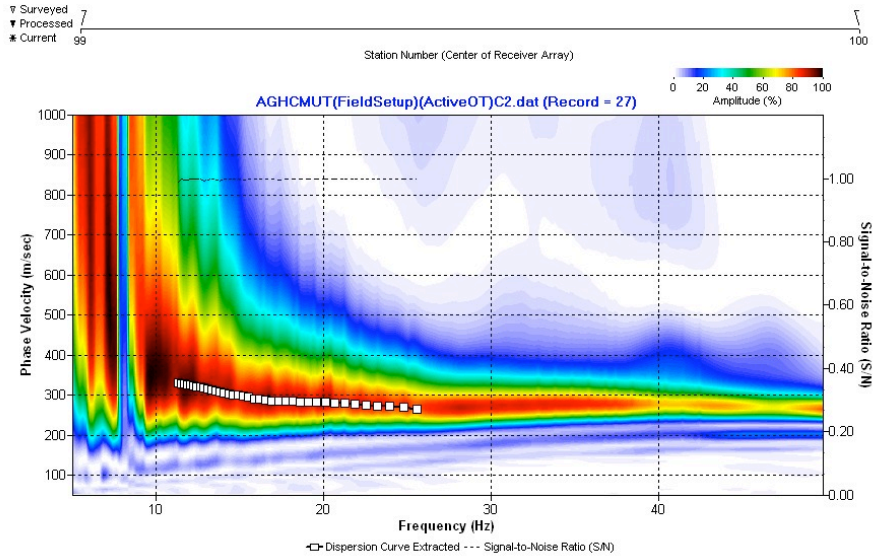


Figure 2.19: Overtone images (amplitude contour plot) and dispersion curve picks (squares) for STA 69 on Line B; (A) active-source; (B) passive-source.

A)



B)

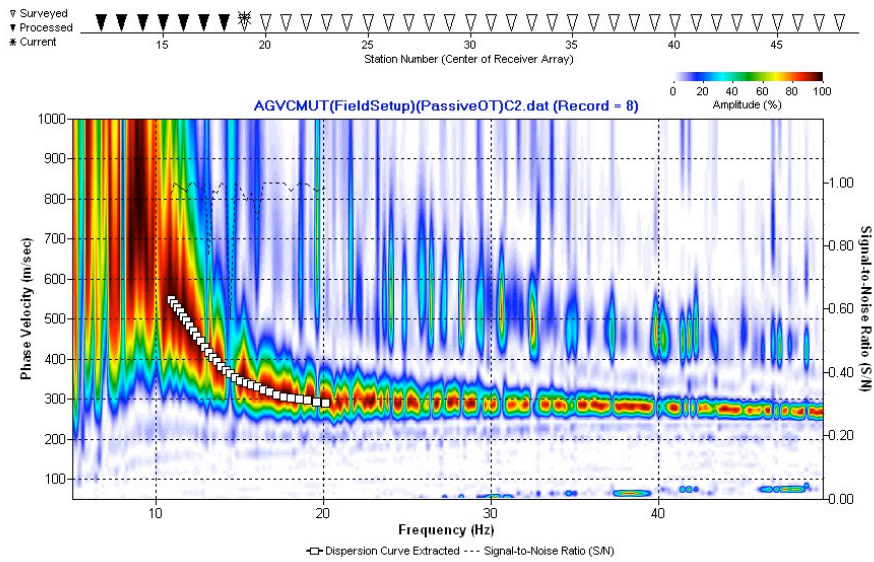
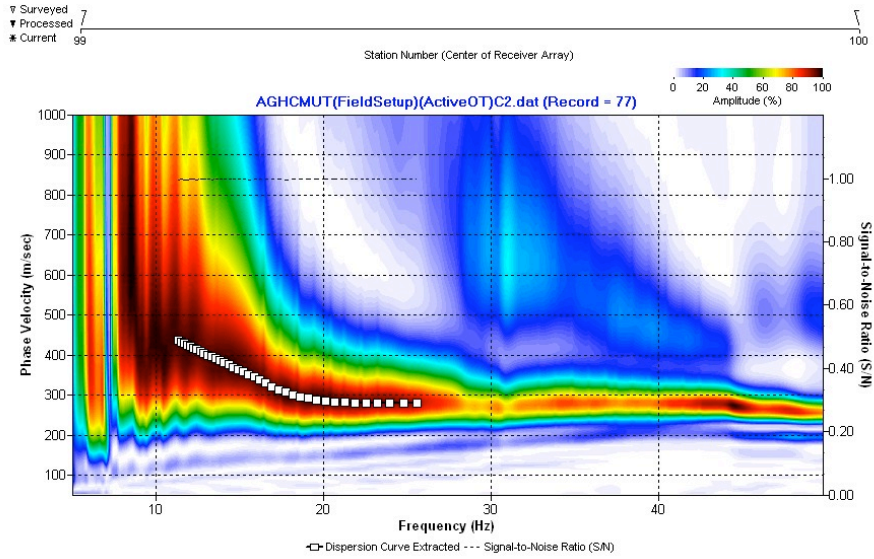


Figure 2.20: Overtone images (amplitude contour plots) and dispersion curve picks (squares) for STA 39 on Line C. (A) active-source; (B) passive-source.

A)



B)

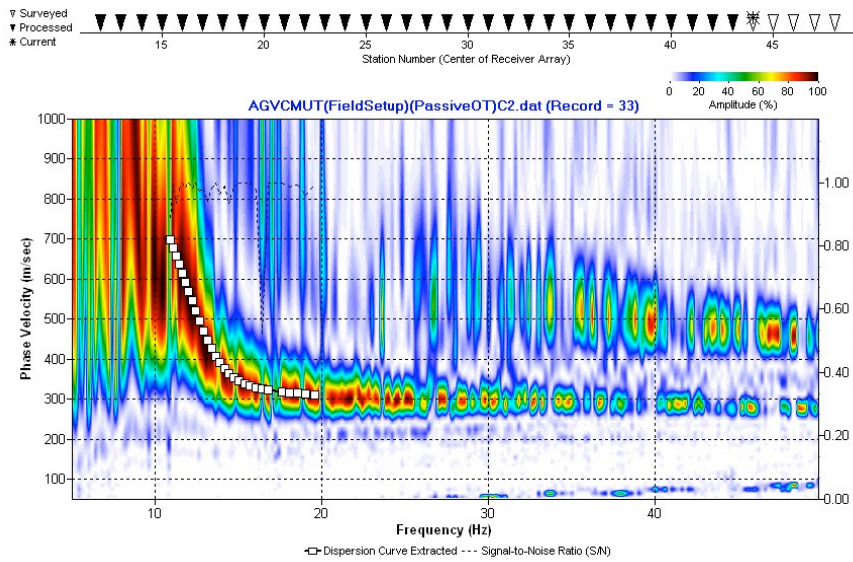


Figure 2.21: Overtone images (amplitude contour plots) and dispersion curve picks (squares) for STA 89 on Line C; (A) active-source; (B) passive-source.

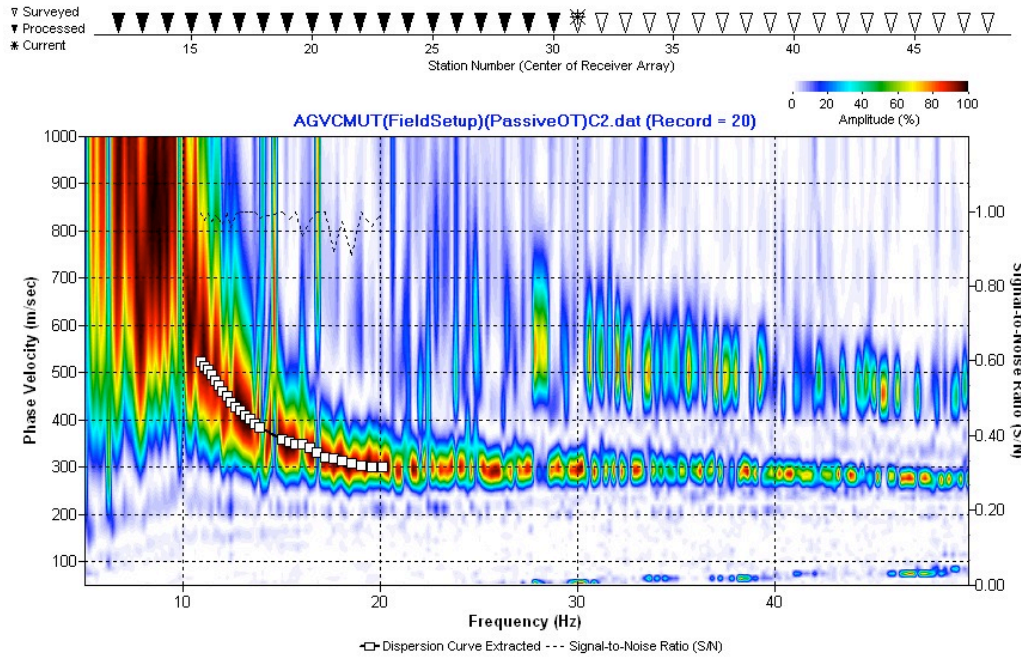
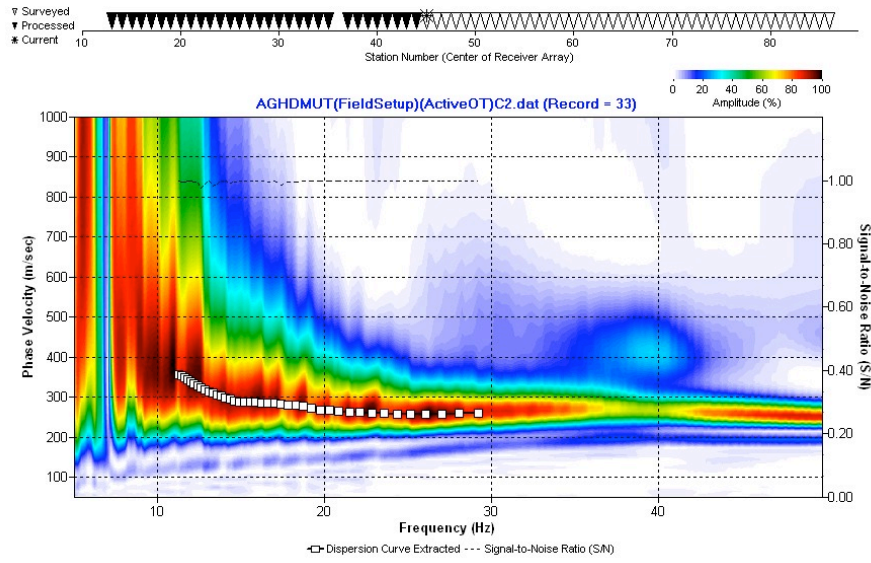


Figure 2.22: Passive-source overtone image (amplitude contour plot) and dispersion curve picks (squares) for STA 63 on Line C.

A)



B)

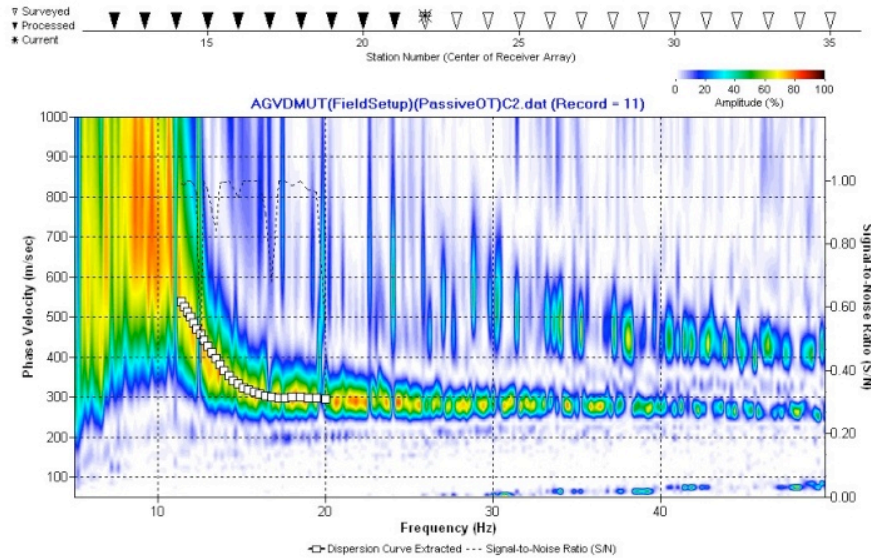
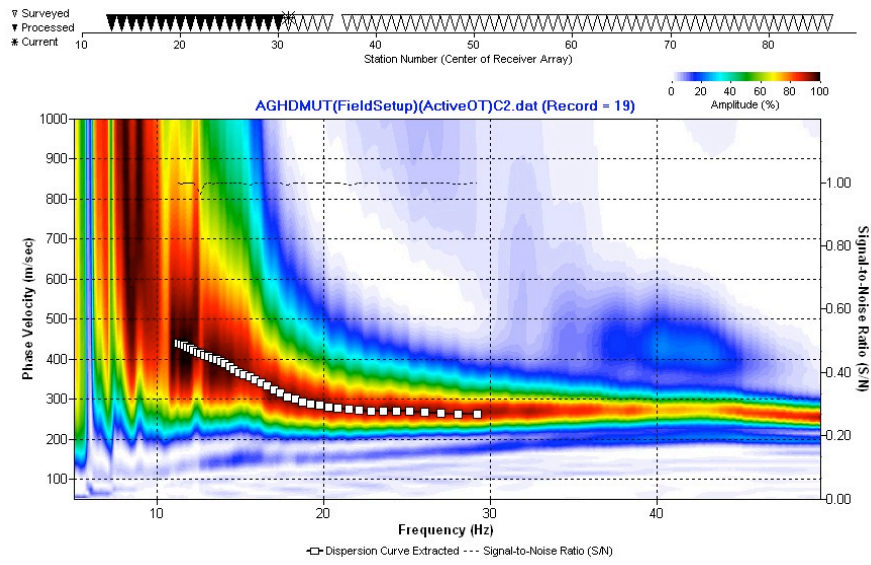


Figure 2.23: Overtone images (amplitude contour plots) and dispersion curve picks (squares) for STA 45 on Line D. A) active-source; B) passive-source.

A)



B)

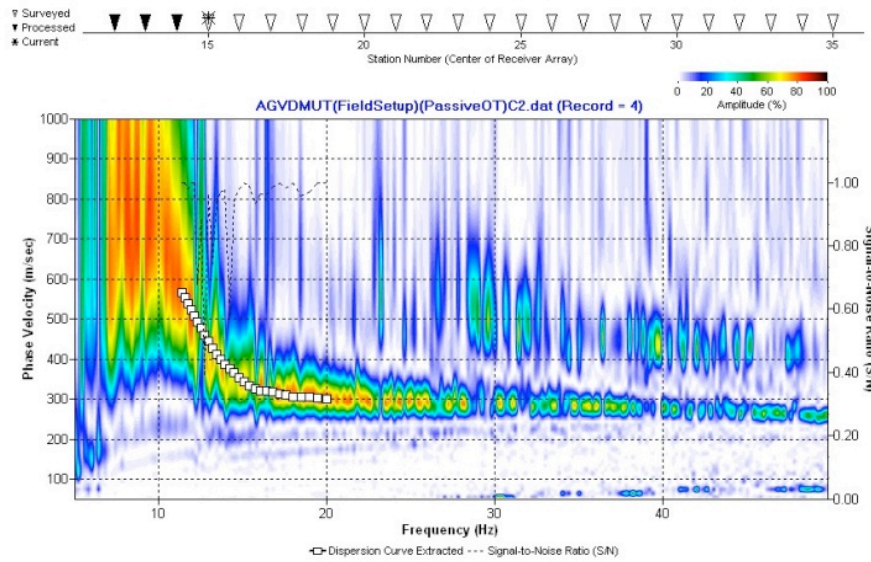


Figure 2.24: Overtone images (amplitude contour plots) and dispersion curve picks (squares) for STA 31 on Line D. A) active-source; B) passive-source.

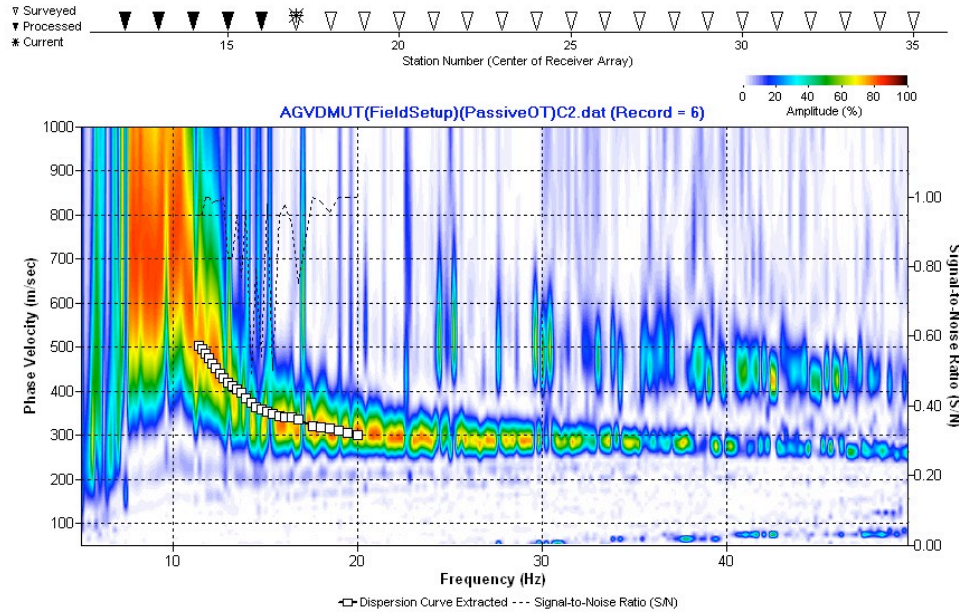


Figure 2.25: Passive-source overtone image (amplitude contour plot) and dispersion curve picks (squares) for STA 35 on Line D.

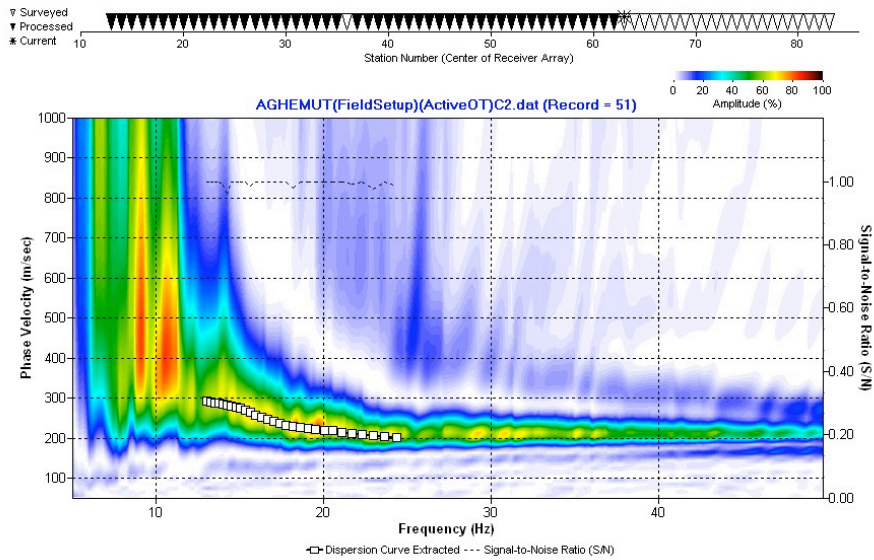


Figure 2.26: Active-source overtone image (amplitude contour plot) and dispersion curve picks (squares) for STA 63 on Line E.

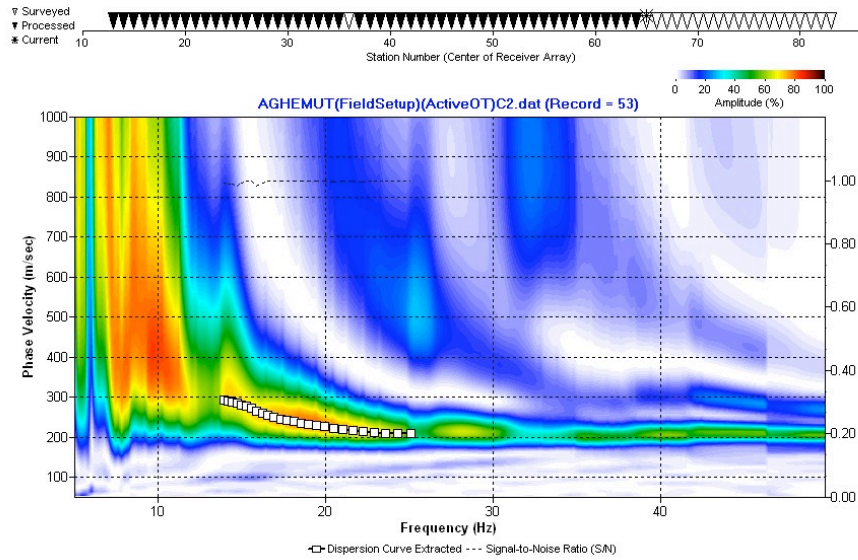


Figure 2.27: Active-source overtone image (amplitude contour plot) and dispersion curve picks (squares) for STA 65 on Line E.

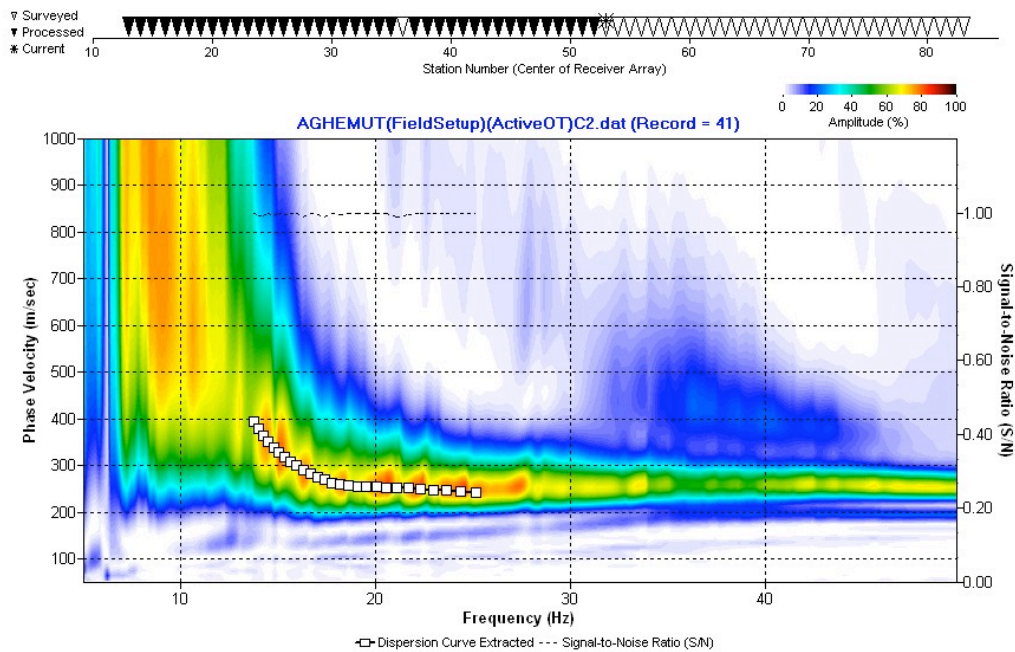
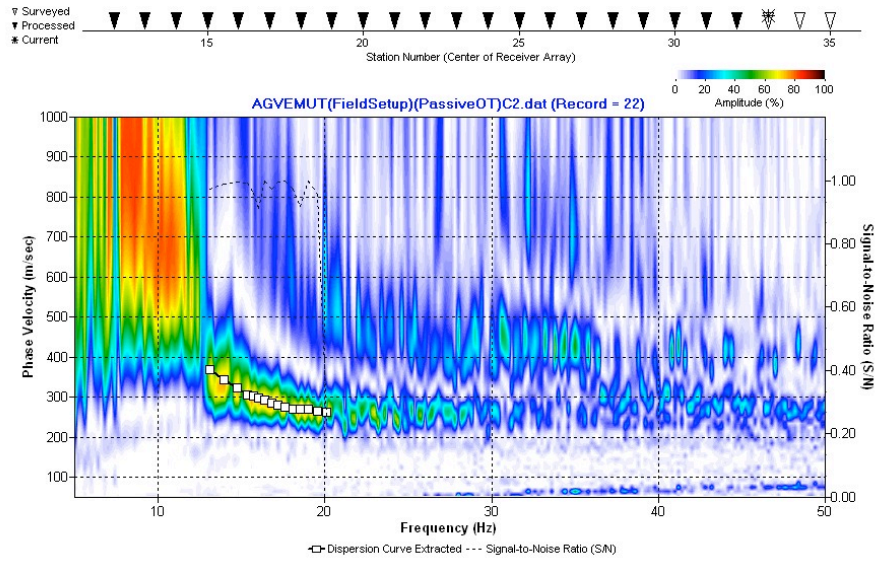


Figure 2.28: Active-source overtone image (amplitude contour plot) and dispersion curve picks (squares) for STA 53 on Line E.

A)



B)

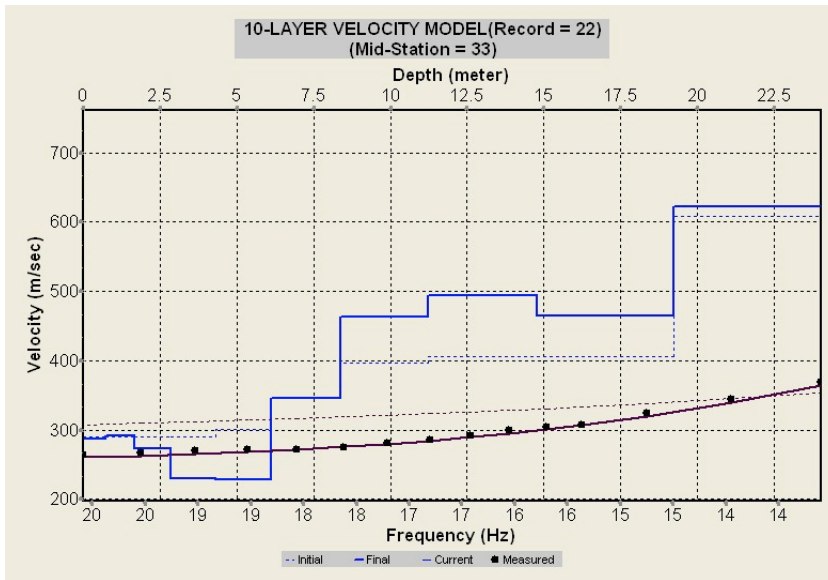
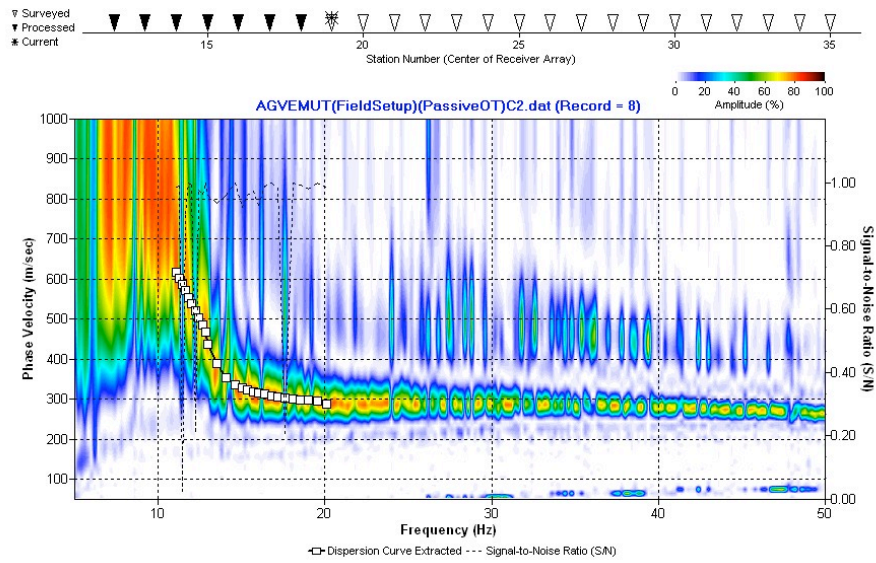


Figure 2.29: A) Passive-source overtone image (amplitude contour plot) and dispersion curve picks (squares) for STA 67 on Line E. B) 1-D shear-wave velocity model for STA 67 on Line E.

A)



B)

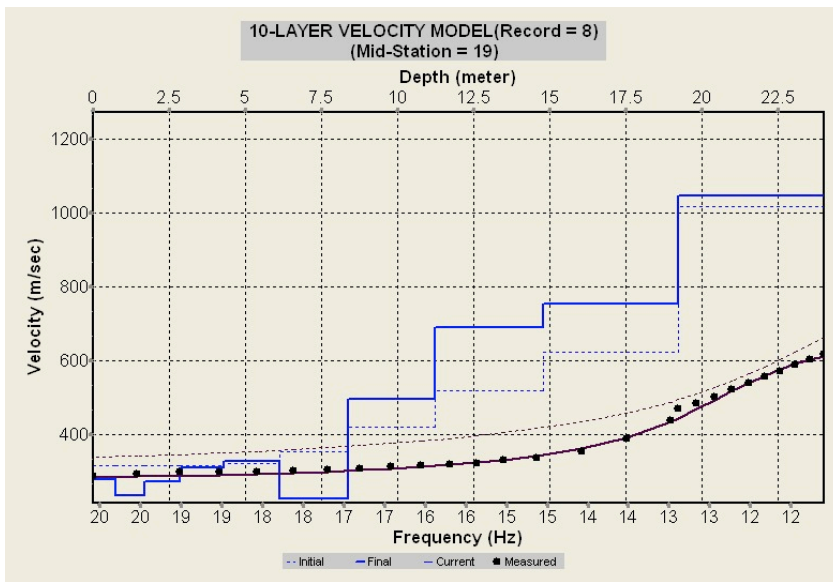


Figure 2.30: A) Passive-source overtone image (amplitude contour plot) and dispersion curve picks (squares) for STA 39 on Line E; B) 1-D shear-wave velocity model for STA 39 on Line E.

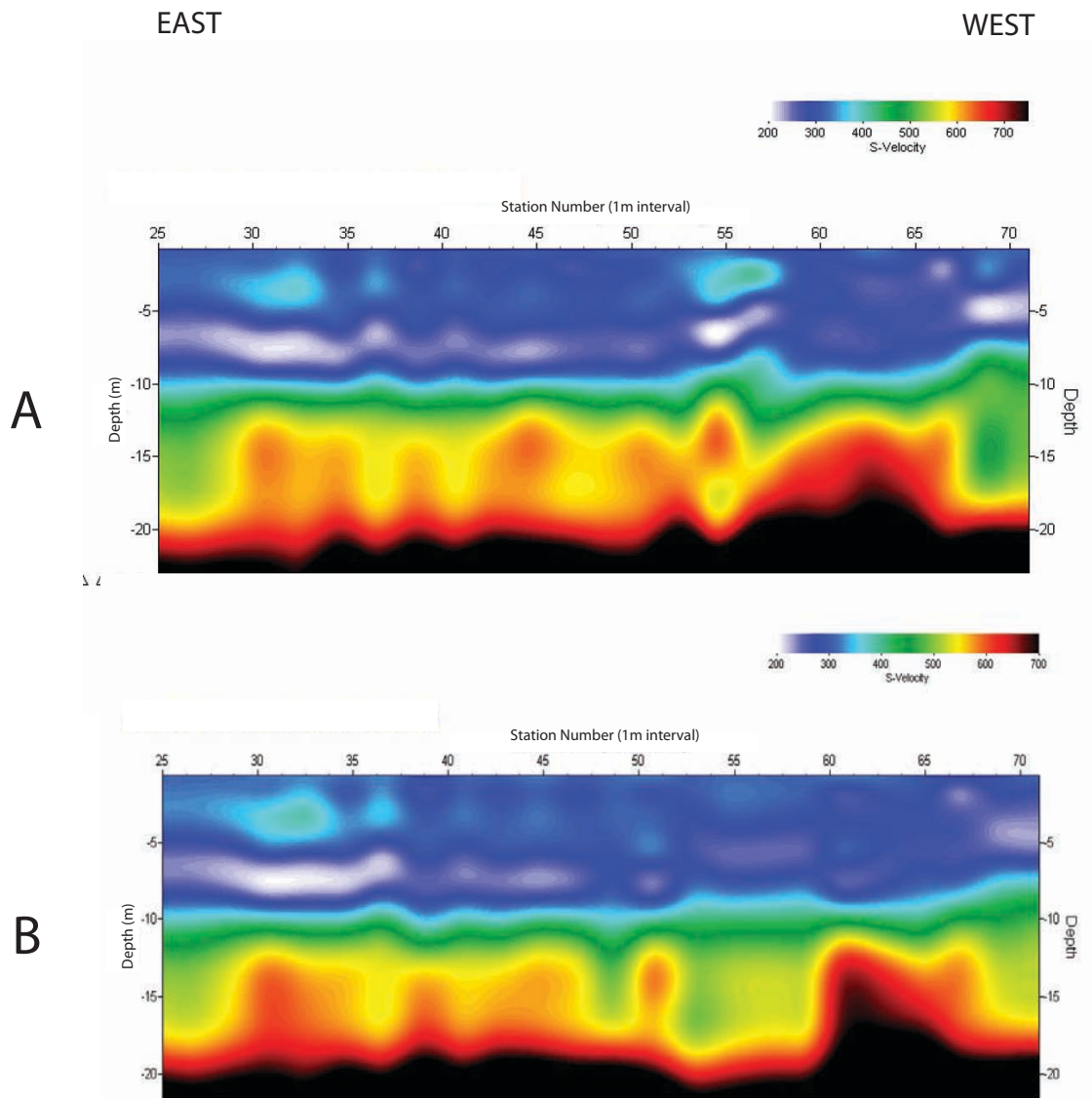
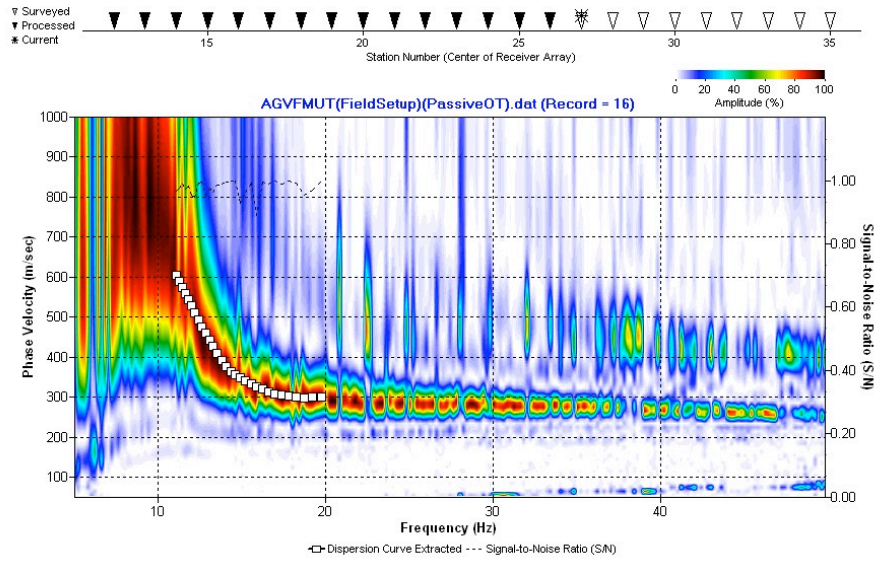


Figure 2.31: Passive-source models for Line F; A) Initial model showing the bull's eye feature below STA 55 at a depth of 15-20 meters (VE = 0.8); B) Alternative model generated with (3) alternate dispersion curves from STA 53, 55, and 57 (VE = 0.8).

A)



B)

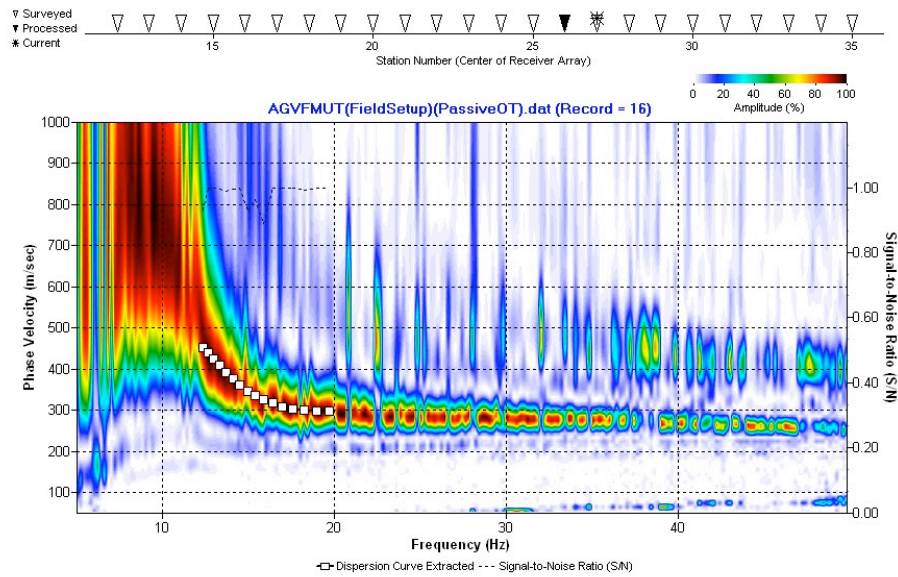
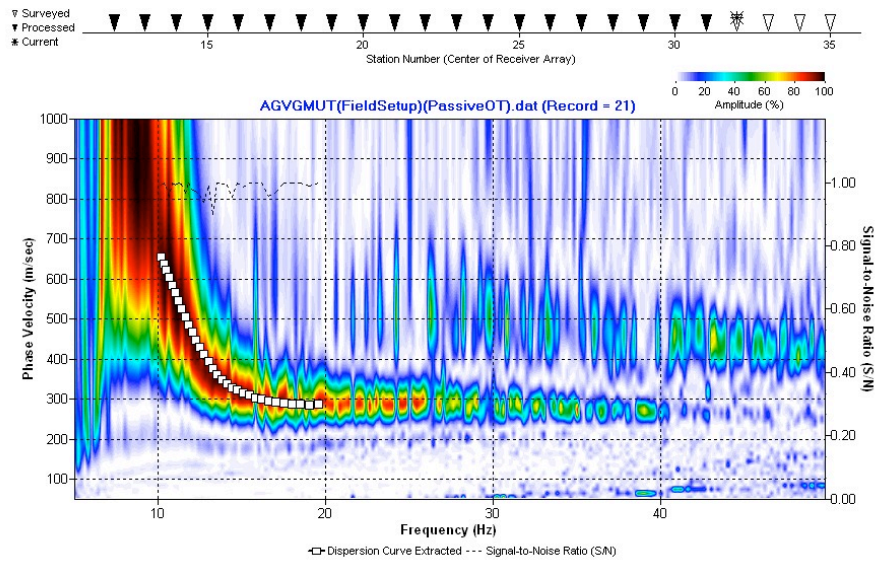


Figure 2.32: Passive-source overtone images (amplitude contour plots) and dispersion curve picks (squares) for STA 55 on Line F. A) Frequency range: 12-20 Hz; B) Frequency range: 14-20 Hz.

A)



B)

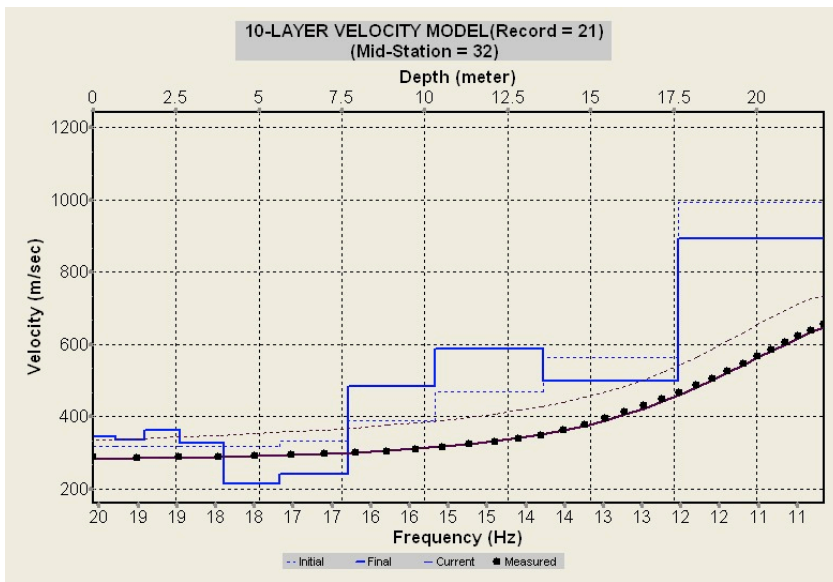


Figure 2.33: A) Passive-source overtone record (amplitude contour plot) and dispersion curve picks (squares) for STA 65 on Line G; B) 1-D shear-wave velocity model for STA 65 on Line G.

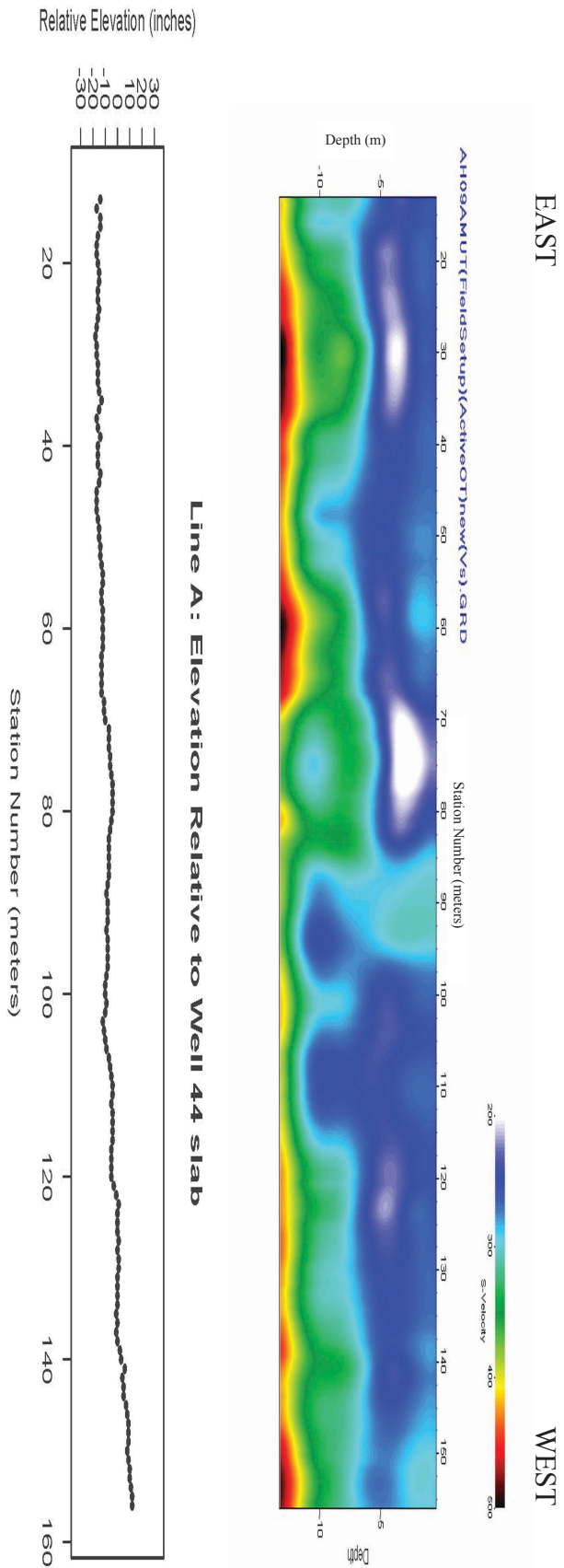


Figure 2.34: Active-source model (VE = 1.3) and topographic profile (VE = 5.3) for Line A.

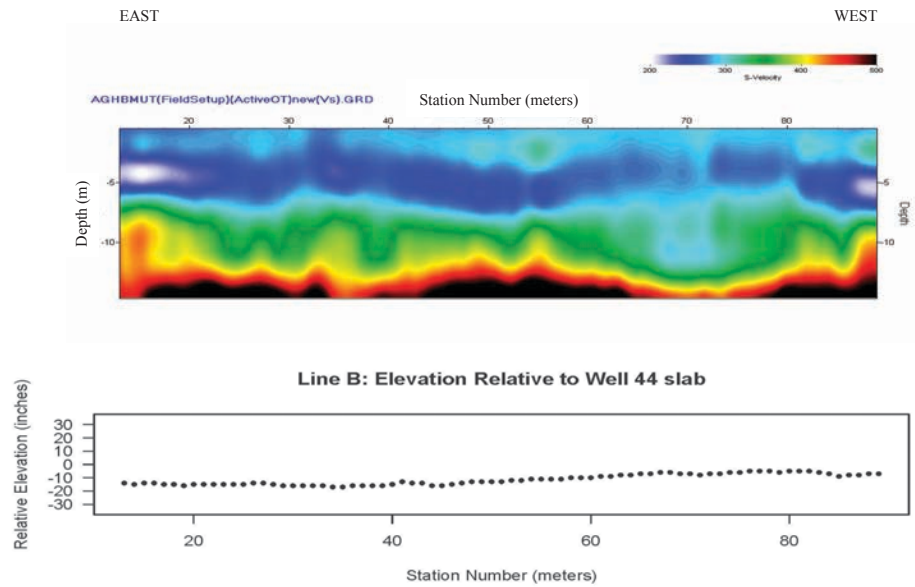


Figure 2.35: Active-source model (VE = 1.2) and topographic profile (VE = 5.3) for Line B.

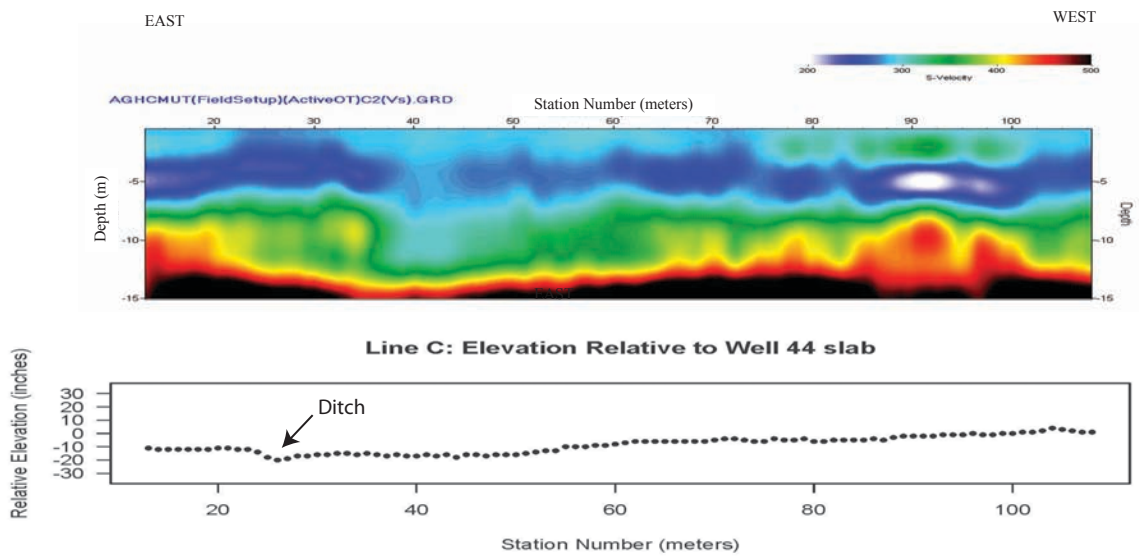


Figure 2.36: Active-source model (VE = 1.2) and topographic profile (VE = 5.3) for Line C.

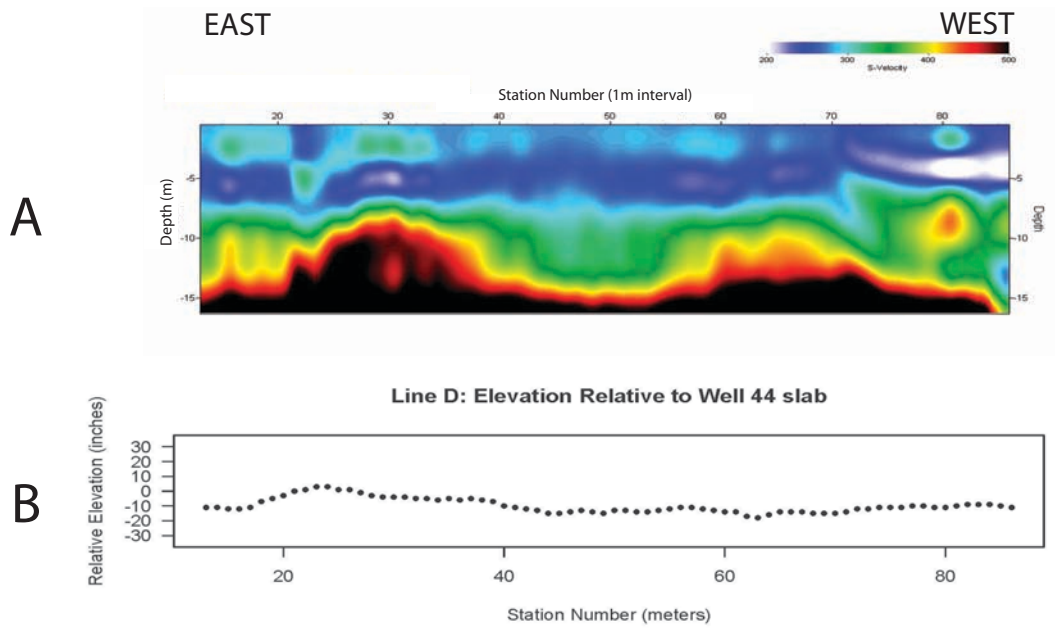


Figure 2.37: Active-source model (VE = 1.04) and topographic profile (VE = 5.3) for Line D.

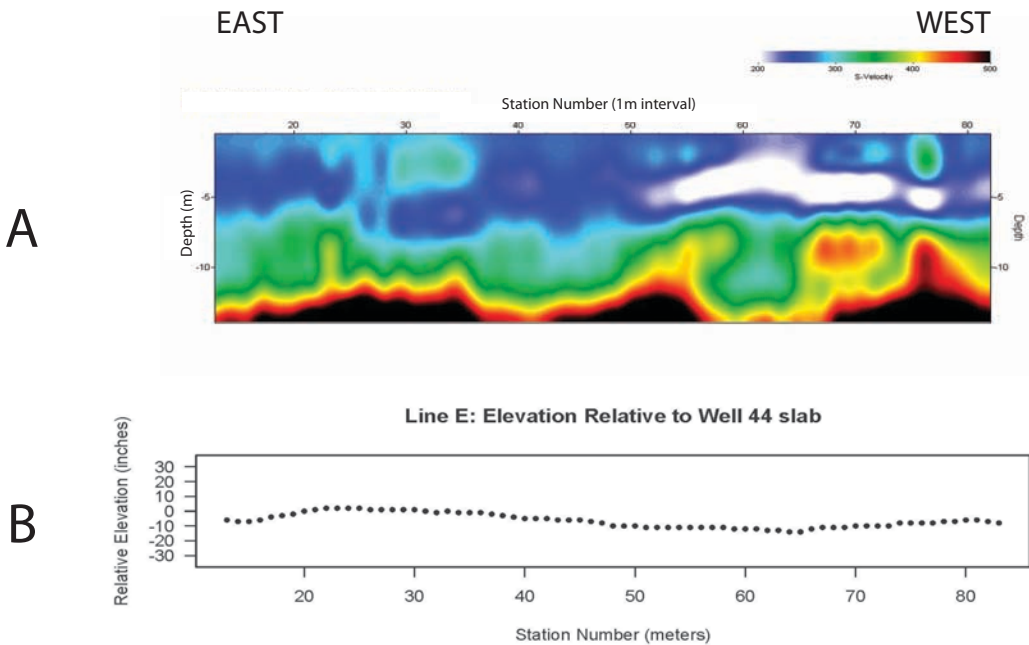


Figure 2.38: Active-source model (VE = 1.2) and topographic profile (VE = 5.3) for Line E.

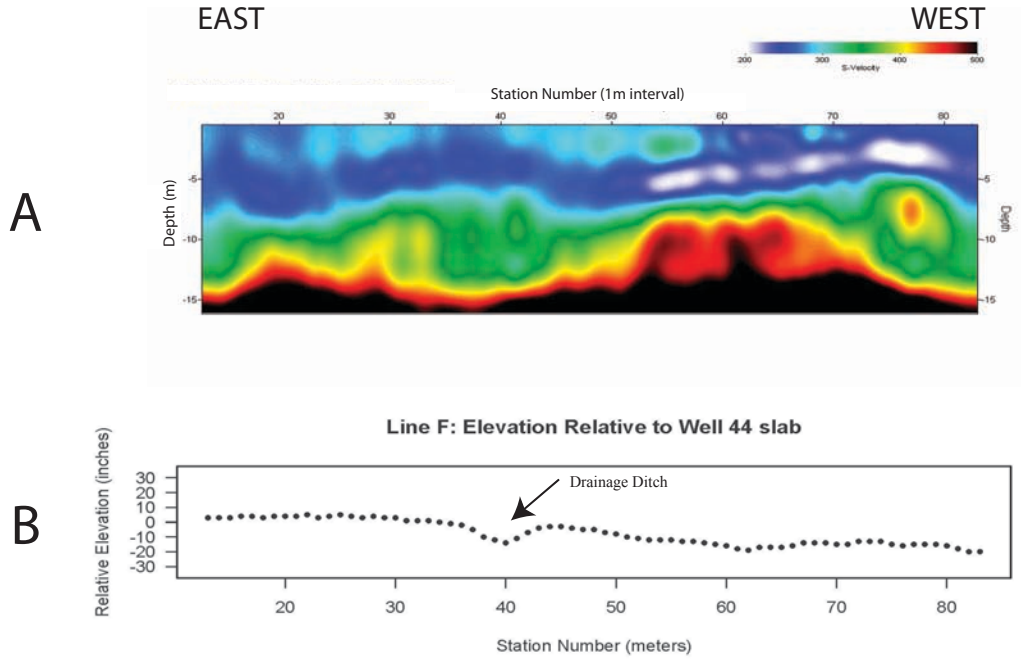


Figure 2.39: Active-source model (VE = 1.08) and topographic profile (VE = 5.3) for Line F.

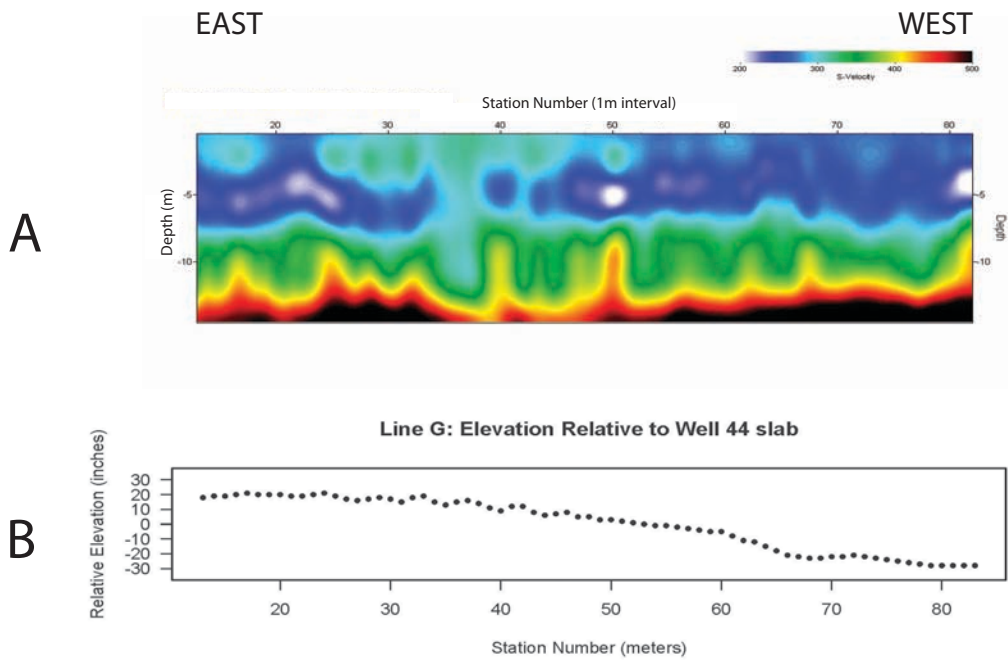


Figure 2.40: Active-source model (VE = 1.2) and topographic profile (VE = 5.3) for Line G.

CHAPTER 3

ALTERNATIVE SHEAR-WAVE VELOCITY MODELS FOR LINE A: EXPERIMENTATION WITH SPATIAL WINDOWING AND THE USE OF HALF-SPREADS

Alternative models for Line A were generated using more intensive processing techniques to enhance spatial resolution (Figures 3.1-3.3). Display and processing parameters are shown in Tables 3.1 and 3.2. Specific techniques and parameters are discussed for each model.

Model 1A

Model 1A (Figure 3.1) represents the preliminary model of the subsurface, and the general variability corresponds with the expected karst geology. The model extends to a depth of approximately 15 meters, which is consistent with the geophone spread for the active survey. The lowest frequency used for the analysis was 10 Hz, and this lower limit was determined by analyzing the spectral characteristics of the overtone records. The upper frequency limit typically ranged from 30 to 100 Hz, and the variability resulted from the quality of the overtone records. Dispersion 1 was used for the analysis, and muting was not performed on the seismic records.

Borehole data obtained from the USGS Water Science Center in Atlanta, GA was used to constrain the geophysical interpretation. Well #44 is located approximately 27 meters from Line A (Figure 1.7), and the depth to bedrock (soft limestone) from the borehole log is 9 meters (Figure 1.4). The surface-wave model displays an abrupt

transition (steep vertical gradient) in shear-wave velocity at a depth of 8 to 14 meters. This transition is interpreted to be the soil-bedrock interface. The velocity of the soil appears to range from 200 to 350 m/s. Based on the steep velocity gradient and correlation with well data, areas where shear-wave velocity exceeds approximately 350 m/s are interpreted to be limestone bedrock. The more gradual variations in shear-wave velocity below the bedrock surface (steep velocity gradient) are interpreted as variations in fracture volume. Prominent low-velocity anomalies beneath STA 70-80 and 90-112 likely indicate preferential weathering, paleokarst, or sinkhole formation.

Analysis of the data itself provides a qualitative basis for confidence in the model. Figure 3.4A represents a shot gather possessing distinct, high amplitude surface waves with little noise or interference. The fundamental mode is clearly defined in the overtone record (Figure 3.5). Thus confidence in dispersion curve picks is relatively high, as reinforced by the high signal-to-noise ratio. Examination of other individual shot gathers and overtone records can yield insight about the overall integrity of the profile.

Unfortunately, many overtone records do not possess such high resolution of the fundamental mode. Several concerns arise after examination of the overtone records. Figure 3.6 shows an example of contamination of the fundamental mode surface wave by higher mode energy at frequencies greater than 30 Hz. Figure 3.7 is a unique situation in which the dispersion curve seems to branch at higher frequencies, and it is unclear which branch represents the fundamental mode. In Figure 3.8, the overtone image lacks the distinct expression of the fundamental mode surface wave, so picking an accurate dispersion curve becomes unrealistic. In these cases, the dispersion curves must be picked within a more limited frequency range, or the record must be omitted altogether from the

inversion procedure. In order to address these issues, more intensive data processing was implemented to improve the quality of the final profile. The procedures are discussed in the following sections.

Model 2A

Model 2A is an alternative subsurface model generated using more intensive processing techniques (Figure 3.1). A ‘wedge mute’ was applied to the seismic records in order to remove P-wave and higher-mode surface-wave energy from the phase velocity-frequency plot, while minimizing the loss of energy in the fundamental mode. In this procedure, traces were zeroed above a user-specified line that defined a time window dominated by P-waves and higher-mode surface waves (Figure 3.4B). The intent was to minimize contamination and sharpen the image of the fundamental mode for improved dispersion curve picks. The extent of the wedge mute was determined for each individual record by examining the overtone records before and after muting. Some records did not benefit from the muting procedure, so the dispersion curve picks from the un-edited data were used in the inversion. As noted in Chapter 2, muting proved to be a sensitive procedure because it always removes the lowest frequencies of the fundamental mode along with portions of the higher modes.

The following examples of overtone records and corresponding dispersion curves illustrate the subtle effects of muting. In addition to the obvious consequence of eliminating the higher-mode surface wave, the wedge mute seems to produce two distinct results for the fundamental mode. First, the distinct up-warping of the dispersion curve at higher frequencies is eliminated, and the curve noticeably flattens. The second general result of muting is an apparent increase in the phase velocity at lower frequencies (down

to the lower frequency limit of 10 Hz). Muting tests by Ivanov et al. (2005) indicate that the apparent increase is an over-estimate or artifact generated by the loss of energy in the fundamental mode at the lowest frequencies. Figures 3.9-3.13 show the effects of muting on several overtone records.

Despite the possible artifacts at low frequencies, the velocity model derived from the muted gathers (Model 2A) compares well with Model 1A. Once again, the depth to bedrock ranges from 8-14 meters. Overall, the low velocity anomalies within the bedrock are somewhat less pronounced, and the low-velocity zone (LVZ) between STA 100 and 125 is less distinct on Model 1A.

Model 3A

Model 3A (Figure 3.1) is an enhanced model of the subsurface generated using trace muting techniques and trace sub-set analysis (or “spatial windowing”). The effect of the ‘wedge mute’ is evident from different overtone records derived from the seismic record for STA 152. The original shot gather is shown in Figure 3.4A, and the overtone image is shown in Figure 3.14A. The wedge mute was applied to the same record (Figure 3.4B), and the new overtone image (Figure 3.14B) illustrates the improvement of resolution of high frequencies.

Trace sub-set analysis refers to the process of selecting smaller sub-sets of traces for the overtone analysis to improve spatial resolution. For Line A, a careful analysis of the individual shot gathers yielded an important observation. A distinct change in slope of the fundamental mode surface wave is evident from STA 78 to 87 (Fig. 3.15A). In this section, the abrupt increase in slope is a direct indication of an abrupt decrease in shear-wave velocity directly beneath these stations. The effect is seen consistently for stations

78-87 as the source and array are moved. Beyond STA 87, the slope decreases again. Since each 1-D profile represents an average across 24 traces, the extent of a small anomaly such as this is likely to be distorted in the resulting 2-D velocity model. The effects of the LVZ before sub-set processing can be identified on the overtone records. The dual nature of the fundamental mode surface wave is manifested as a branching of the dispersion curve at higher frequencies. Figure 3.7 shows an example of this effect. Spatial windowing was used to isolate the LVZ and avoid the negative effects of averaging.

Starting at STA 71, traces within the LVZ were excluded from the overtone analysis. The traces constituting the LVZ were processed separately, and sub-sets of traces were used on both sides of the LVZ (Table 3.3). The sub-sets provide better lateral resolution, but the reduced number of traces used in each overtone analysis limits the depth of penetration. For example, overtone image for STA 82 represents only 7 traces (Fig. 3.15B), so the frequency range is only 45-110 Hz. In addition, there are two significant gaps in the mid-point coverage of the profile. Nonetheless, lower average shear-wave velocities are clearly evident, and the void/sinkhole is well defined on the final profile (Figure 3.1). Surfseis uses an interpolation scheme to estimate gaps in the data set for the shear-wave profile.

The depth to bedrock is still consistent with Model 1A, as indicated by the shear-wave velocities in excess of 350 m/s at 8-14 meters. Although the similarities between the two models are somewhat inconspicuous, the general bedrock topography roughly matches on both models. Model 3A illustrates the importance of noting trends on the

seismic records prior to processing with Surfseis. Breaking up the records into sub-sets of traces improved the spatial resolution of an important anomaly.

Model 4A

Model 4A represents an attempt to gain improved mid-point coverage in the low velocity zone (Figure 3.2). As with Model 3A, the gathers were divided into sub-sets of traces, but the trace sub-sets were isolated using Winseis prior to processing with Surfseis. The intent was to retain the original mid-point locations across the geophone spread while simultaneously analyzing trace-subsets within and beside the LVZ. Unfortunately, Surfseis used the mid-points for the trace subsets instead of the mid-points for the original 24-trace spread. The major LVZ appears as a wider anomaly, and the anomaly at STA 25 is characterized by a closed, circular low-velocity region rather than a depression in the shear-wave velocity structure. Despite the differences in the appearance of Models 3A and 4A, the depth to bedrock on both models is very similar.

Model 5A

The objective for Model 5A (Figure 3.2) was to obtain better resolution of near-surface shear-wave velocities using a sub-set of the 24 traces for each seismic record. For this model, the middle twelve traces (7-18) were isolated for better resolution of the upper 4-5 meters of the subsurface. This decreased the resolution width to about 5 meters. As before, there is a trade-off with this approach. The lower frequencies are lost, but the lateral resolution is improved because a smaller number of traces are averaged. The minimum frequency used in the analysis was 30 Hz, and the depth of the profile is 4 meters. The major features and shear-wave velocities are consistent with the upper 4 meters of Model 3A. The low velocity zone in the center of the profile persists and is now

fully resolvable. The shear-wave velocities themselves do not exceed 350 m/s in the upper 4 meters, which is consistent with the previous profiles. There is also a circular low velocity zone at STA 130 at a depth of 3-5 meters on both profiles. It is possible that this indicates a potential collapse feature such as a void.

Model 6A

The passive seismic survey was designed to complement the active survey by increasing the depth of penetration. The moving van produced slightly lower frequencies (8 Hz), and the corresponding profiles are reliable to a depth of approximately 23 meters (half of the geophone spread), as opposed to 12 meters for the active survey. The trade-offs inherent in MASW surveys are once again apparent. The geophone spread was 46 meters for the survey, so depth penetration is improved at the expense of lateral resolution (~23 meters). The objective of the survey was to provide a broad image of the sub-surface at greater depth for comparison with results from the active survey.

Model 6A (Figure 3.3) represents the results of the passive survey using the following processing parameters: 8-50 Hz frequency range, 50 data points, and smoothing value of three. The increased depth of penetration corresponds with a larger range of shear-wave velocity (200-700 m/s), presumably due to more competent limestone at depth. Figure 3.16A is a typical example of a seismic record from the passive survey, and Figure 3.16B is an enlarged view of the first 1000 milliseconds. The records appear very different from the active survey records due to the continuous energy, but the overtone records are nearly the same (Fig. 3.17). The energy peaks on the passive overtone records are less continuous for reasons noted in Chapter 2, but the dispersion curves were still chosen based on the high signal-to-noise ratio.

The features from Model 6A were then compared with the active survey models. The soil-bedrock interface at 10 meters, where shear-wave velocity exceeds 350 m/s, is consistent with the borehole log from well #44 and averages across the active survey profile. The passive survey has detected the lateral variations within the limestone bedrock (due to variations in fracture density?) extending to greater depths, as indicated by shear wave velocities ranging from 400 to 600 m/s below 15 meters. The prominent LVZ on Model 3A does not appear on Model 6A because it is much narrower than the ~23 meter resolution width of the passive array.

Model 7A

Model 7A (Figure 3.3) is an alternative model for the subsurface to a depth of approximately 23 meters. The slight change in parameters (frequency range: 8-25 Hz; 30 data points; smoothing; 5) alters the profile, but the general features are consistent with Model 6A. The soil-bedrock interface (interpreted as the transition to velocities greater than 350 m/s) is between 10 and 12 meters. A residual clay layer derived from weathering of the bedrock may be present directly above the limestone, as indicated by well logs from engineering reports. Below 15 meters, the transition from velocities between 400-600 m/s to velocities between 600-700 m/s is likely associated with a decrease in fracture density. A typical overtone record and dispersion curve is shown in Figure 3.18.

Subtle depressions in the velocity structure (i.e. local decreases in shear-wave velocity) can also be correlated with Model 6A. At the extreme ends of both profiles, low-velocity zones below 10 meters are clearly visible. Low-velocity areas between STA 60-70 and 110-120 also appear on both profiles. However, the distinct circular anomaly

at STA 80 at a depth of 20-25 meters is not as pronounced on Model 6A. This anomaly correlates with the LVZ on Model 3A (Figure 3.1).

Model 8A

Model 8A (Figure 3.3) is another alternative passive-source model for Line A. As in Model 6A, the frequency range used for picking dispersion curves was 8-50 Hz (Figure 3.19), but the averaging window used to smooth the phase velocity picks was increased to five points. There are clearly differences with the previous passive profiles, but the major features persist. Shear-wave velocity below 10 meters is generally lower than Model 7A, but the soil-bedrock interface is still located at a depth of 10-13 meters. Anomalous zones are still evident at STA 30-40 and 110-140, and the circular velocity anomaly at STA 80 can also be correlated with Model 7A.

Discussion: Line A

The geophysical interpretation for Line A agrees with borehole data and surficial evidence of local karst processes. The high number of sinkholes in the area indicates that subsidence is very active, and the variations in velocity observed in the profiles may be associated with preferential weathering along bedrock fractures. Although the resolution limits vary between the active (6 and 12 m) and passive-source surveys (23 m), geologic features can be correlated between both surveys. The active survey provides a more detailed view of the upper 12 meters of the subsurface, while the passive survey offers a broader glimpse of the geology to a depth of 23 meters. The previous models illustrate that there is no unique solution for the MASW technique. The specified parameters clearly influence the resolution, so it is imperative to choose values in accordance with the target geology.

The LVZ between STA 78 and 87 provides an unequivocal reference point to compare the shallow, intermediate, and deep profiles. Although the resolution limits are very different, similar velocity information appears on each profile. These consistent results indicate the usefulness of MASW at different scales. The LVZ is prominent on the shallow and intermediate profiles, but it is far more subtle and elongated on the deep profile. The averaging effects associated with processing different sets of trace gathers accounts for the differences in lateral and vertical resolution. Therefore, it is helpful to process the data in different ways in order to evaluate the inherent trade-offs associated with the method and determine what features of the models are robust.

Preferential weathering along fractures within the Ocala limestone may be responsible for the variation in bedrock competence. The regions of lower rigidity indicated by low-velocity zones at depth probably control the locations of sinkholes at the surface due to the movement of sediment along fractures in the limestone. In general, the passive survey provides a broad framework for interpretations within this karst landscape. The correlation of the LVZ between the active and passive profiles suggests that broad trends in the velocity structure at depth may be used to infer areas of potential subsidence. Depressions in the velocity structure at STA 30-40, 60-70, and 130-140 may be susceptible to collapse due to voids within highly fractured bedrock. An alternative interpretation is the presence of paleo-karst features (Miller et al., 2005). There is considerable lateral smearing of the LVZ at STA 78-87 on the passive profiles. If the void is located within relatively competent bedrock, the averaging effect across the spread likely obscures the anomaly. Therefore, comparison of active and passive profiles can provide a more comprehensive understanding of the subsurface conditions.

Table 3.1: Display Parameters for Line A

Display Parameters for Overtone Records	
Frequency Range	5-100 Hz
Phase Velocity Range	50-1000 m/s
Contrast	1

Table 3.2: Processing Parameters for Line A

Seismic Models - Line A						
<u>Profile</u>	<u>Source</u>	<u>Traces</u>	<u>Mute</u>	<u>Data Pts</u>	<u>Smoothing</u>	<u>Freq. Range (Hz)</u>
1A	Active	Full	No	30	3	> 10
2A	Active	Full	Yes	30	3	> 10
3A	Active	Sub-sets	Yes	30	3	> 10
4A	Active	Modified	No	30	3	> 30
5A	Active	7-18	Yes	30	3	30-50
6A	Passive	Full	No	50	3	8-50
7A	Passive	Full	No	30	5	8-25
8A	Passive	Full	No	50	5	8-50

Table 3.3: Spatial Windowing: Analyzing subsets of traces

Spatial Windowing			
<u>Seismic Record</u>	<u>Traces</u>	<u>Mid-Point</u>	<u>Traces within LVZ</u>
1059	1-18	1068.5	No
1060	1-17	1069	No
1061	1-16	1069.5	No
1062	1-15	1070	No
1063	1-14	1070.5	No
1064	1-13	1071	No
1065	1-12	1071.5	No
1066	1-11	1072	No
1067	11-20	1082.5	Yes
1068	11-19	1083	Yes
1069	11-18	1083.5	Yes
1070	11-17	1084	Yes
1071	7-16	1084.5	Yes
1072	Invalid	Floating Point	N/A
1073	15-22	1091.5	No
1074	14-23	1092.5	No
1075	13-24	1093.5	No
1076	12-24	1094	No
1077	11-24	1094.5	No
1078	10-24	1095	No
1079	9-24	1095.5	No
1080	8-24	Invalid	N/A
1081	7-24	1096.5	No
1082	6-24	1097	No
1083	5-24	1097.5	No
1084	4-24	1098	No
1085	3-24	1098.5	No
1086	2-24	1099	No

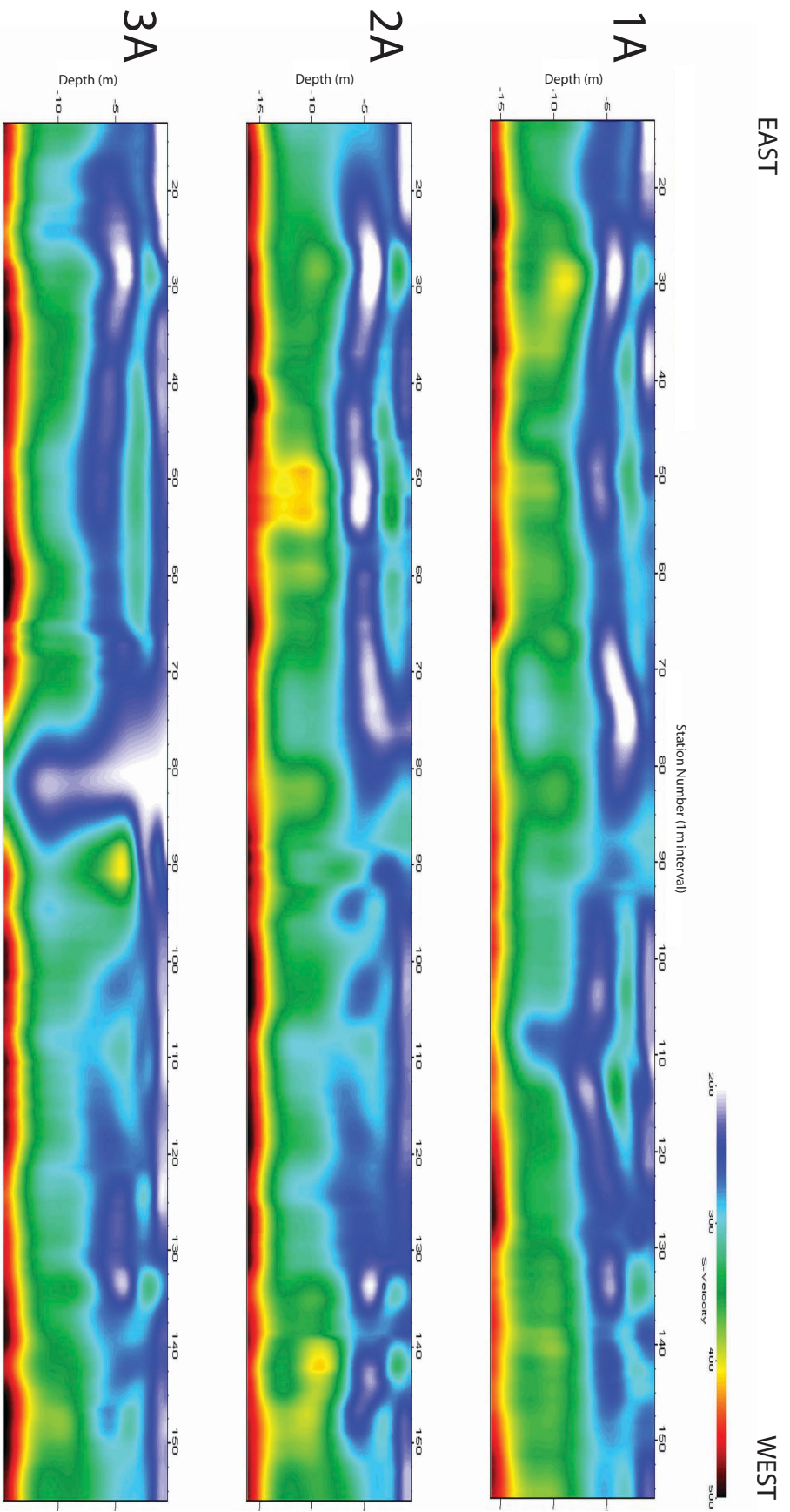


Figure 3.1: Alternative models for Line A ; (1A) No muting (VE = 1.1); (2A) Wedge mute (VE = 1.1); (3A) Wedge mute and spatial windowing (VE = 1.2).

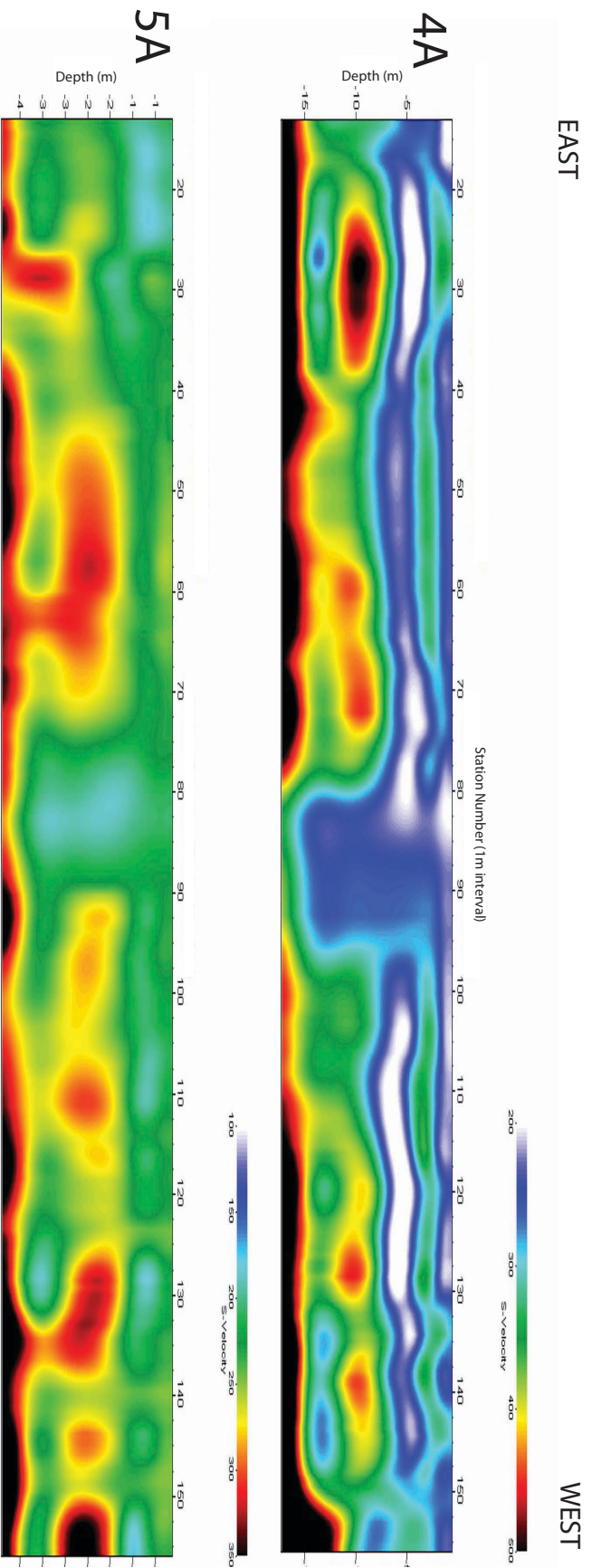


Figure 3.2: Alternative models for Line A; (4A) Sub-sets of traces were processed to isolate the low-velocity zone from STA 78-87 (VE = 1.0); (5A) Half of the traces (7-18) were processed to improve lateral resolution of the upper 4 meters of the subsurface (VE = 4.5).

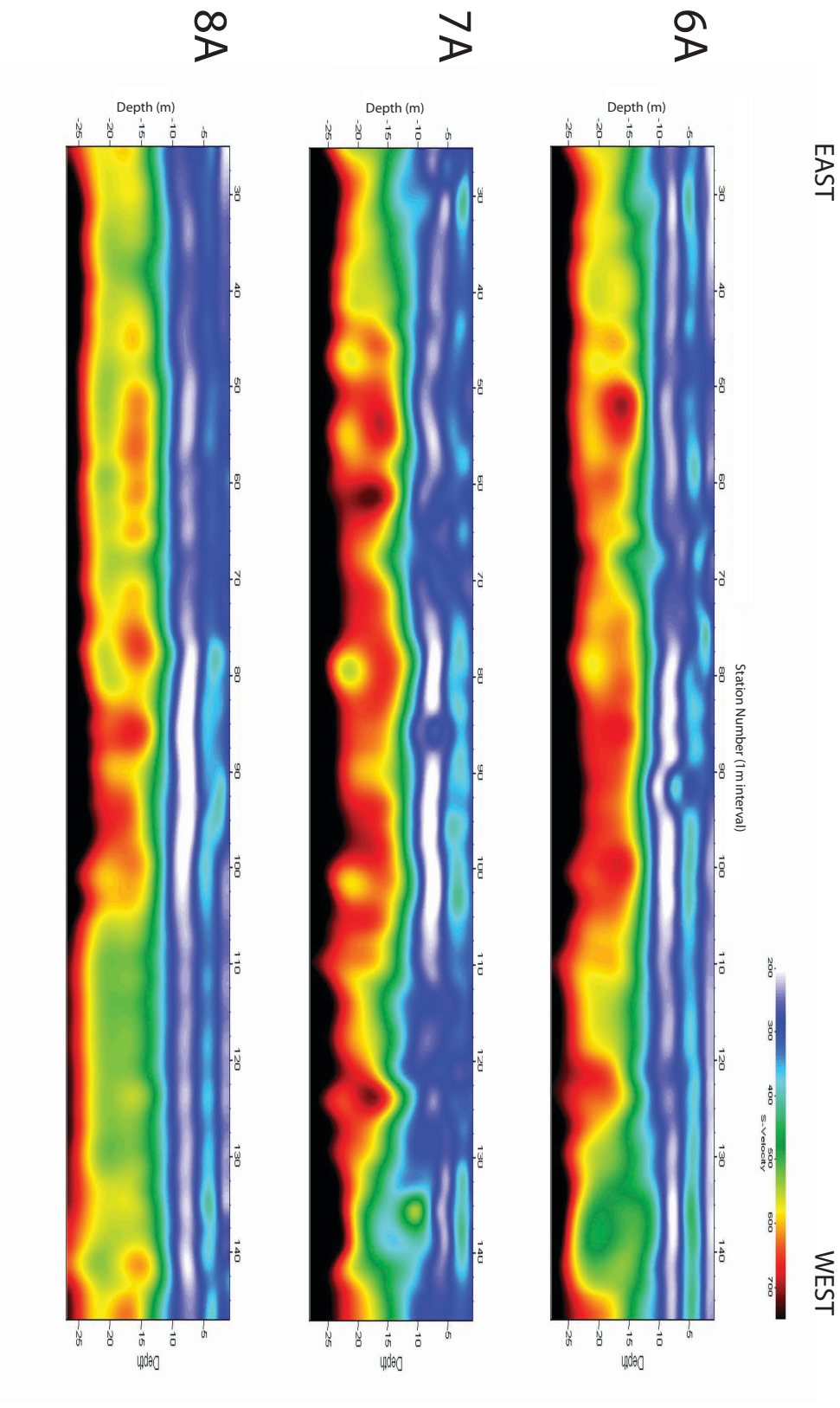


Figure 3.3: Alternative passive-source models for Line A using different processing parameters for dispersion curve picking (VE = 0.6); (6A) 8-50 Hz, 50 data points, smoothing: 3; (7A) 8-25 Hz, 30 data points, smoothing: 5; (8A) 8-50 Hz, 50 data points, smoothing: 5.

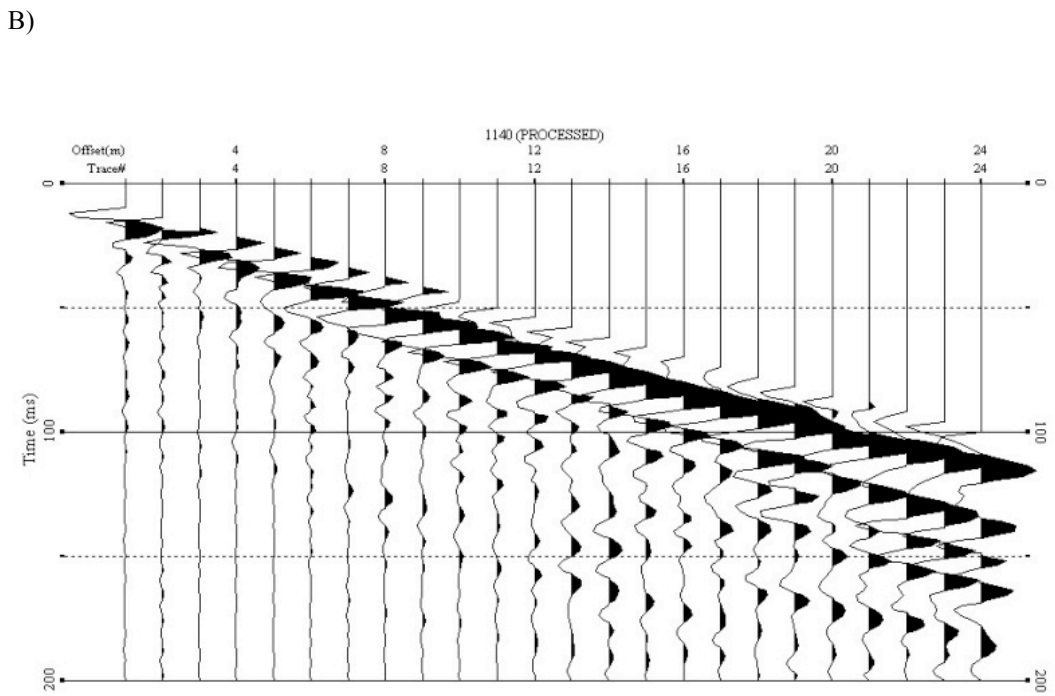
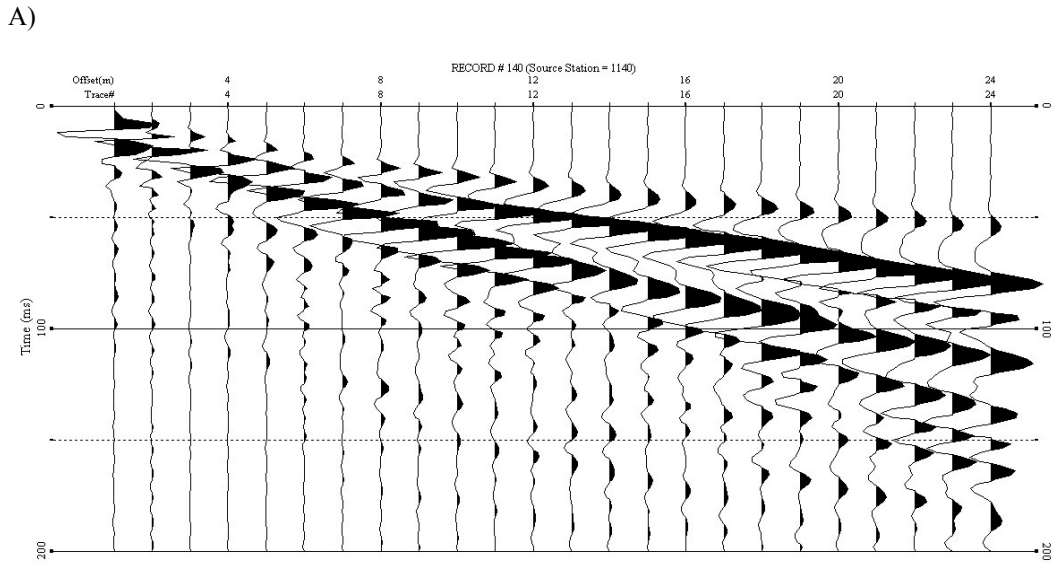


Figure 3.4: Shot gathers for STA 152 on Line A. A) No muting; B) Wedge mute.

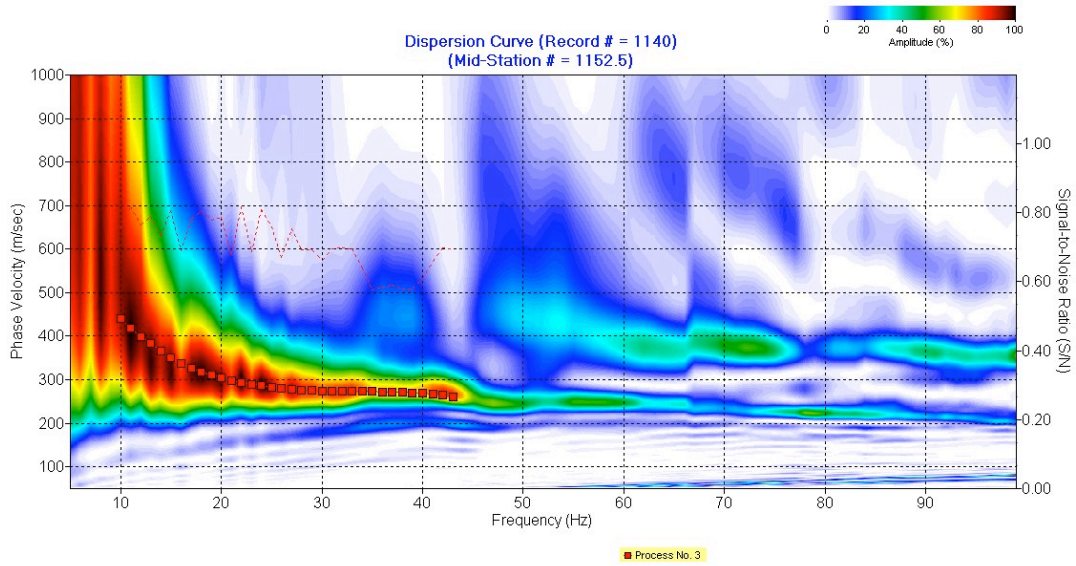


Figure 3.5: Active-source overtone image (amplitude contour plot) and dispersion curve picks (squares) for STA 152 on Model 1A without pre-processing (muting).

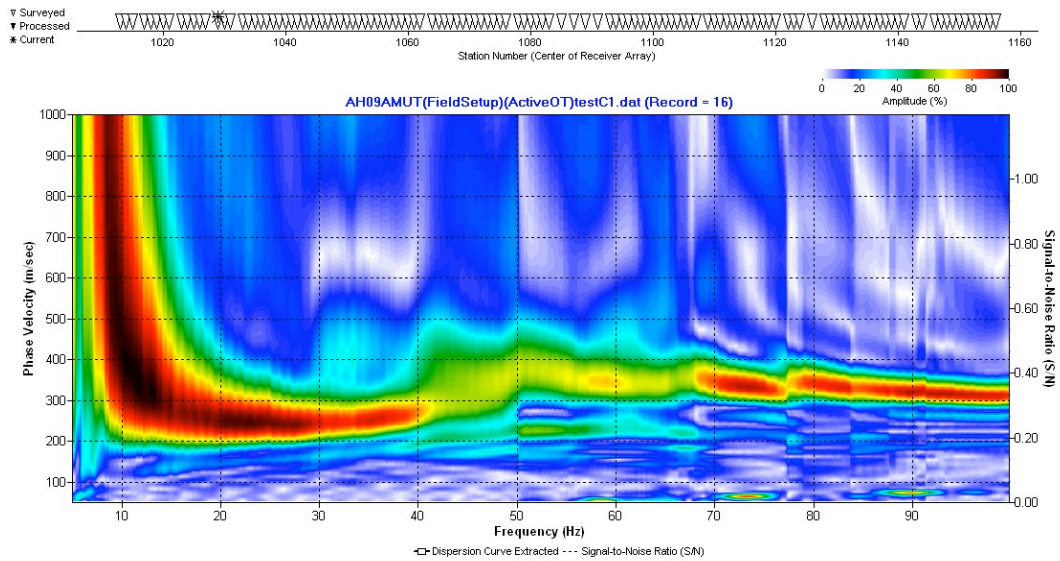


Figure 3.6: Active-source overtone image (amplitude contour plot) for STA 28 showing the fundamental mode and a higher-mode surface-wave merged together.

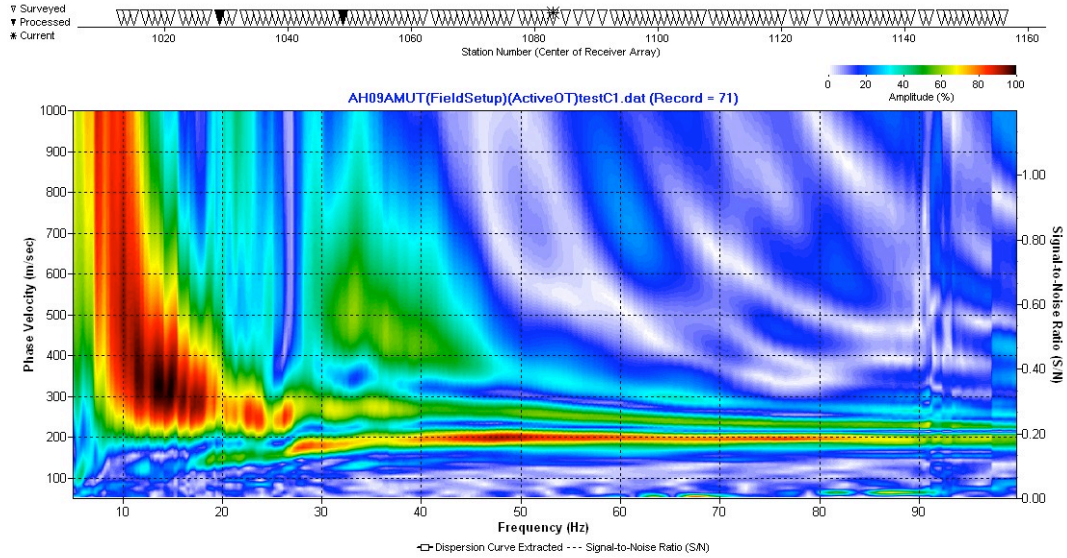


Figure 3.7: Active-source overtone image (amplitude contour plot) for STA 83 on Line A showing a branching effect at high frequencies (30-90 Hz).

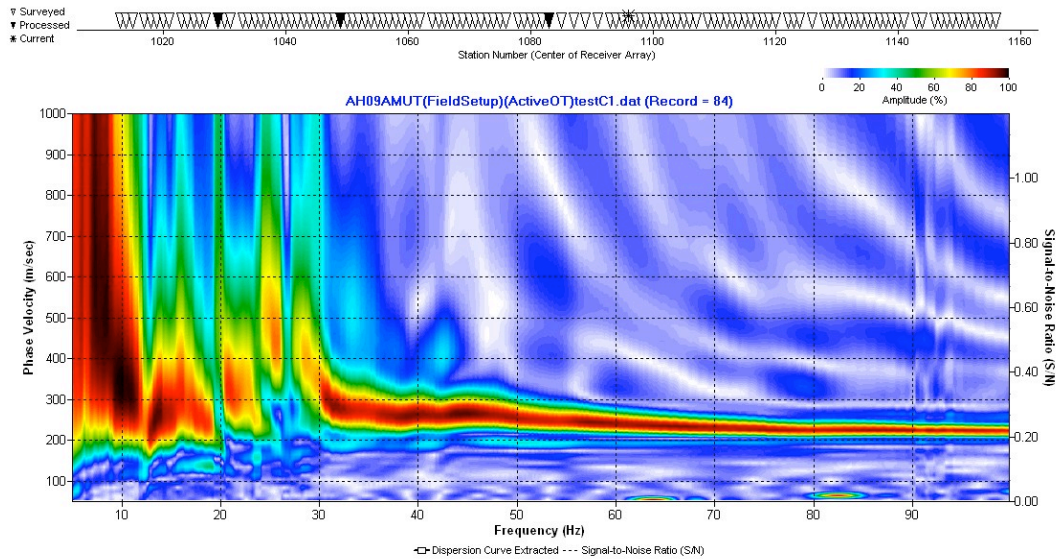
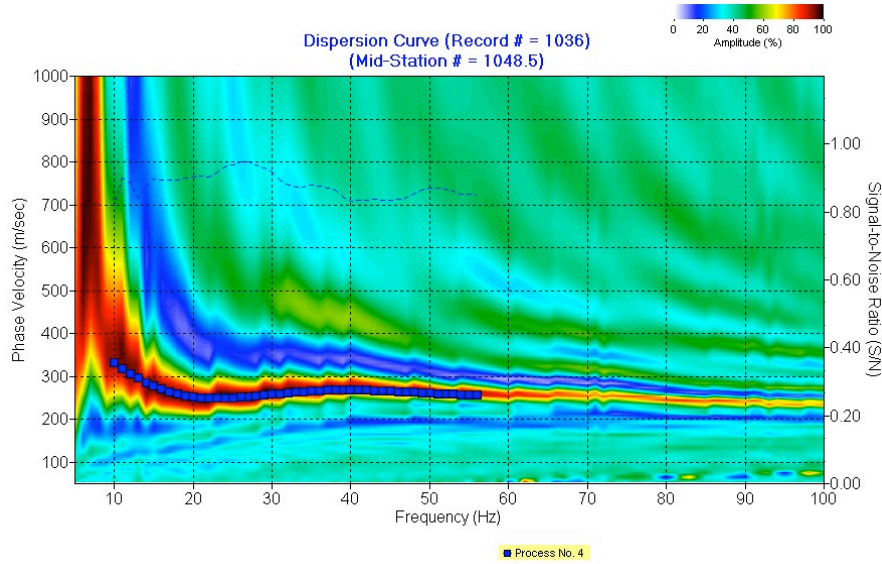


Figure 3.8: Active-source overtone image (amplitude contour plot) for STA 96 on Line A showing the disruption of the fundamental mode signal at low frequencies (10-30 Hz).

A)



B)

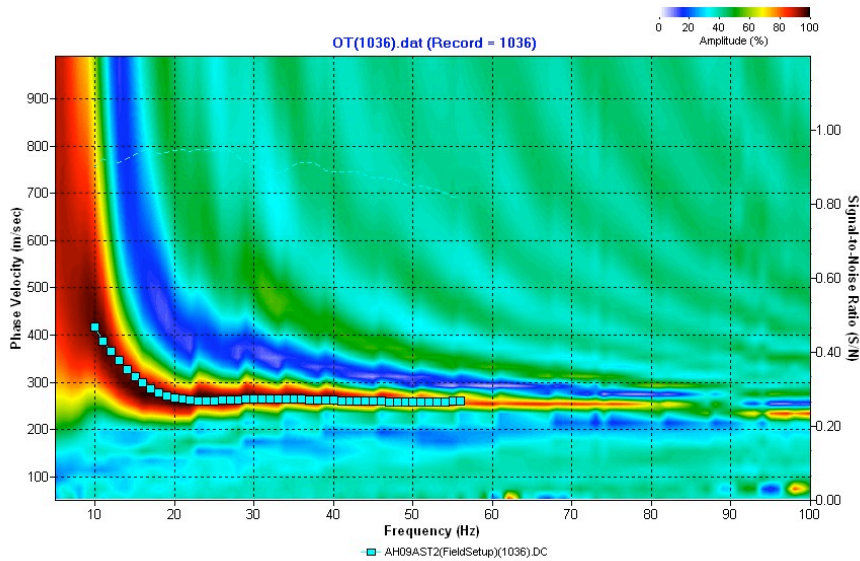
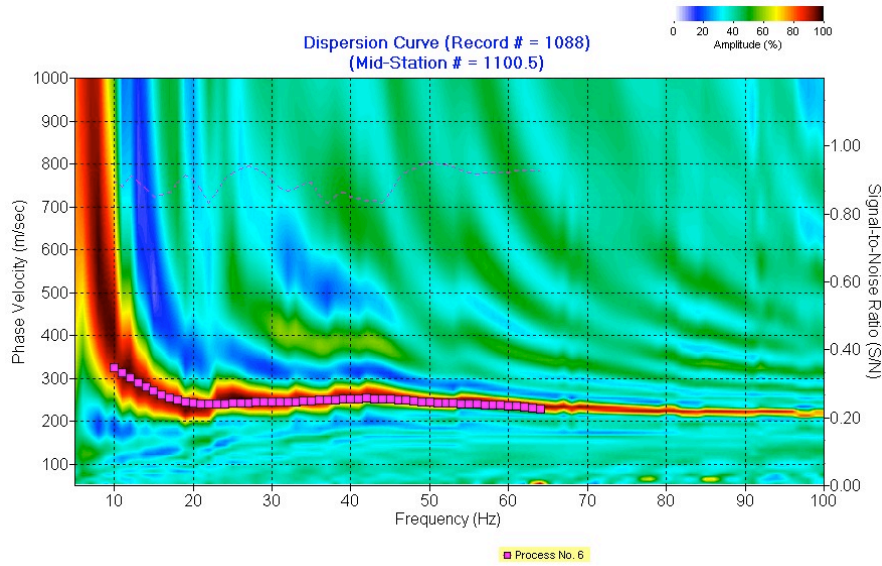


Figure 3.9: Active-source overtone images (amplitude contour plots) and dispersion curve picks (squares) for STA 48 Line A. A) Model 1A: no muting; B) Model 2A: Upwarping of the curve from 30-50 Hz is reduced after applying a wedge mute, and the increase in phase velocity at low frequencies (10-20 Hz) is an artifact of muting.

A)



B)

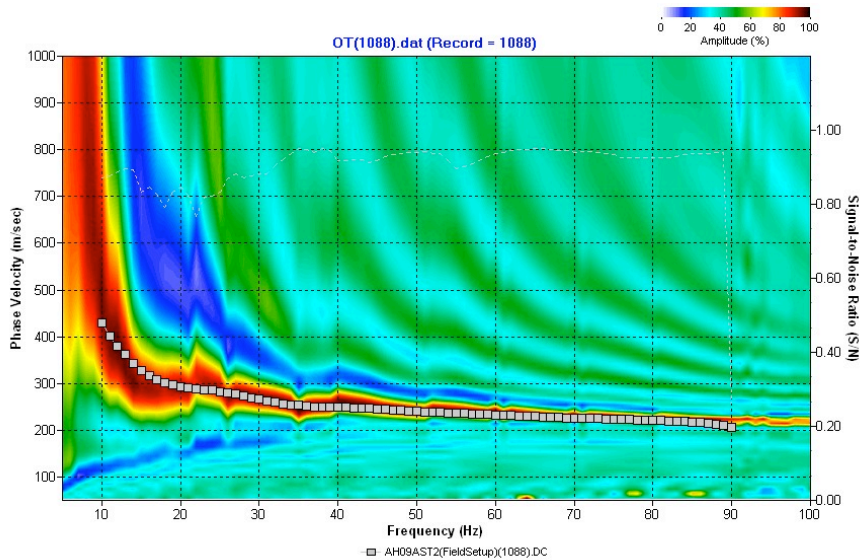
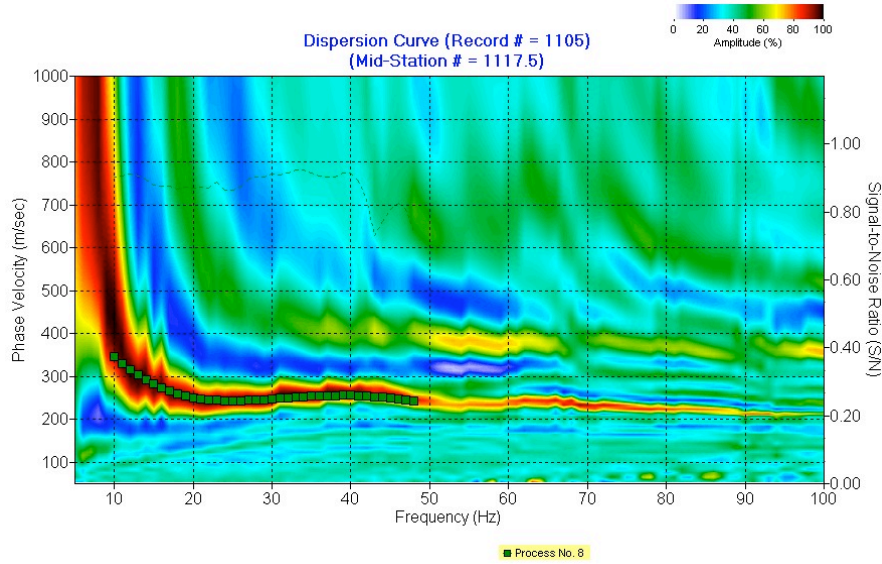


Figure 3.10: Active-source overtone images (amplitude contour plots) and dispersion curve picks (squares) for STA 100 for Line A. A) Model 1A: no muting; B) Model 2A: wedge mute. The increase in phase velocity at low frequencies (10-20 Hz) is an artifact of muting.

A)



B)

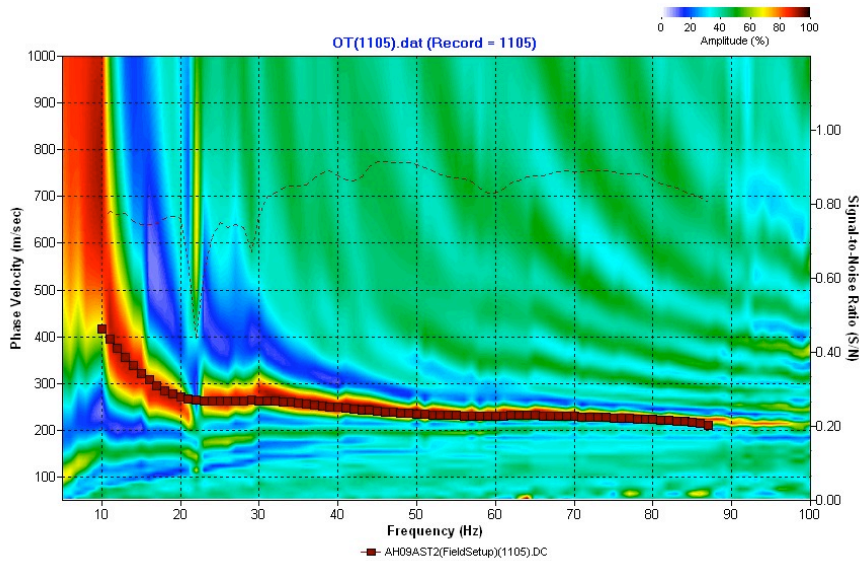
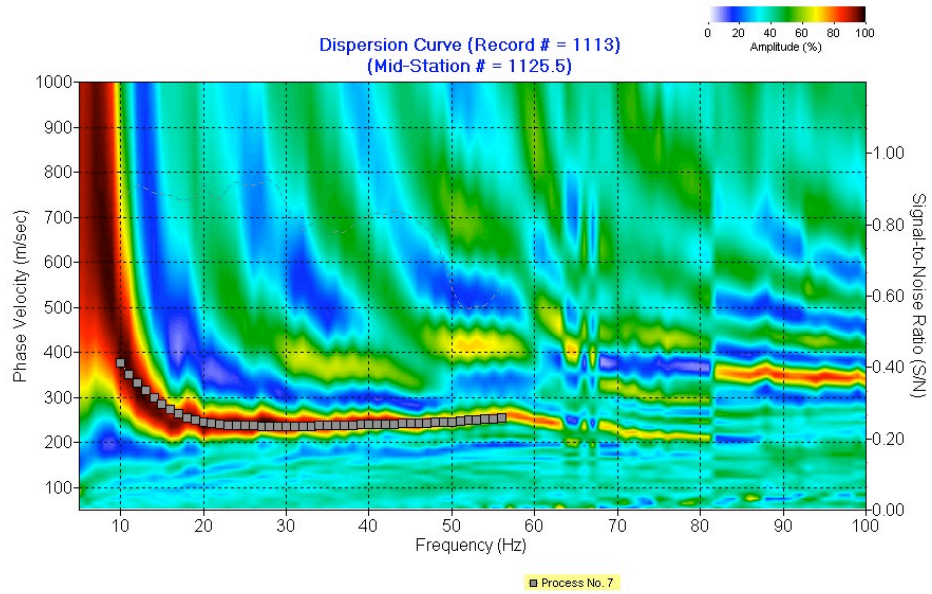


Figure 3.11: Active-source overtone images (amplitude contour plots) and dispersion curve picks (squares) for STA 117 on Line A. A) Model 1A: no muting; B) Model 2A: wedge mute. The higher-mode energy has been strongly attenuated. The higher phase velocity at low frequencies (10-20 Hz) is an artifact of muting.

A)



B)

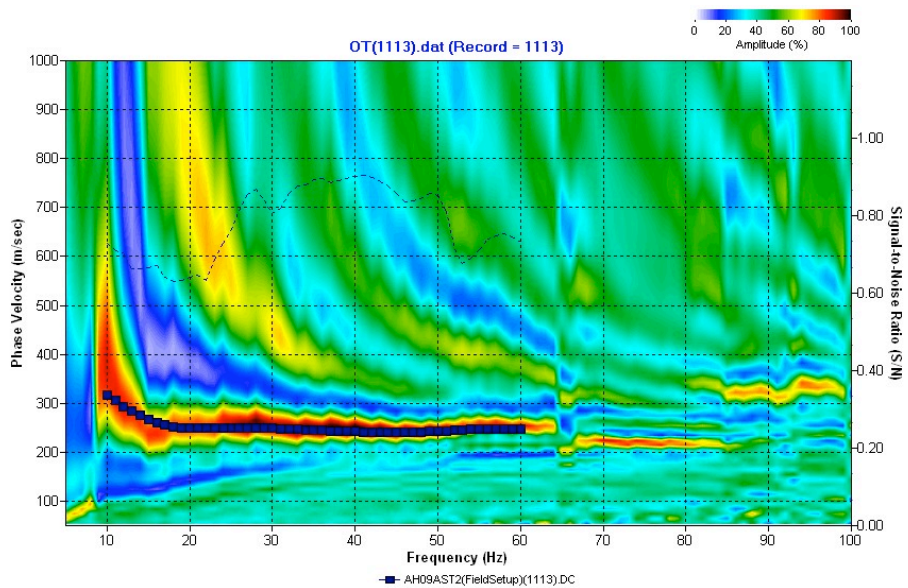
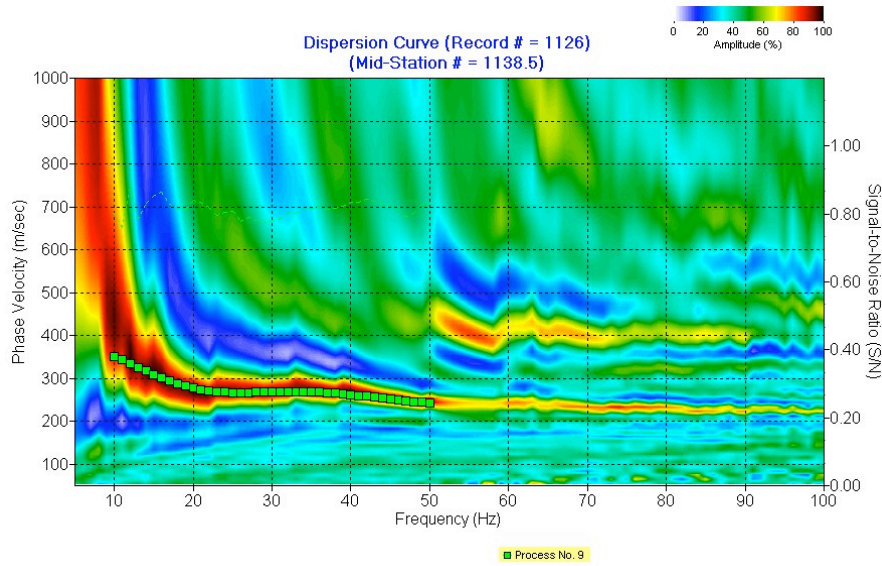


Figure 3.12: Active-source overtone image (amplitude contour plot) and dispersion curve picks (squares) for STA 125 on Line A. A) Model 1A: no muting; B) Model 2A: wedge mute. The phase velocity at 10 Hz is considerably lower (300 m/s) than the un-muted record. The quality of the image is degraded for frequencies less than 12 Hz.

A)



B)

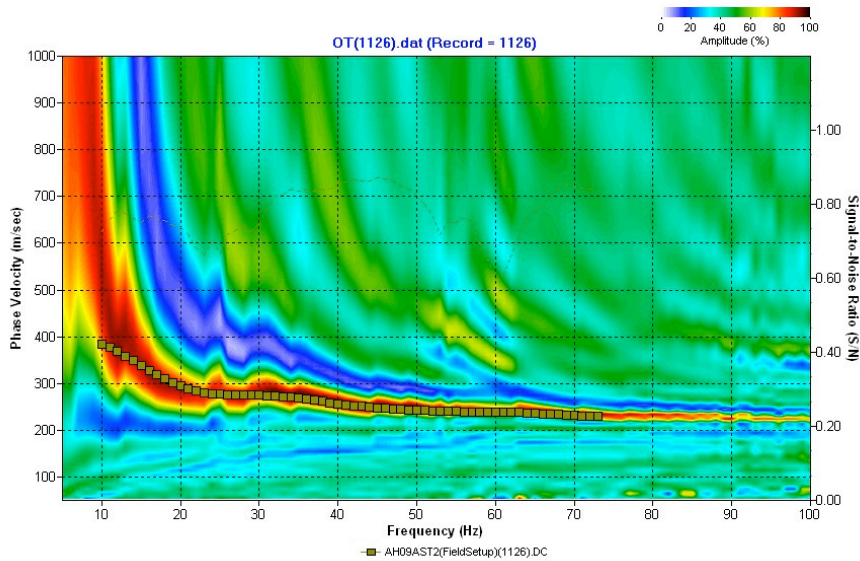
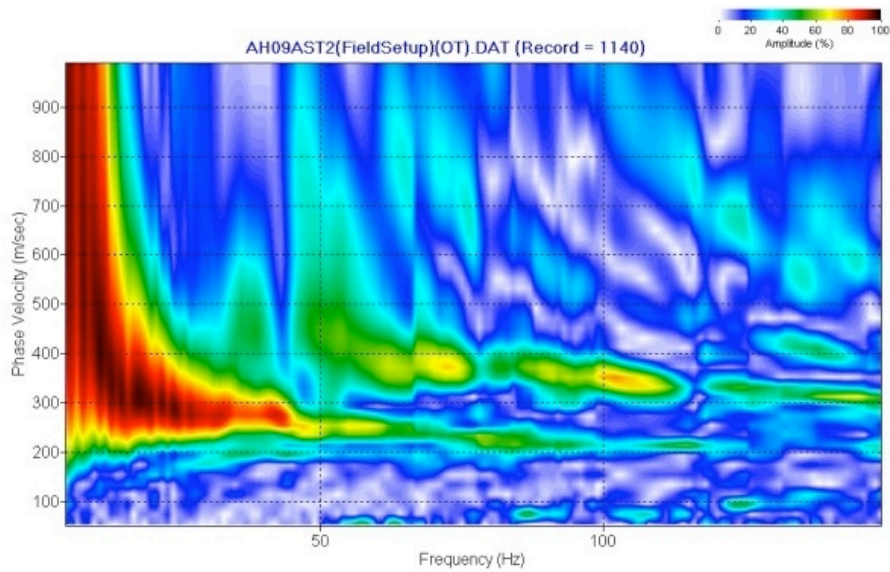


Figure 3.13: Active-source overtone images (amplitude contour plots) and dispersion curve picks (squares) for STA 138 on Line A. A) Model 1A: no muting; B) Model 2A: wedge mute. Higher-mode energy above 50 Hz is strongly attenuated. Again, the increase in phase velocity at the lowest frequencies is an artifact due to muting the early part of the fundamental mode.

A)



B)

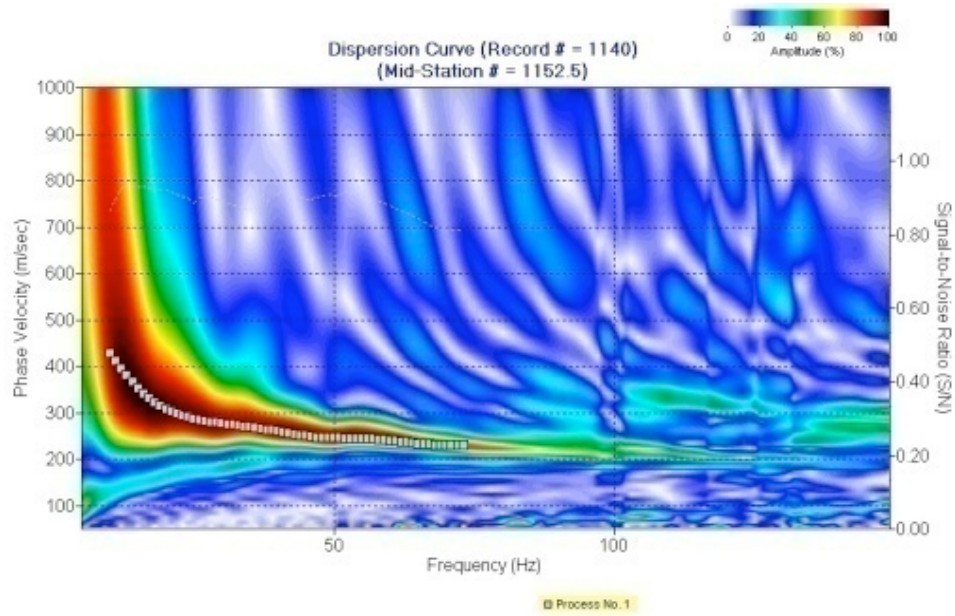


Figure 3.14: Active-source overtone images (amplitude contour plot) and dispersion curve picks (squares) for STA 152 on Line A. A) Model 1A: no muting; B) Model 2A: wedge mute. The higher-mode surface wave energy is attenuated, and resolution of the fundamental mode at high frequencies (50-75 Hz) is improved.

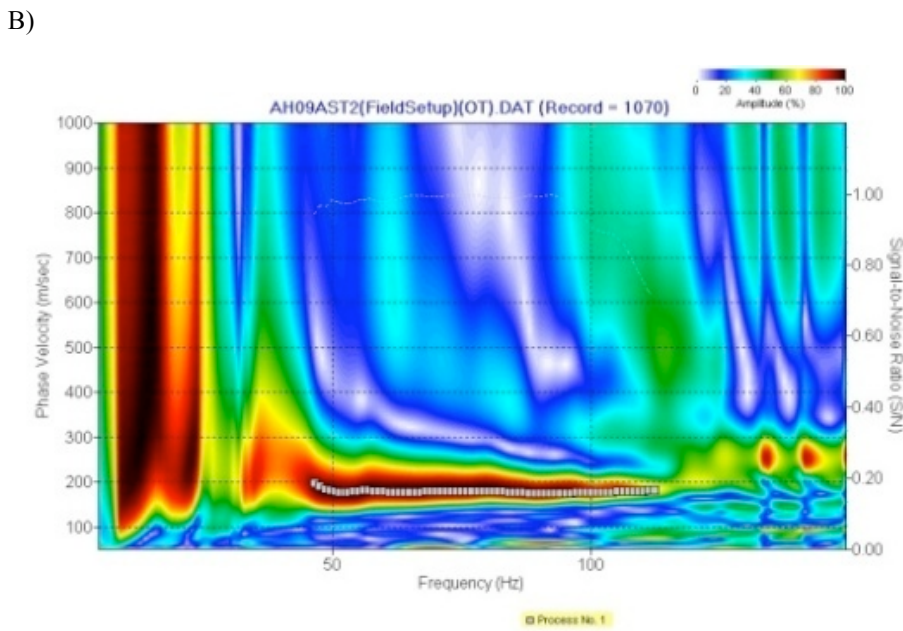
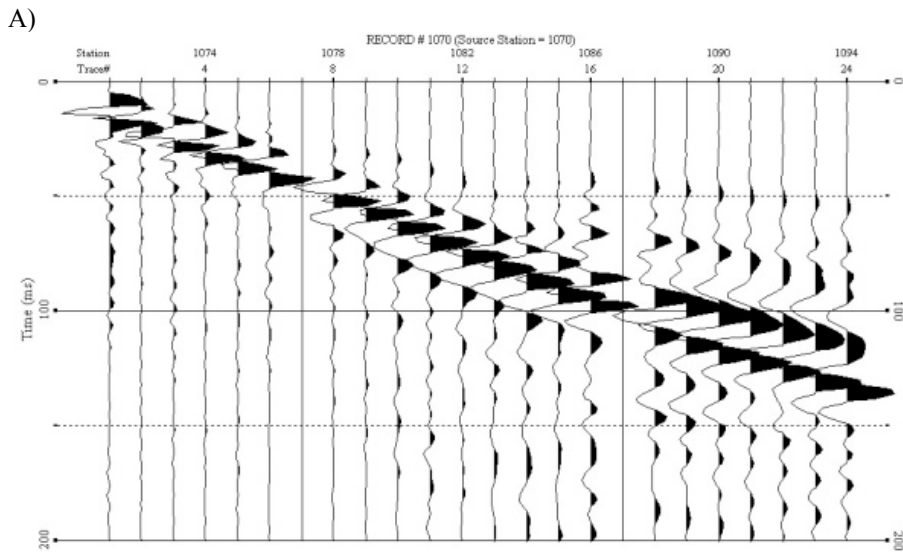
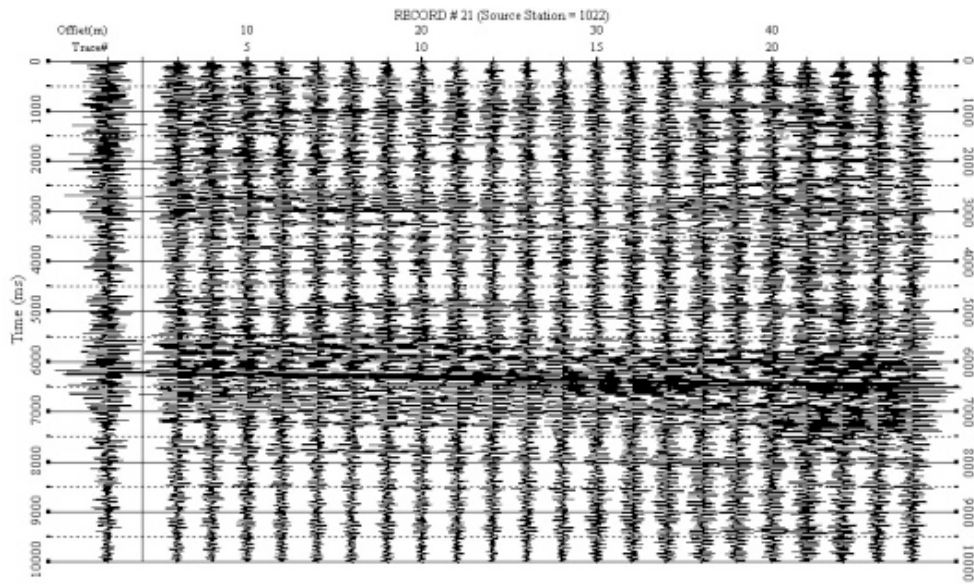


Figure 3.15: A) Shot gather for STA 82 on Line A. There is a distinct change in the slope of the surface wave between STA 78-87 indicating lower apparent velocity in this section. (B) Active-source overtone record (amplitude contour plot) and dispersion curve picks (squares) for traces 11-17 on the shot gather for STA 82. Note the distortion of low frequencies due to the small number of traces used in the overtone analysis.

A)



B)

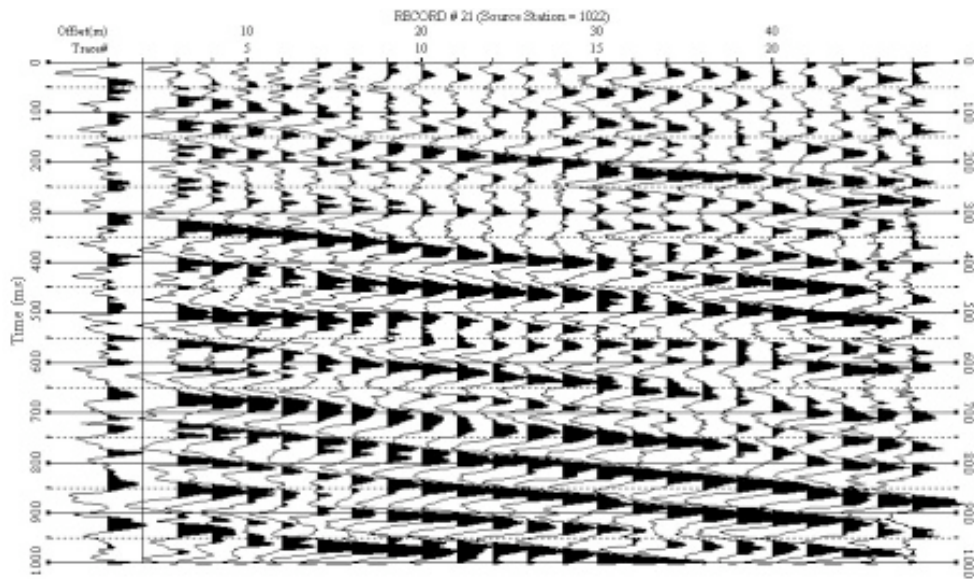


Figure 3.16: (A) Passive-source shot gather for STA 65 on Line A. (B) Passive-source shot gather for STA 65 on Line A showing only the first 1000 ms of the record.

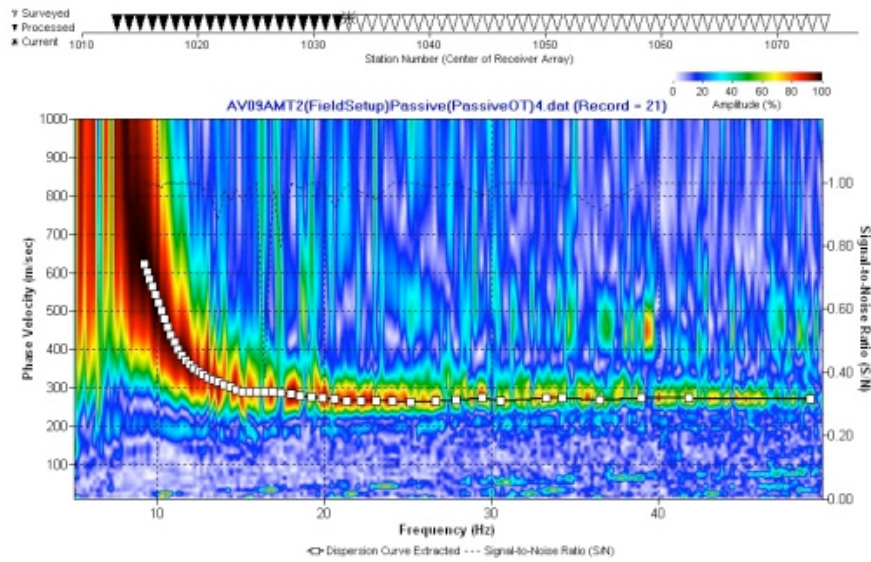


Figure 3.17: Passive-source overtone image (amplitude contour plot) and dispersion curve picks (squares) for STA 65 (Model 6A).

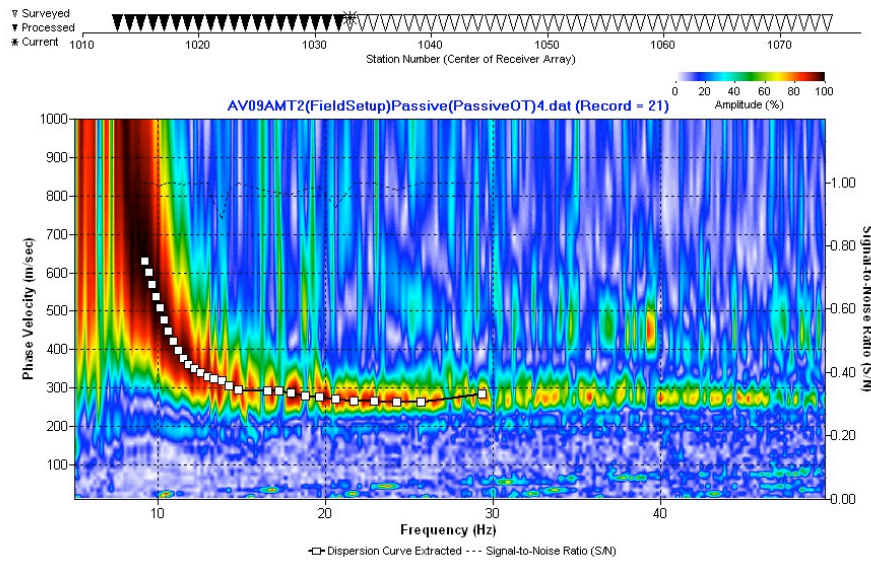


Figure 3.18: Passive-source overtone image (amplitude contour plot) and dispersion curve picks (squares) for STA 65 (Model 7A).

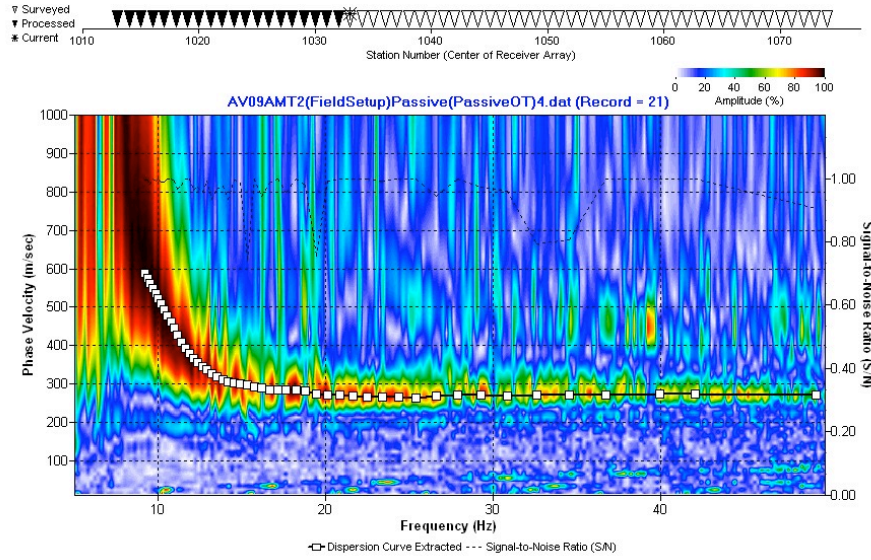


Figure 3.19: Passive-source overtone image (amplitude contour plot) and dispersion curve picks (squares) for STA 65 (Model 8A).

CHAPTER 4

SHEAR-WAVE VELOCITY MODELS: LINES Y AND Z

Lines Y and Z are oriented perpendicular to Lines A-G to “tie” those lines and provide some constraints on the 3-D structure. Differences in shear-wave velocity at the intersection point of two perpendicular lines are expected due to the averaging effect across the geophone spread. Despite the effects of smearing, it seems likely that the location and extent of prominent low-velocity zones and suspected subsidence features can be well constrained with surface wave data collected along a grid. The intersection points of the seismic lines are shown in Table 4.1. The 1-D shear-wave velocity models for the intersection points are shown in Appendix B.

Line Y

The “conservative” active and passive-source models for Line Y are shown in Figure 4.1. The interpreted depth to bedrock of 9-12 meters (350 m/s transition) is consistent with borehole information as well as models for Lines A-G. The modeling results from the two independent data sets suggest that low-velocity zones at depth are related to anomalous zones in the upper 12 meters of the subsurface.

Line Z

The “conservative” active and passive-source models for Line Z are shown in Figure 4.2. Once again, interpreted depth to bedrock of 8-10 meters is consistent with borehole information and previous models. A low-velocity zone is evident at the intersection of Line A and Z (STA A83 and Z55). The LVZ (< 200 m/s shear-wave

velocities) at a depth of 5m between STA 45-60 (Figure 4.2) on the active-source profile for Line Z directly correlates with the LVZ on Line A between STA 79-87 (Figure 3.2).

The shot gathers from Line Z shown in Figure 4.3 can be used to constrain the dimensions of the LVZ. The change in slope on the shot gather from STA 54 to 65 spans approximately 11 meters. For the same feature on Line A, the change in slope spans approximately 8 meters from STA 79 to 87 (Figure 4.4). Therefore, the feature appears to have a slightly elliptical shape (asymmetry ratio: 1.375) with the long axis oriented north-south. In a study in Albany, GA, Hyatt and Jacobs (1996) demonstrated that the majority of sinkholes were nearly circular with 75% having asymmetry ratios less than 1.3, and the dominant azimuthal orientation for elongate sinkholes is 355 degrees. Brook and Allison (1983) also found a dominant long axis azimuth of 0-10 degrees in Dougherty County. The asymmetry ratio and azimuth of elongation for the interpreted sinkhole correlates well with morphometric data from the Albany area.

Relatively low shear-wave velocity at the intersection of Lines A and Z supports the conclusion that this area is a potential subsidence feature. The trend of the feature indicates that formation may be controlled by a north-south oriented fracture, which is consistent with the sinkhole formation at the site and documented fracture patterns (Brook and Allison, 1983).

Comparison of models with topographic profiles

Figures 4.6 and 4.7 show the active-source shear-wave velocity models compared with topography for Lines Y and Z, respectively. In general, the entire field area can be characterized as a flat landscape with subtle topographic depressions. However, there is approximately 2 meters of topographic relief along Line Y. The topographic high extends

from STA 150 to 225, but there are no obvious correlations between the active-source model and topographic profile. It is important to note that the natural topography has been altered by construction of well #44, so correlations between velocity anomalies and topographic features can be difficult.

Table 4.1: Intersection points for seismic lines

<u>Intersection Points for Seismic Lines</u>	
<u>Line Y</u>	<u>Line Z</u>
Y15/C62.5	Z15/C82.5
Y35/B63	Z35.5/B83
Y55/A63	Z55.5/A83
Y74/D63	Z74/D83
Y95/E63	Z95/E83
Y114/F63	Z115/F83
Y134/G63	Z134/G83

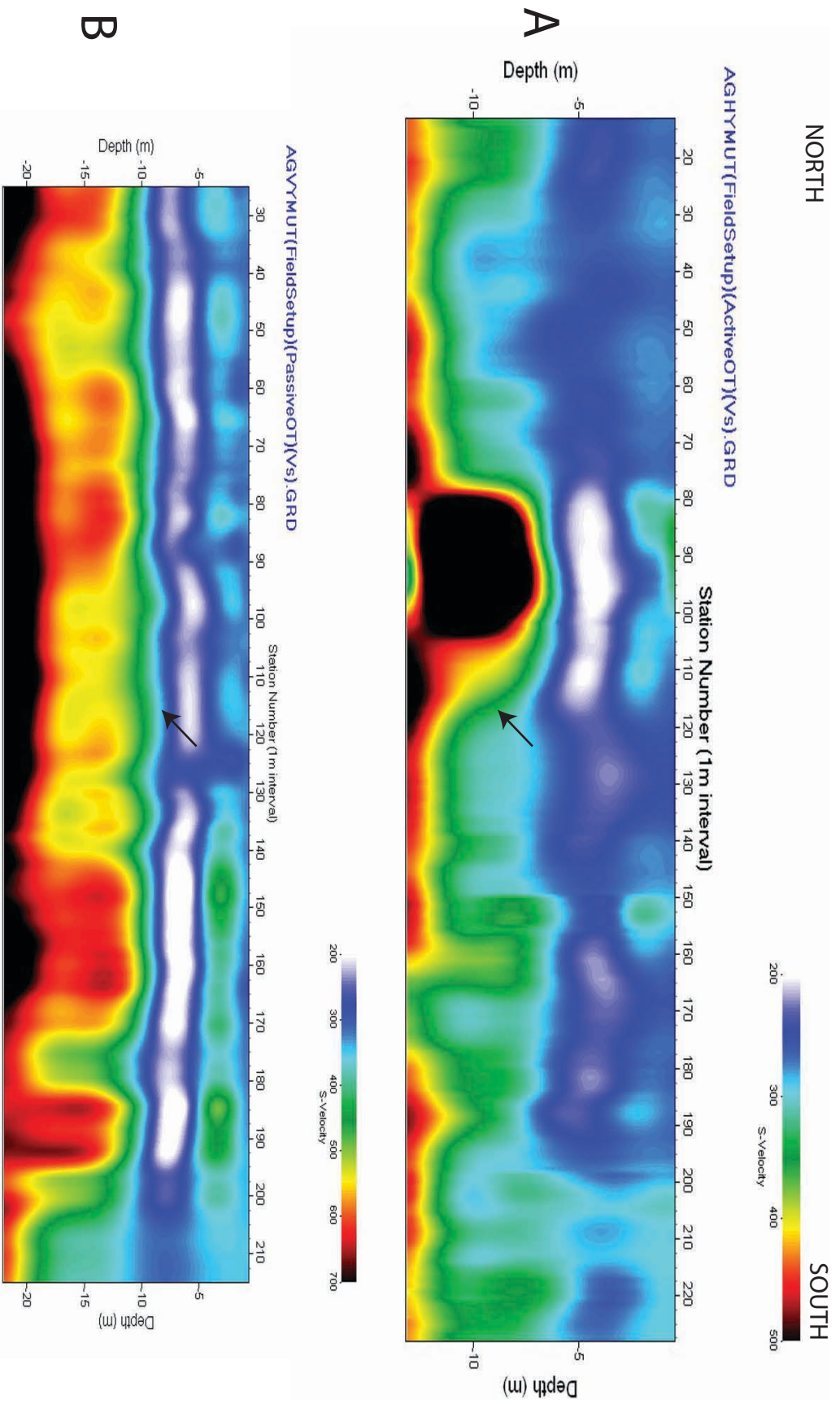


Figure 4.1: (A) Active-source (VE = 3.5) and (B) passive-source (VE = 2.2) models for Line Y. The arrow indicates the 350 m/s contour.

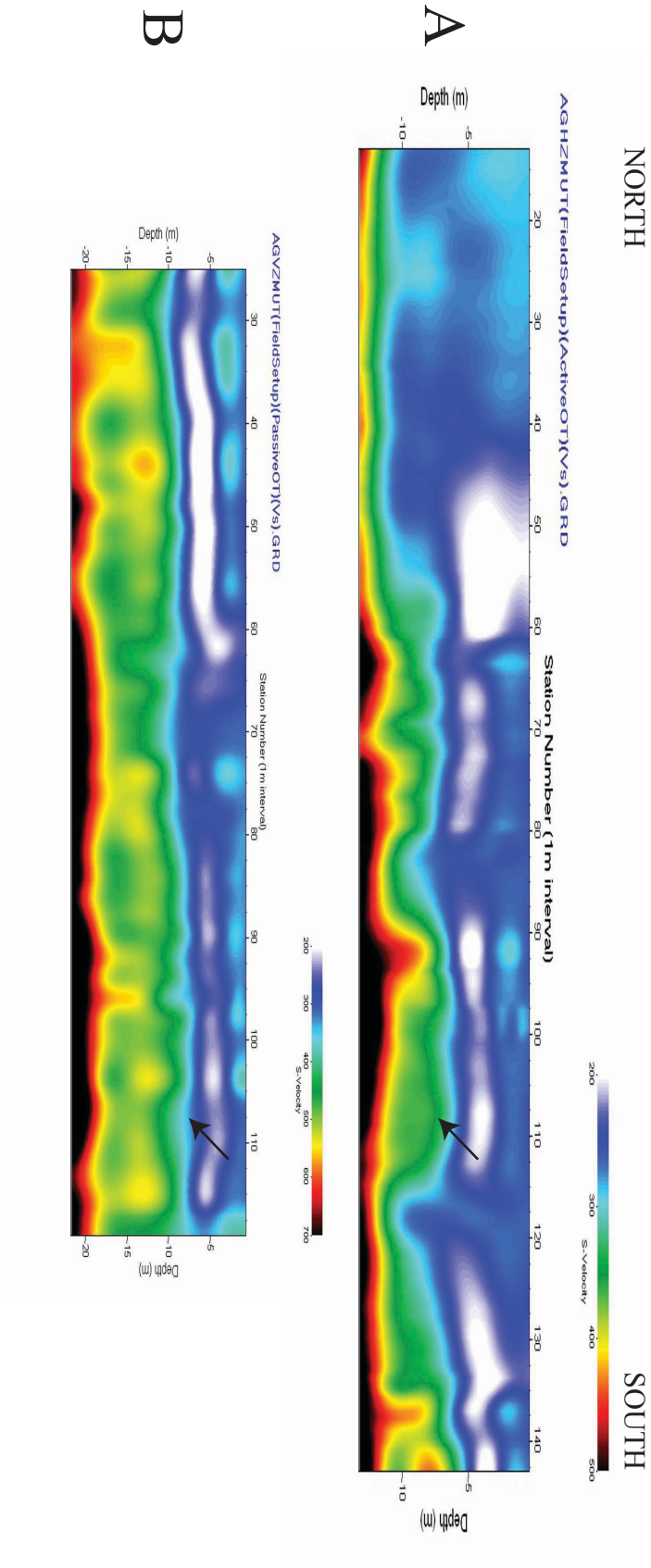


Figure 4.2: (A) Active-source ($VE = 1.3$) and (B) passive-source ($VE = 0.78$) models for Line Z. The arrow indicates the 350 m/s contour.

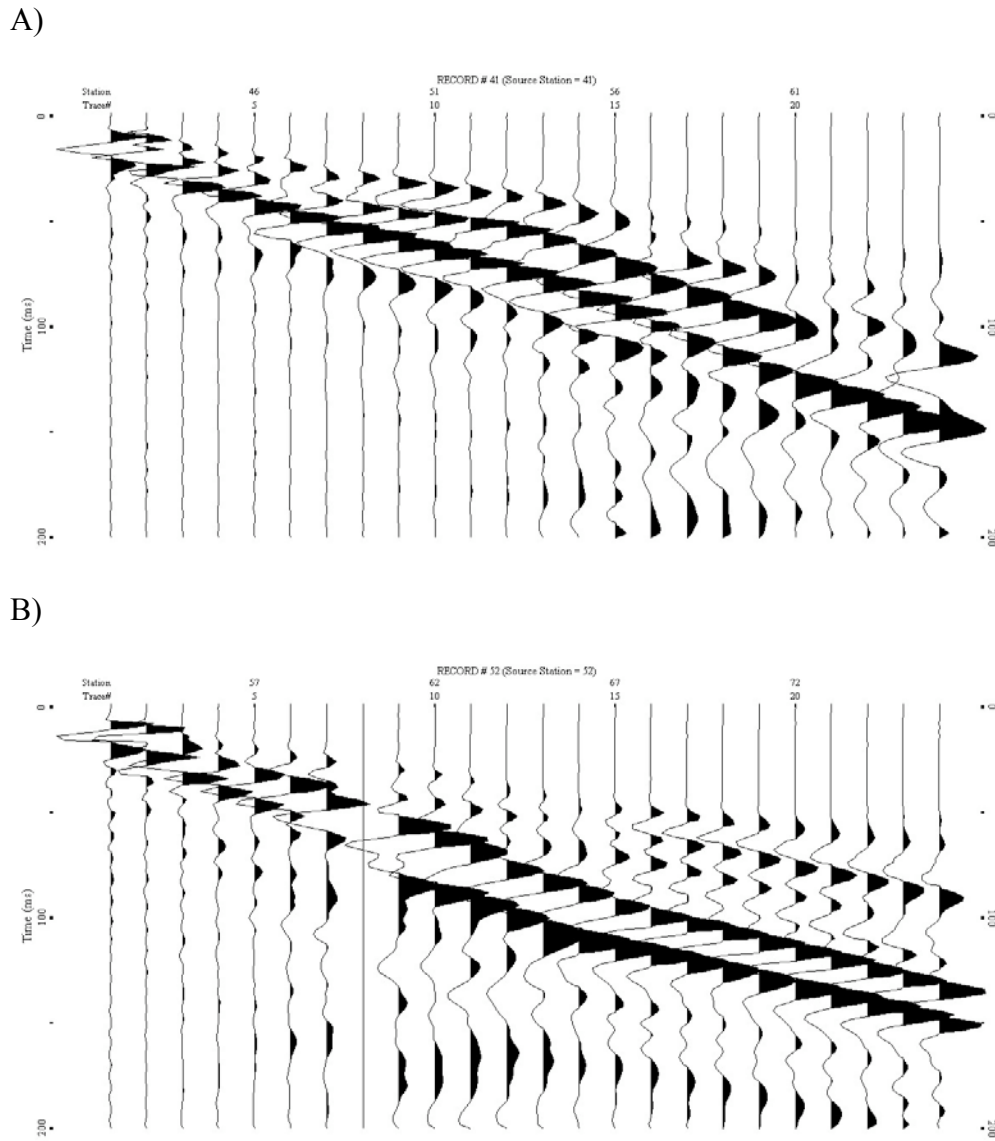


Figure 4.3: Shot gathers across the LVZ on Line Z; (A) shot gather for STA 53; (B) shot gather for STA 64. The change in slope of the surface-wave indicates that the LVZ is located between STA 54 and 65.

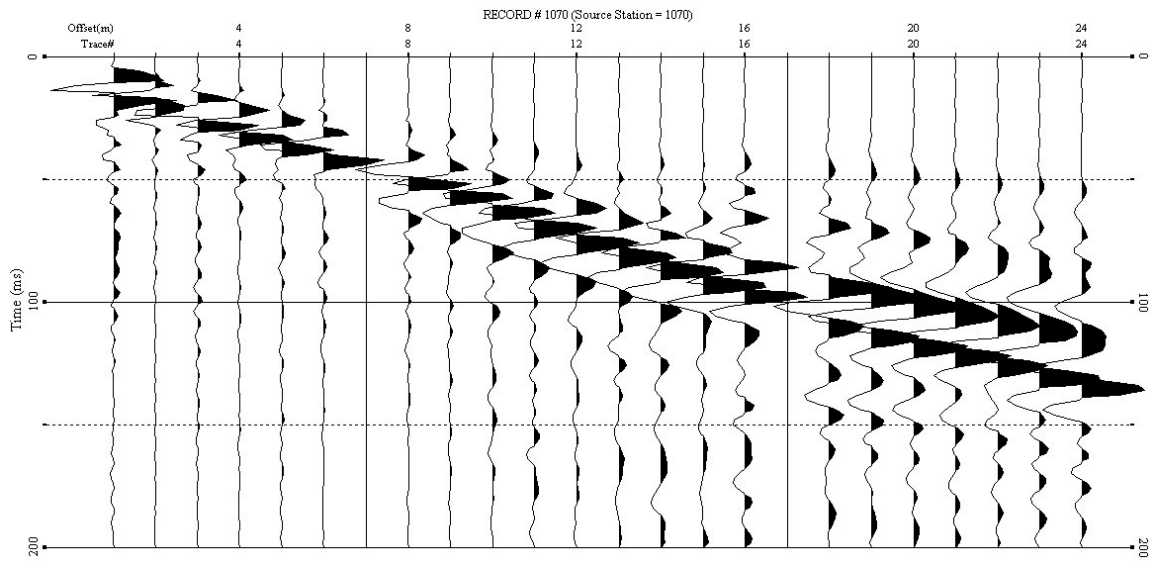
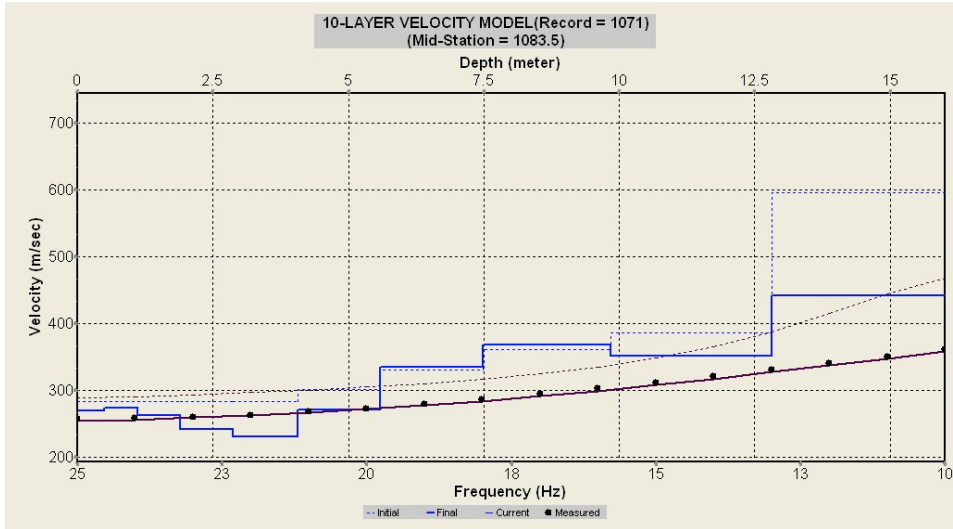


Figure 4.4: Shot gather for STA 82 on Line A. The LVZ spans approximately 9 meters from STA 78 to 87.

A)



B)

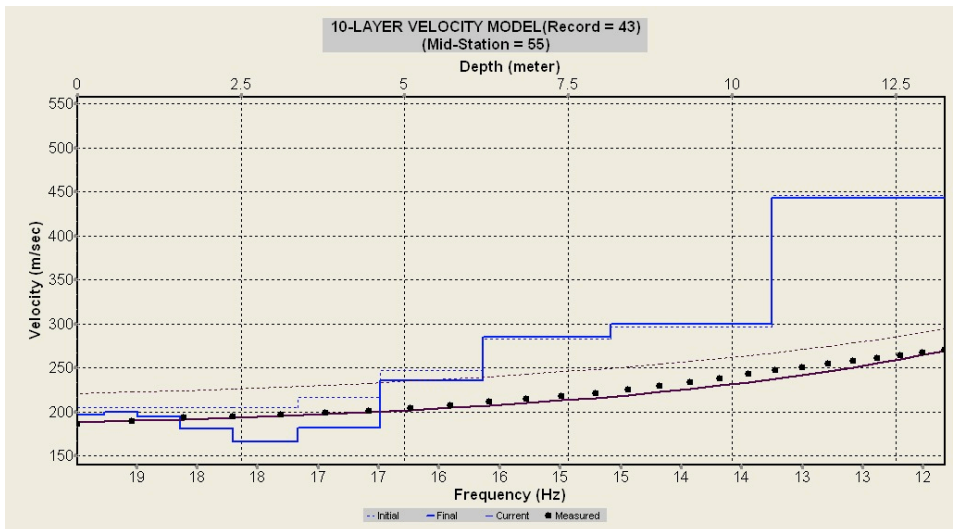
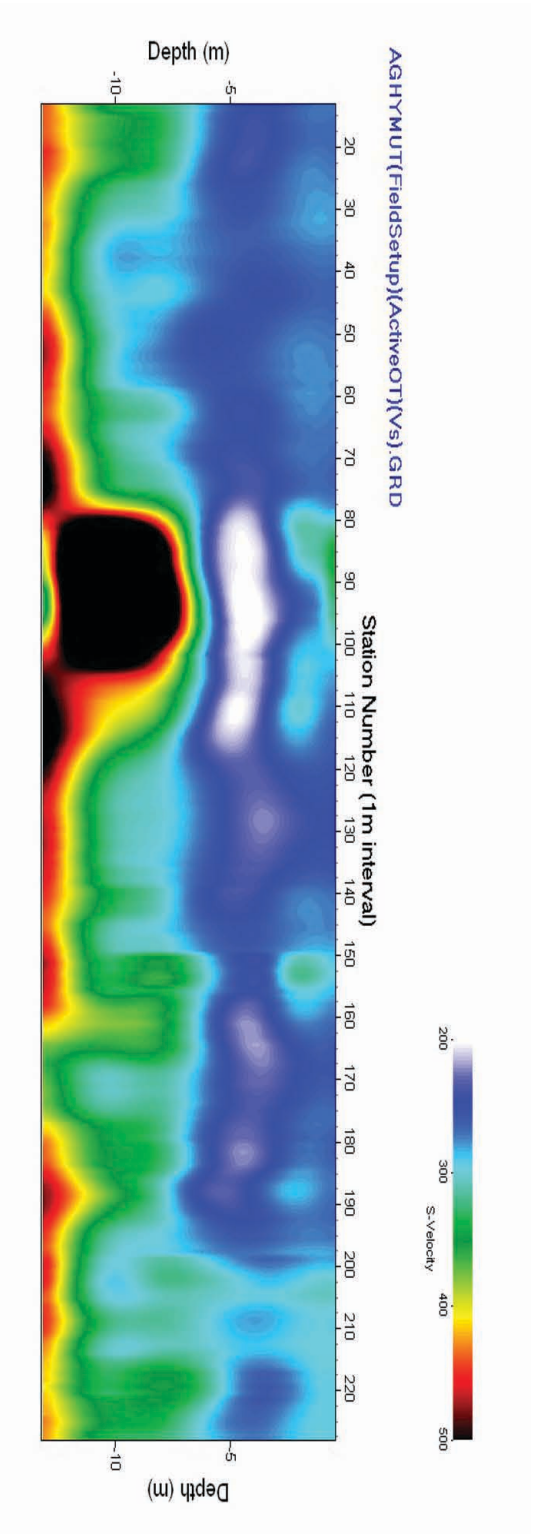


Figure 4.5: 1-D shear-wave velocity models for the intersection of Line A and Z; (A) STA 83 on Line A, (B) STA 55 on Line Z.



Line Y: Elevation Relative to Well 44 slab

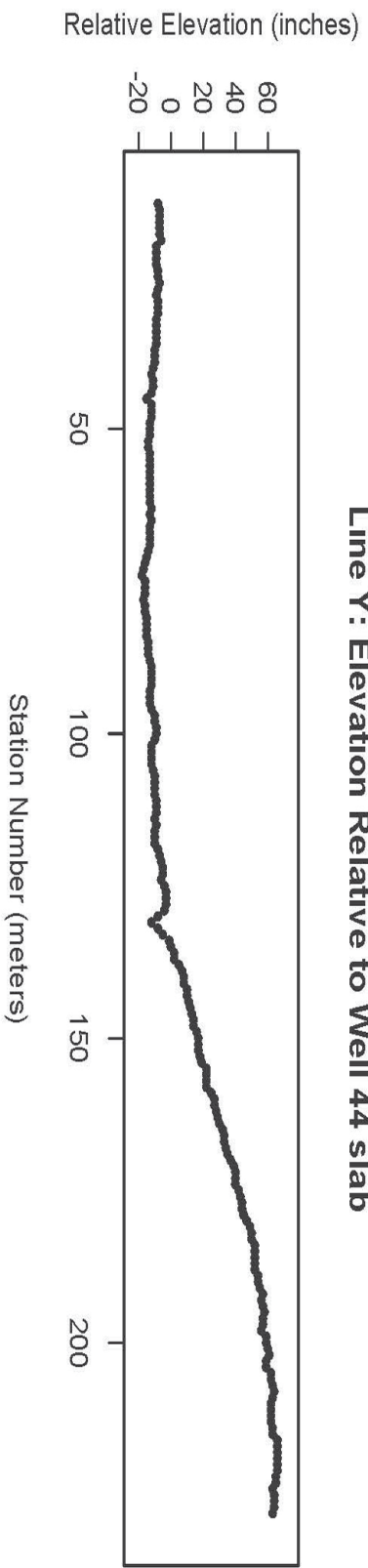


Figure 4.6: Active-source model (VE = 3.5) and topographic profile (VE = 10.5) for Line Y.

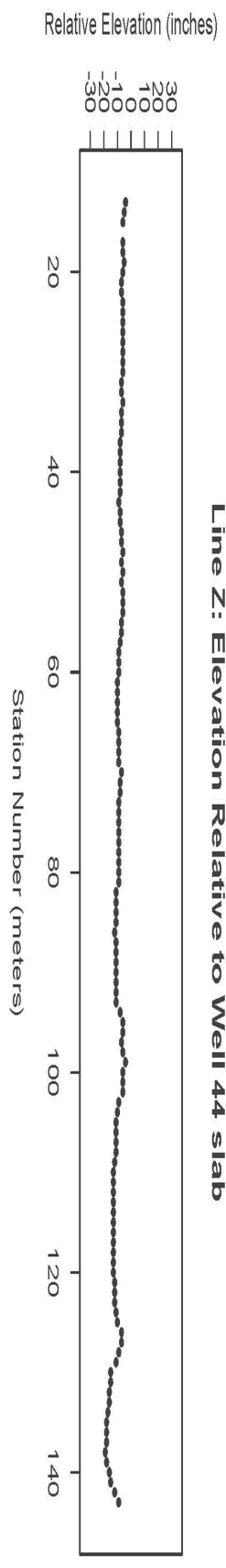
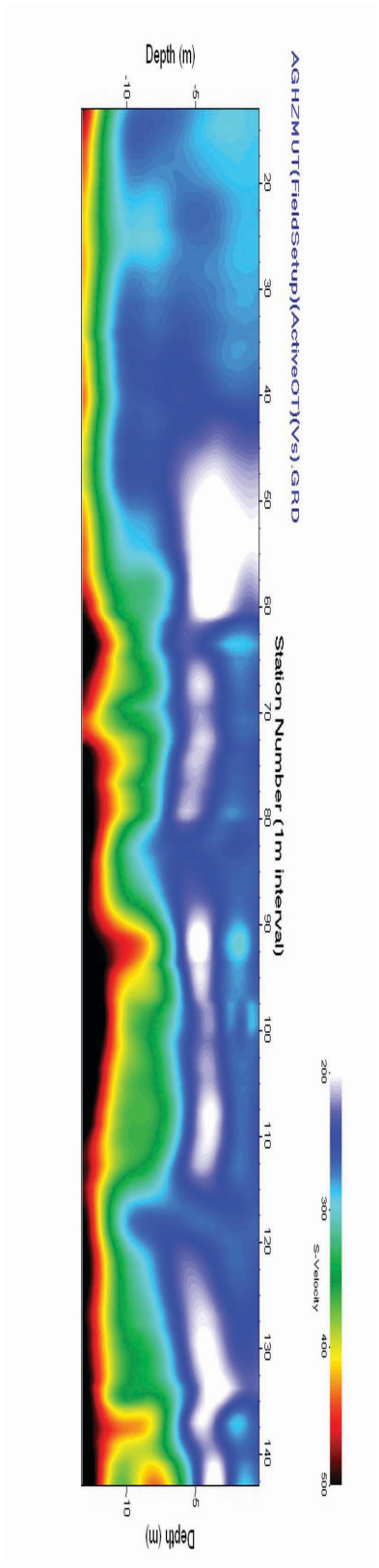


Figure 4.7: Active-source model (VE = 1.3) and topographic profile (VE = 5.3) for Line Z.

CHAPTER 5

HALF-SPREAD ANALYSIS: LINES A-G and Y-Z

The middle twelve traces (7-18) for each active-source shot gather were processed to improve lateral resolution within the upper 4 meters of the subsurface. As mentioned before, lateral resolution is improved at the expense of depth penetration. The half-spread models are presented in Figures 5.1-5.9 with the full-spread (23 meter aperture) active-source models shown for comparison.

Contamination of the fundamental mode by higher-mode surface waves is still a primary concern in the half-spread analysis. The dispersion curves shown in Figure 2.3 indicate that phase velocities for given frequencies higher than 30 Hz are likely affected by higher mode surface wave energy. Therefore, muting was performed on all shot gathers prior to generating the half-spread models. The intent was to analyze relatively high frequencies, so a conservative frequency range of approximately 35-90 Hz was used for dispersion curve picking to avoid the distorted part of the overtone record at lower frequencies. Artifacts resulting from muting are still possible, so interpretations of the half-spread models must ultimately be based upon qualitative assessments of the amplitude contour plots and dispersion curves. Nonetheless, several features in the half-spread models correlate nicely with the original models, so confidence in the technique is still relatively high.

The most striking feature on the half-spread models is located at the intersection of Lines A (STA A83; Figure 5.1) and Z (STA Z55; Figure 5.9). A low-velocity zone is

apparent at STA 75-90 on Line A and STA 50-60 on Line Z; on both lines, the zone widens with depth. The seismic signature of the of the anomaly spans 10-15 meters, and the feature is interpreted to be a potential subsidence feature or void.

The LVZ on Line E illustrates the effect of smearing across the geophone spread. On the full-spread model (Figure 5.5A), the LVZ extends from STA 53 to 73 in the upper 5 meters of the model. The half-spread model (Figure 5.5B) indicates a more localized LVZ from STA 65 to 75. These results suggest that half-spread analysis can be used to locate anomalous zones in the upper 3-4 meters of the sub-surface. Therefore, integrated analysis of models for different depth ranges can be used to constrain interpretations of potential subsidence features.

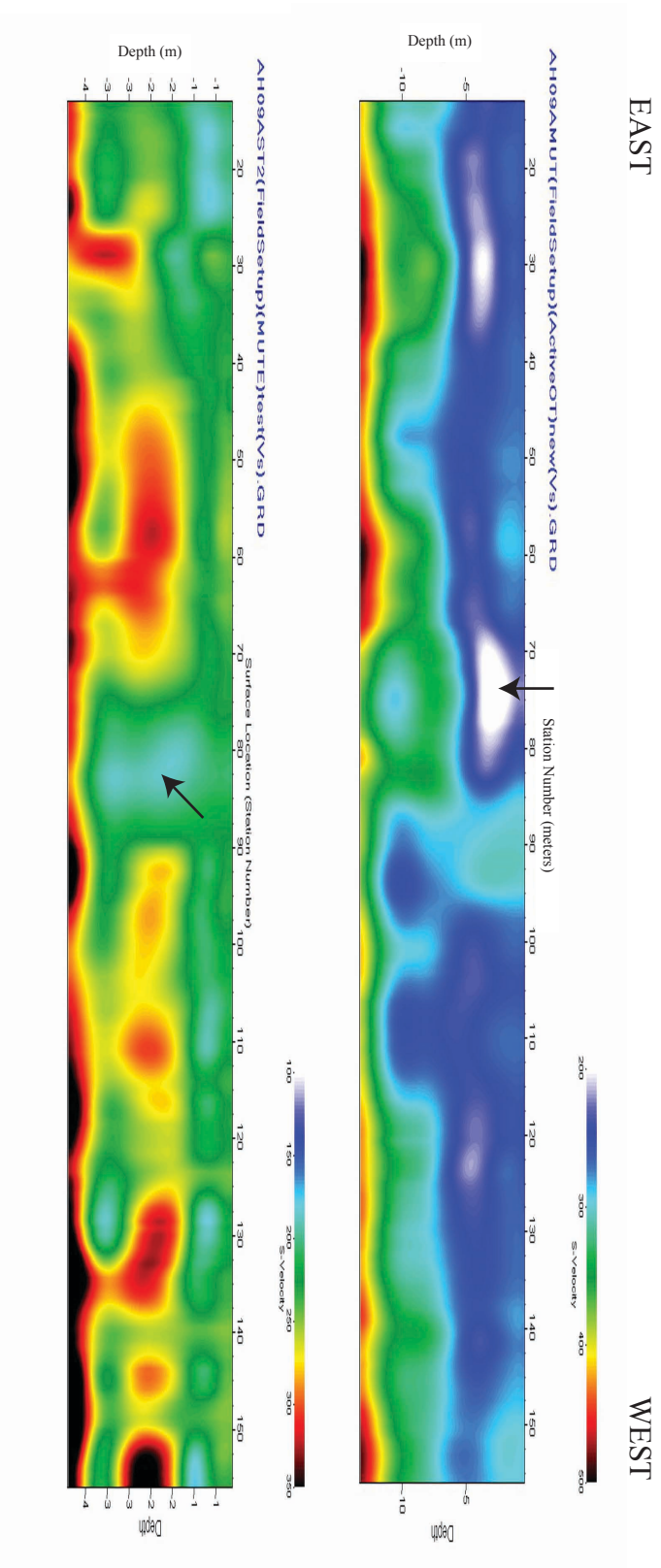


Figure 5.1: Active-source models for Line A; (A) full spread (VE = 1.3), (B) half spread (VE = 4.5). Arrow indicates low-velocity anomaly.

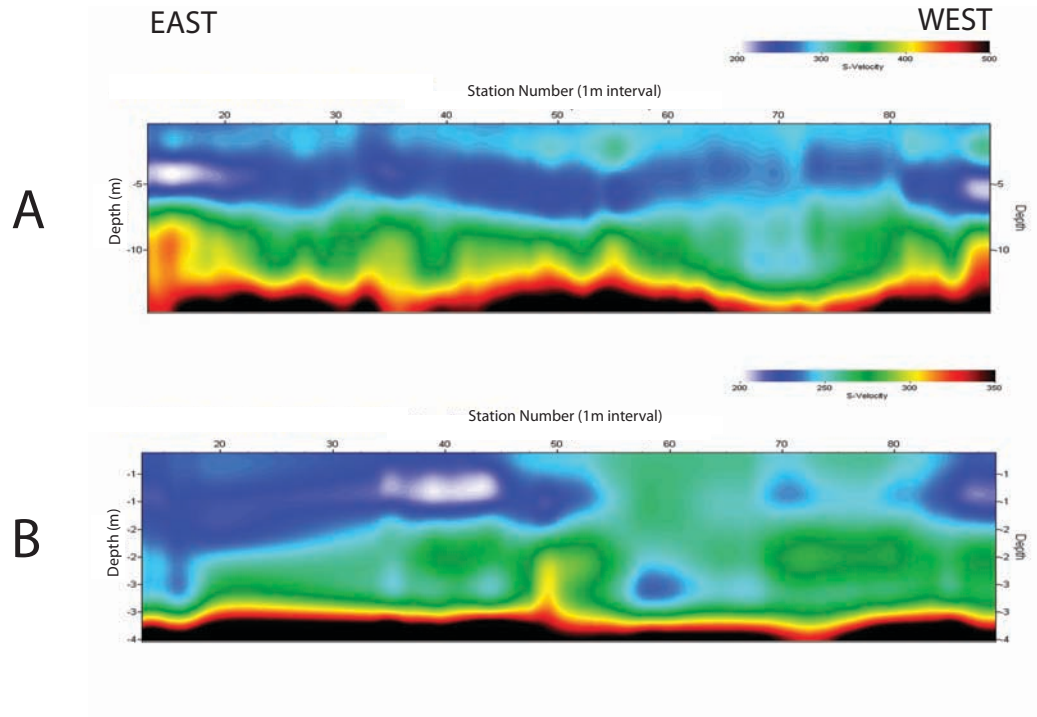


Figure 5.2: Active-source models for Line B; (A) full spread (VE = 1.1), (B) half spread (VE = 4.9).

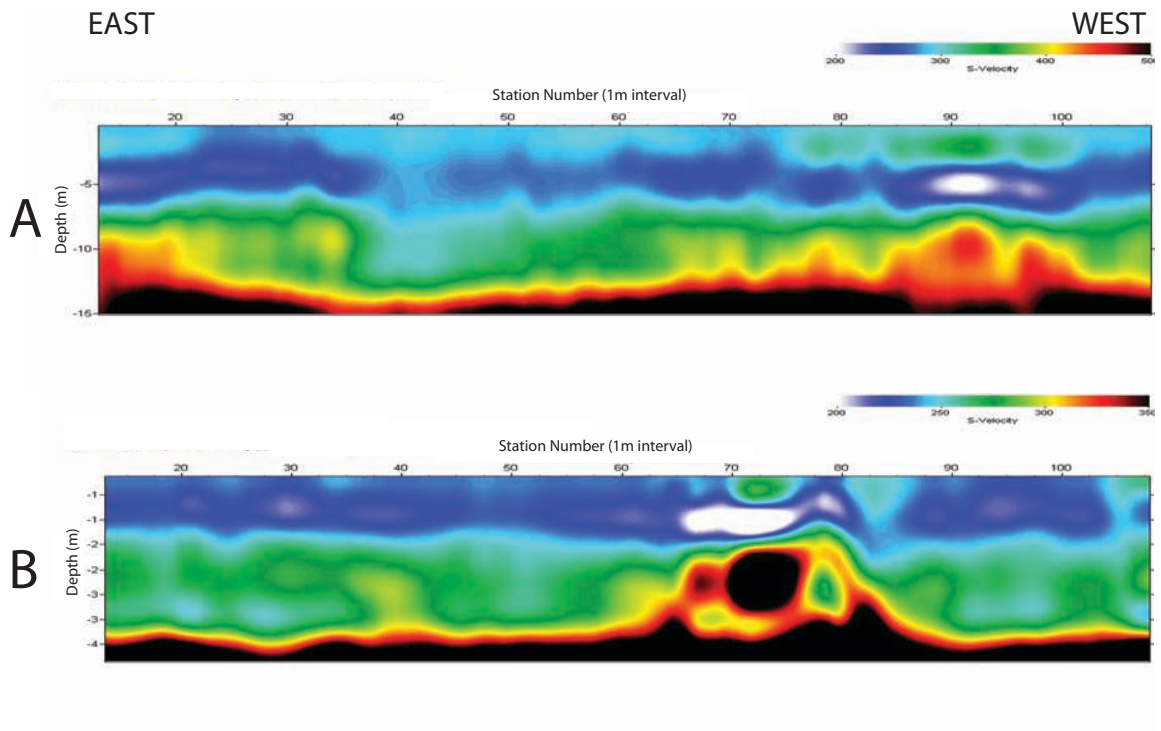


Figure 5.3: Active-source models for Line C; (A) full spread (VE = 1.1), (B) half spread (VE = 4.6).

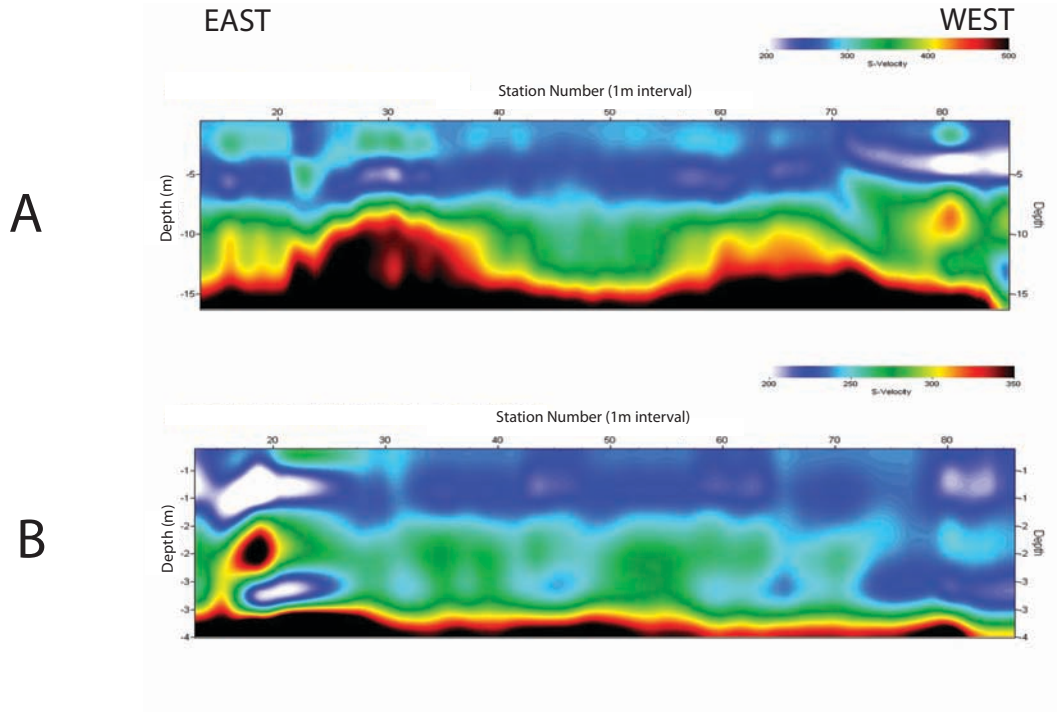


Figure 5.4: Active-source models for Line D; (A) full spread (VE = 1.1), (B) half spread (VE = 4.9).

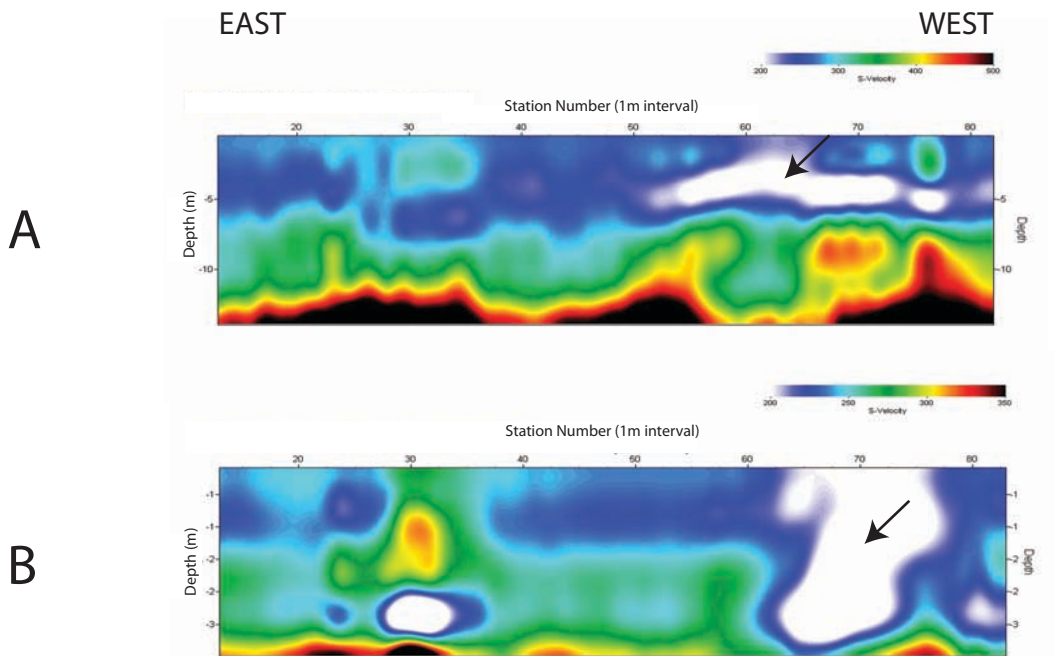


Figure 5.5: Active-source models for Line E; (A) full spread (VE = 1.3), (B) half spread (VE = 5.7). Arrow indicates low-velocity anomaly.

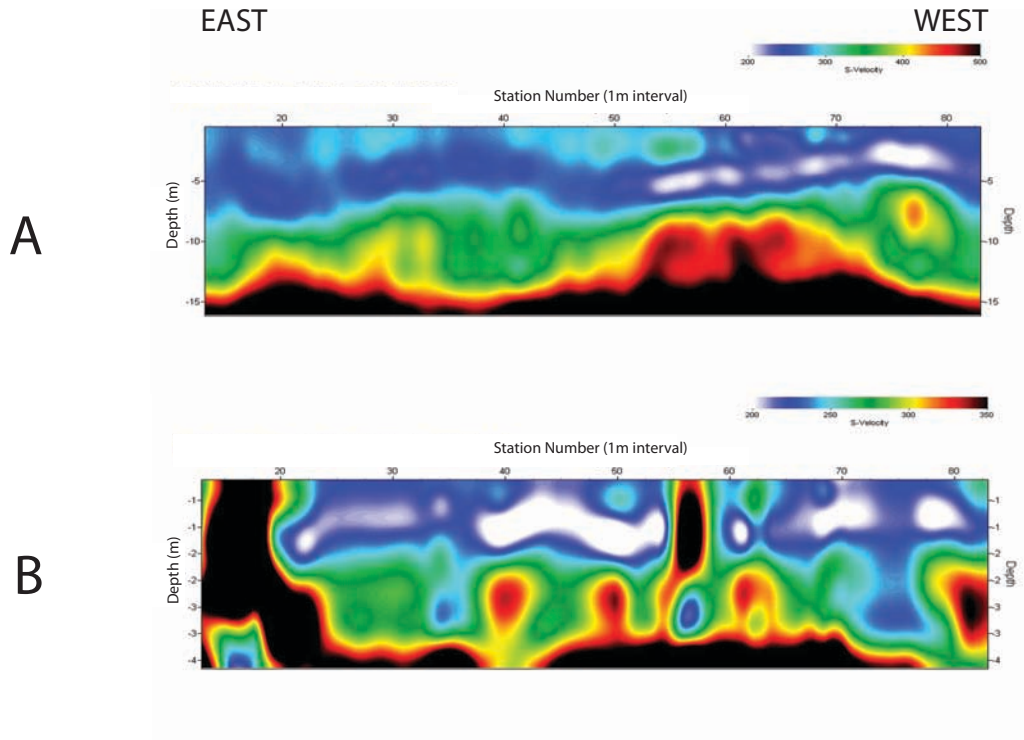


Figure 5.6: Active-source models for Line F; (A) full spread ($VE = 1.1$), (B) half spread ($VE = 4.7$).

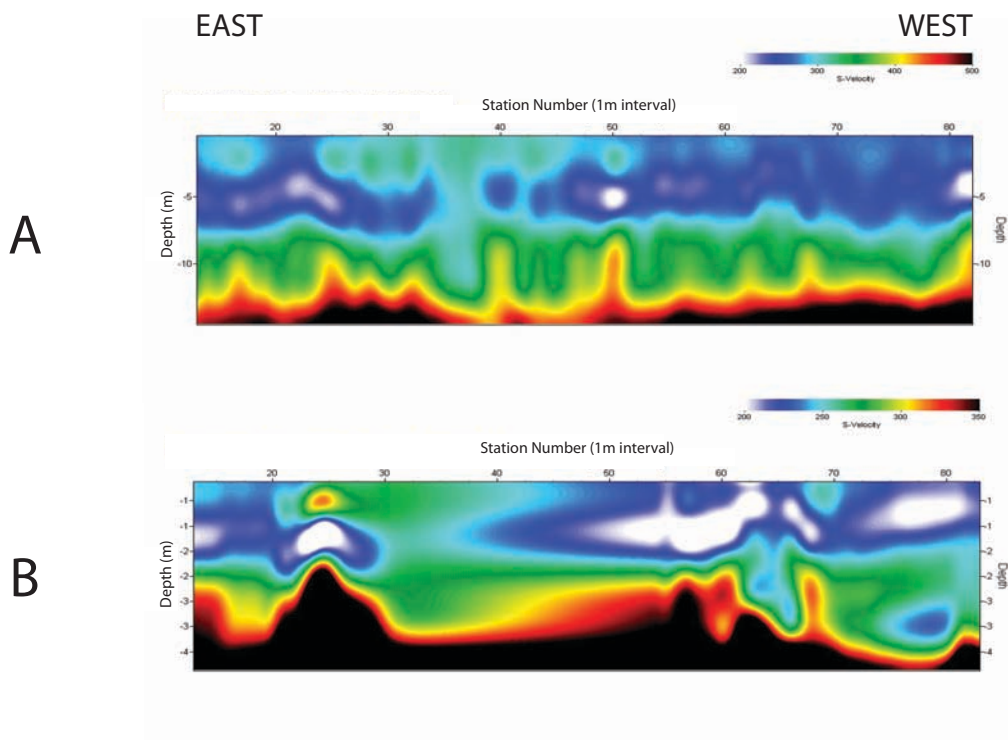


Figure 5.7: Active-source models for Line G; (A) full spread ($VE = 1.2$), (B) half spread ($VE = 4.6$).

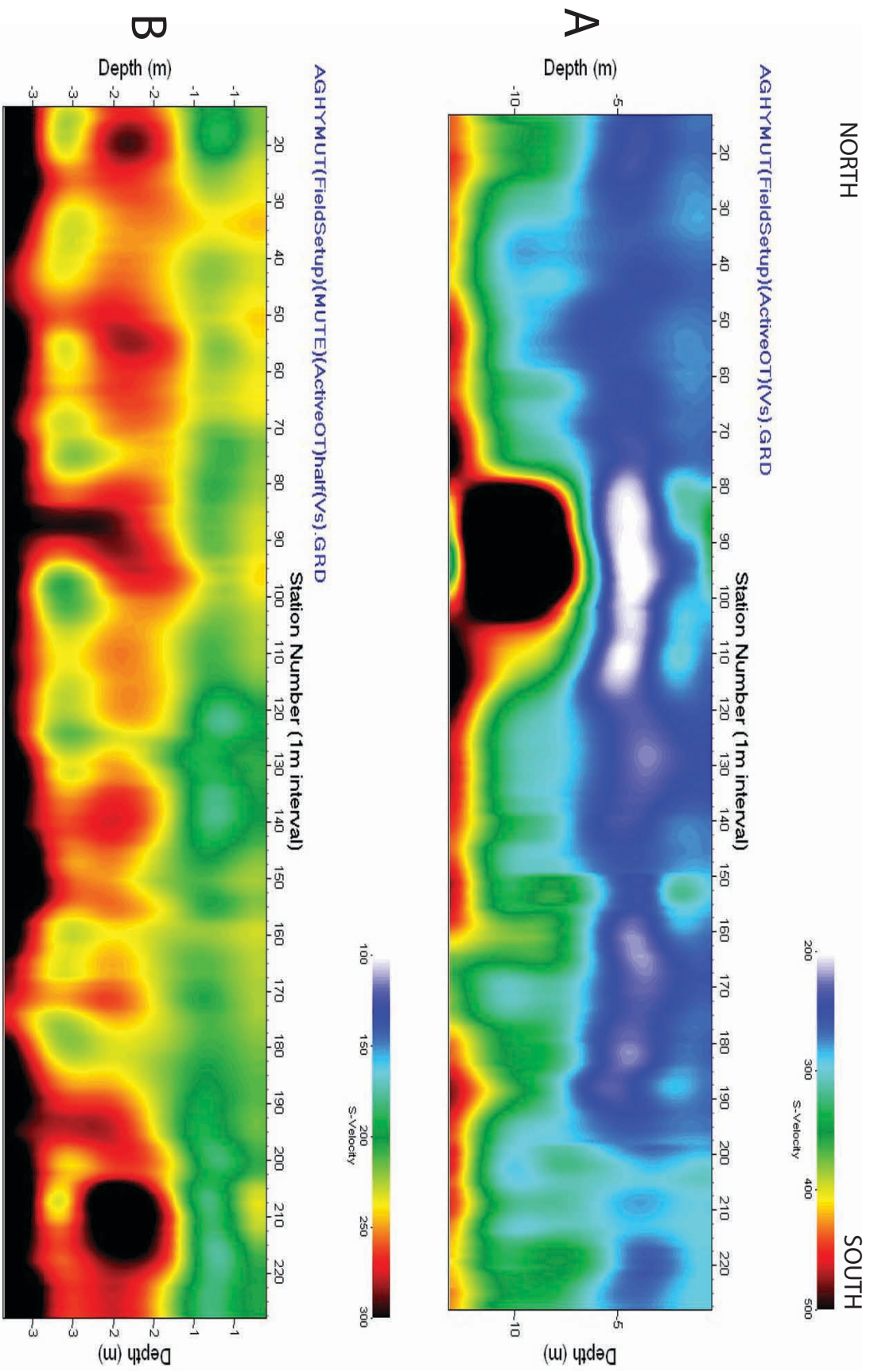


Figure 5.8: Active-source models for Line Y; (A) full spread (VE = 3.4), (B) half spread (VE = 14.2).

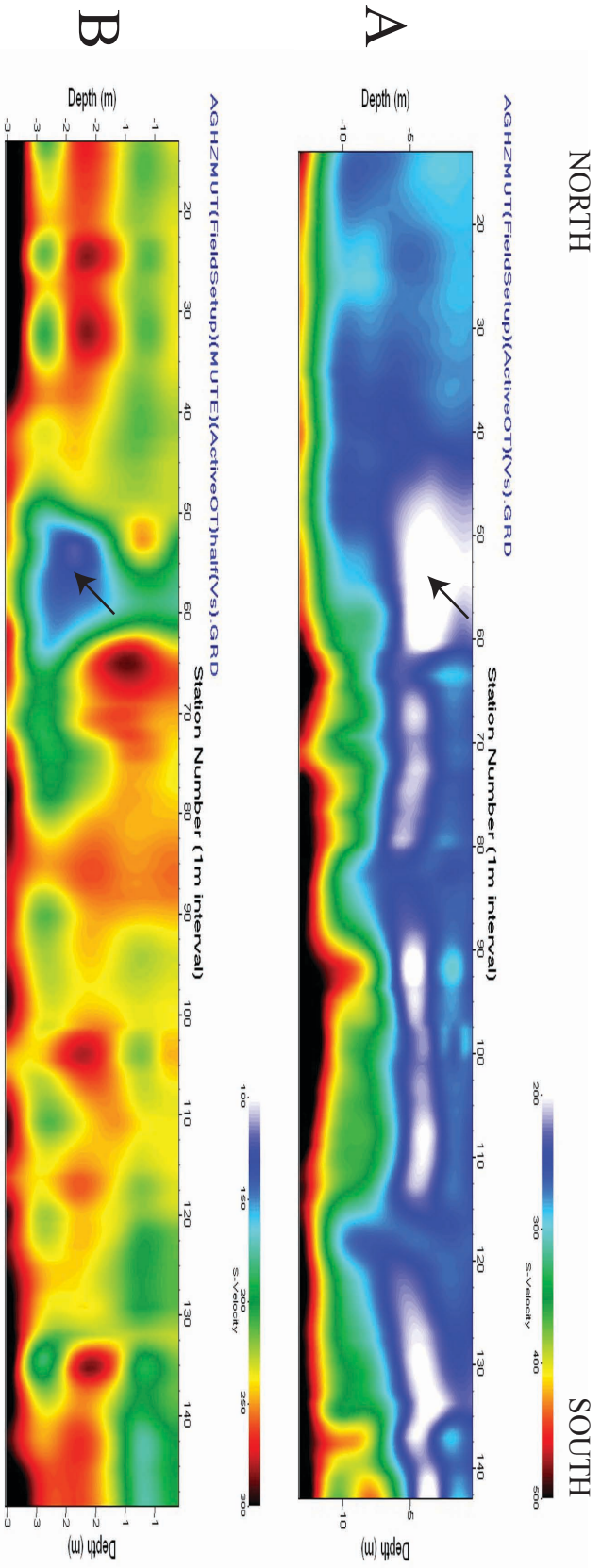


Figure 5.9: Active-source models for Line Z; (A) full spread (VE = 1.3), (B) half spread (VE = 5.8). Arrow indicates low-velocity anomaly.

CHAPTER 6

DISCUSSION

Processing issues and recommendations for future work

The shear-wave velocity profiles presented above are not unique models of the subsurface, so it is important to choose processing parameters that are appropriate for the depth range of interest. The final parameters depend upon the geology, target depth, seismic source, and the array length. Once the processing routine is in place, it is still necessary to ensure that the individual dispersion curve picks are based on high-quality data. The inversion process is sensitive to subtle changes in the shape of the dispersion curve, so it is critical to examine the features of each curve. It is also helpful to invert several versions of phase velocity picks for each profile to determine which features of the models are robust. Although the processing flow only involves three major steps, attention to each step is important for the final interpretation.

Since contamination of the fundamental mode is apparent at higher frequencies, a simplistic processing approach is recommended to obtain “conservative”, yet realistic models of the subsurface geology. For the active and passive surveys, a frequency range of 10-25 Hz was chosen based on the frequency spectra and characteristics of the overtone records. For the half-spread analysis, the shot gathers were muted to attenuate the higher-mode energy. Since muting can introduce artifacts at lower frequencies, the frequency range for the half-spread analysis was restricted to 35-100 Hz. Integrated

analysis of the models from three different depth ranges can provide better constraints on subsurface geology.

Interpretations of anomalous zones depend upon recognizing inherent limitations of the MASW technique; in particular, limitations on horizontal resolution related to the array length. Using synthetic data sets, O'Neill et al. (2008) demonstrated the limitations with regards to the lateral extent of an anomalous feature. They determined that only features greater than about half the array length are confidently resolved. Otherwise, smearing of shear-wave velocity structure due to averaging across the geophone spread obscures the anomaly (O'Neill et al., 2008). The lateral resolution for the active and passive surveys is low (11.5 and 23 meters, respectively), so smaller anomalies cannot be fully resolved with these array lengths. The half-spread analysis provides lateral resolution of approximately 6 meters. Once again, better lateral resolution is accompanied by decreased depth penetration. Despite these limitations, major karst features can still be identified by variations in shear-wave velocity. Potential subsidence features were identified on the shear-wave velocity models, and the alignment of low-velocity zones on the shear-wave velocity models (see Fracture zones and lineaments section below) may be indicative of widened bedrock fractures.

Resistivity would be a useful geophysical method to help resolve ambiguities and verify interpretations of the subsurface geology. This technique has been used in karst terrain to image bedrock topography, locate fracture zones, and detect air-filled voids in the subsurface (Nyquist et al., 2007). Since clay-rich soils are highly conductive and air-filled voids are extremely resistive (Nyquist et al., 2007), resistivity could be used to determine whether or not the anomaly at the intersection of Line A and Z is a void.

However, high resistivity associated with both voids and limestone makes differentiation of these features more difficult with resistivity. In this case, MASW is more useful because of the extreme difference in shear-wave velocity between bedrock and void space. Although resolution limits are also limited for resistivity surveys, the method would help constrain the geologic interpretations along existing seismic lines.

Shear-wave velocities for geologic materials

Borehole logs for AWGL wells were obtained from the USGS Water Science Center in Atlanta, GA for comparison with the seismic data. Although the depth to bedrock can vary significantly across a karst surface, the borehole log from well # 44 (Figure 1.4) is used here for comparison (other borehole logs within 1-2 km of the site support the conclusion that the bedrock varies in depth from 9 to 12 meters). The depth to limestone bedrock is 9 meters for well #44, which correlates with the steep vertical gradient in shear-wave velocity (and increase in velocity to values greater than 350 m/s) at a depth of 10 meters on the profile for Line D.

Shear-wave velocities for different geologic materials can be interpreted from the correlations between borehole and seismic data (Table 6.1). The depth to bedrock is defined by the 350 m/s shear-wave velocity contour line. Therefore, the interpreted shear-wave velocity for the soil overburden is 200-350 m/s. Below this contour, the variable increases in velocity with depth is attributed to different levels of weathering and fracturing of the limestone bedrock. Higher shear-wave velocities are likely indicative of more competent limestone bedrock. Fracture zones and highly weathered bedrock exhibit shear-wave velocities between 350-600 m/s, and more competent limestone in the study area exhibits shear-wave velocities between 600-700 m/s. Hicks et al. (1987) describe the

middle unit of the Ocala limestone as relatively impermeable, white to brown, clayey, dense, chalky limestone inter-layered with non-calcareous clay and silt. The measured shear-wave velocities are primarily representative of the Ocala formation, but the velocity information may also be relevant for other limestone with similar lithology.

Potential subsidence features

A striking example of a potential subsidence feature at the intersection of Lines A and Z was presented in Chapter 4. The shot gathers indicate that the feature is approximately 11 meters long and 8 meters wide. Since the feature is larger than the resolution width of the half-spread analysis (6 meters), the anomaly is well resolved on the half-spread models for Line A and Z (Figures 5.1 and 5.9). For the full-spread active-source model, the anomaly is distorted because the feature is slightly smaller than the resolution width for this array. On the passive-source model for Line A (Figure 2.10B), there is a subtle decrease in shear-wave velocity from STA 78-87. Dispersion curves for STA 79 on Line A are presented in Figure 6.1. Although this may be an exceptional example of a potential collapse feature, it seems reasonable that less prominent low-velocity zones can still be identified by decreased shear-wave velocity on the models.

The back-filled sinkhole from 2007 that intersects Line A at approximately STA 130-132 provides an opportunity to analyze the MASW signature in an area of recent subsidence. Figure 2.10A shows a distinct depression in shear-wave velocity at approximately STA 130-132 at depths of 15-20 meters. The anomaly is not as obvious as others on the same model, and this could be explained by the filled or partially filled void. A corresponding signature on the passive model (Figure 2.10B) is not evident, but the smearing effect from the 46-m array is expected to obscure the subsidence signature.

However, it is noteworthy that the section from STA 130-147 has the lowest average shear-wave velocity structure on the profile. The relatively deep position of the 450 m/s contour line indicates lower overall shear-wave velocity in this zone. Clear evidence of a fracture is lacking, but sinkhole formation appears to be related to a highly fractured zone within the bedrock. The dispersion curves for STA 131 on Line A (Figure 6.2) do not indicate any fundamental problems with the data quality. Dispersion curves for STA 30-31 (competent bedrock) are presented for comparison (Figure 6.3). The phase velocity associated with the low frequency amplitude peak is considerably higher for the latter records.

The interpretation of subsidence features in karst terrain is difficult because of the inherent complexity of the subsurface and MASW resolution limits. Shear-wave velocity models clearly show low-velocity zones, but interpretations of anomalies can include sinkholes, voids, fractured bedrock, as well as naturally in-filled collapse features. Smearing of the shear-wave velocity pattern is a major limitation, but the presence of anomalous zones in association with highly fractured bedrock or small voids may still appear as a down-warping of the shear-wave velocity contours.

Fracture zones and lineaments

The linear expression of sinkholes on Figure 1.7 suggests association with a major north-south trending bedrock fracture zone. Although it is difficult to determine the exact orientation of the fracture, a low-velocity zone on Line A generally aligns with the trend. The prominent anomaly at STA 110 on the active-source model for Line A (Figure 2.10A) may correspond to the suspected fracture. On the passive-source model (Figure 2.10B), the pronounced down-warping of the shear-wave velocity contours that occurs at

STA 115 could also be indicative of the fracture. A LVZ is evident at STA 100-110 on the active model for Line C (Figure 2.12A), but the correlation is more speculative because the passive survey profile does not extend this far.

Figure 6.4 shows the shear-wave velocity models for Lines A-G and the apparent alignment of LVZ's along fracture trends. The blue and red arrows correspond to trends of N10°W and N55°E, respectively. The green arrows show the alignment of bedrock ridges adjacent to the north-trending low-velocity zones. Since it is difficult to determine the exact location of the fracture within relatively wide low-velocity zones, the uncertainty for the azimuth is estimated to be 5-10 degrees. Despite the ambiguity, these trends roughly correspond to the 5° and 40° fracture azimuths measured by Brook and Allison (1983). The north-south trend is also consistent with observed sinkhole development at the site.

The LVZ at the intersection of Lines A and Z may also be related to the north-south trending fracture zone. Figure 6.5 shows the suspected orientation of fractures within the study area. The westernmost fracture directly corresponds to the alignment of sinkholes as well as the 5° preferred orientation. Since fracture sets are often parallel (Engelder, 1987), it is certainly plausible that the LVZ and the two sinkholes to the east formed along a second fracture. Line Z is coincident with the suspected fracture trace, and the passive-source model shows consistently low shear-wave velocities (400-550 m/s) at depths of 10-20 meters across most of the profile. By contrast, shear-wave velocities of 550-600 m/s are evident on Line Y for the same depth range. The elongation direction of the LVZ also supports this conclusion.

Lineament analysis in this study is severely limited by the relatively short length of the lines, high lateral variation on the models, and complicated fracture patterns. The above interpretation is simply a preliminary assessment, but the observed trends can be used to guide future studies. More data is required to confidently assess the suspected lineament orientations.

Regional joint sets and fracture mechanics

Jointing can be caused by tectonic stress, thermal-elastic contraction during uplift, or high pore-fluid pressure in strata (Engelder, 1987, Arlegui and Simon, 2001). Joint propagation is typically normal to the least principal stress, and displacement along the joint plane can occur when there is a shear component of stress (Engelder, 1987). The precise mechanism for jointing on a regional scale can be difficult to determine because orientations of unloading joints can be controlled by either residual or contemporary stress fields (Engelder, 1987). Several studies have used joint patterns to infer the orientation of tectonic stress fields (Arlegui and Simon, 2001; Whitaker and Engelder, 2005).

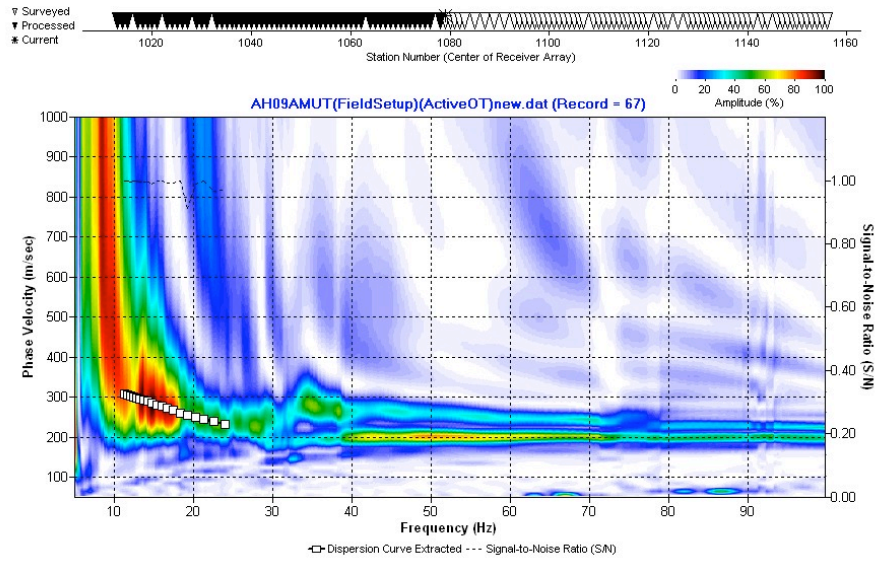
Vernon (1951) originally recognized a regional joint pattern in Florida, and Brook and Allison (1983) have documented similar fracture patterns in exposed limestone along the Flint River in Dougherty County, Georgia. The Ocala Formation (Eocene age) and underlying strata were deposited on a shallow-water marine platform in a passive margin tectonic setting (Randazzo, 1997). Unloading joints may have formed as a response to erosion and exhumation resulting from tectonic or eustatic changes (Randazzo, 1997). Brook and Allison (1983) hypothesized that the fractures oriented at 40 and 325 degrees represent conjugate shear fractures.

This study provides limited insight regarding regional fracture patterns due to the inherently low resolution of the MASW technique and the limited spatial extent of the profiles. Instead, known fracture orientations can be used to guide MASW investigations and aid the interpretation of subsidence features. The results of this study do not provide clear evidence of lineament orientations, but low-velocity anomalies on the shear-wave profiles may be indicative of fracture zones.

Table 6.1: Interpreted shear-wave velocities for geologic materials

<u>Interpretation of Shear-wave Velocities for Geologic Materials</u>	
<u>Material</u>	<u>S-wave velocity</u>
Sandy/clay soil and clay residuum	200-350 m/s
Highly-fractured limestone	350-600 m/s
Competent limestone	600-700 m/s

A)



B)

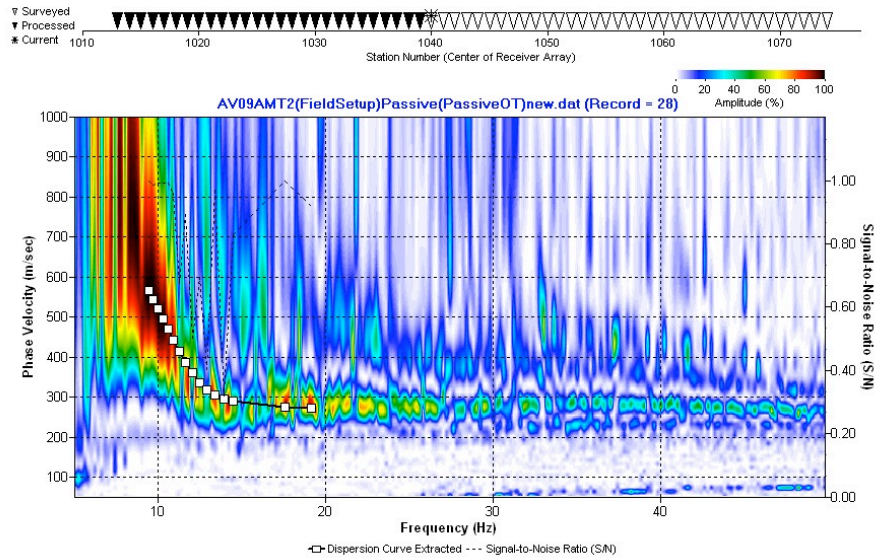
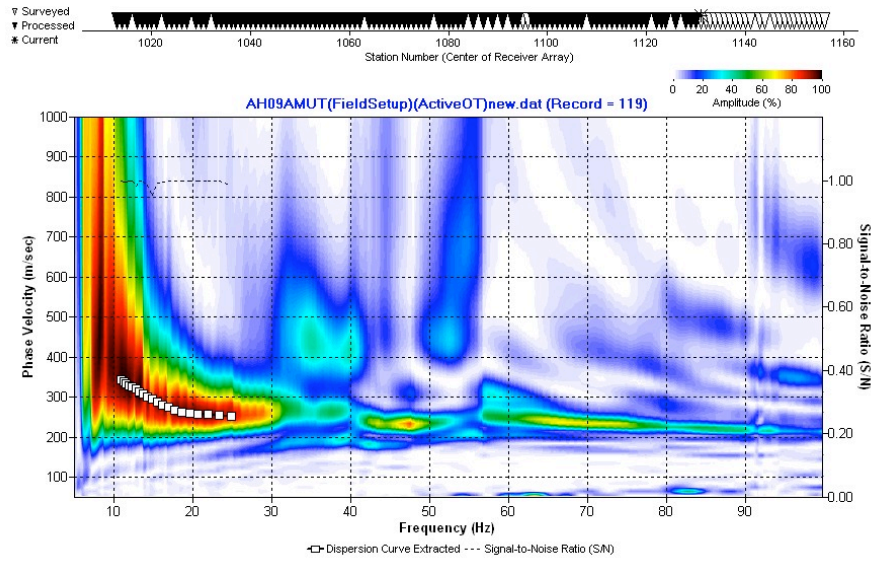


Figure 6.1: (A) Active-source overtone image (amplitude contour plot) and dispersion curve picks (squares) for STA 79 within the LVZ on Line A. Note the branching of the amplitude peak at frequencies greater than 30 Hz; (B) Passive-source overtone image (amplitude contour plot) and dispersion curve picks (squares) for STA 79 within the LVZ on Line A.

A)



B)

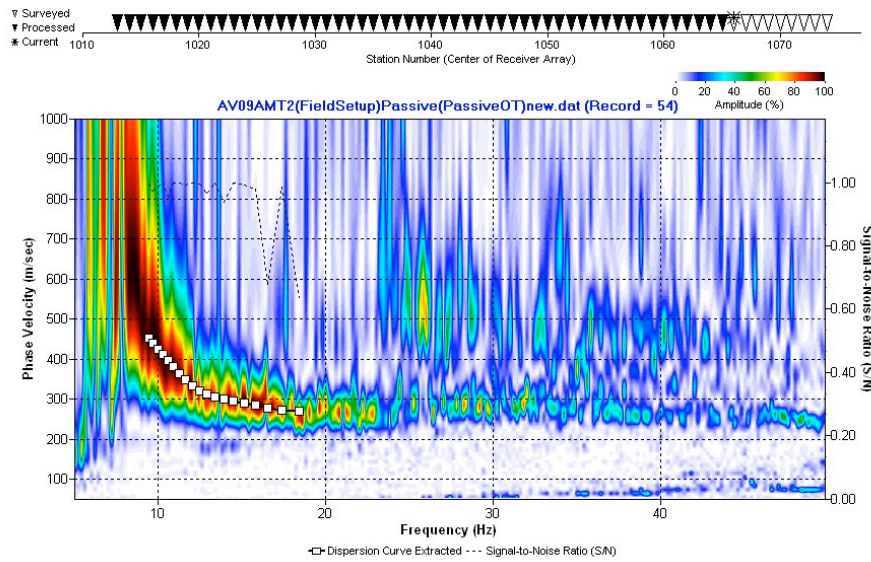
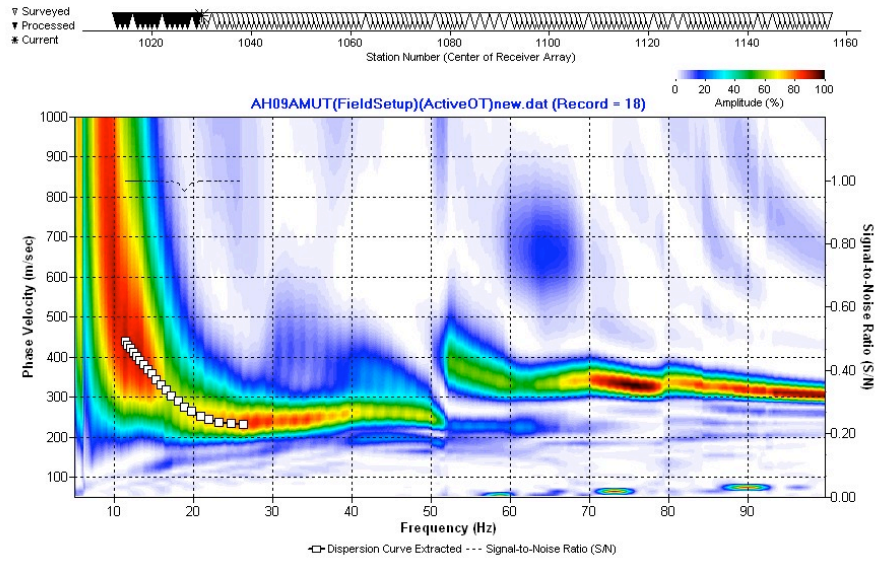


Figure 6.2: (A) Active-source overtone image (amplitude contour plot) and dispersion curve picks (squares) for STA 131 on Line A. (B) Passive-source overtone image (amplitude contour plot) and dispersion curve picks (squares) for STA 131 on Line A.

A)



B)

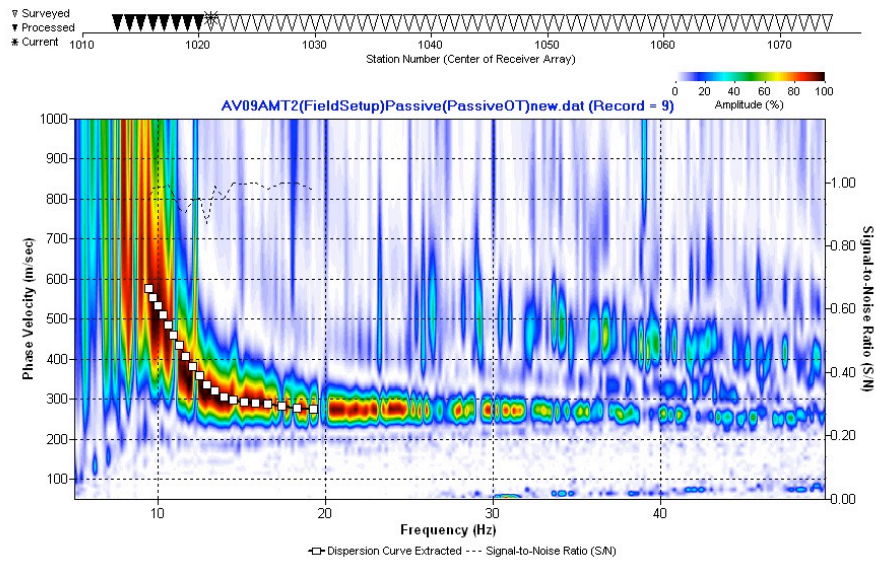


Figure 6.3: (A) Active-source overtone record (amplitude contour plot) and dispersion curve picks (squares) for STA 30 on Line A. (B) Passive-source overtone image (amplitude contour plot) and dispersion curve picks (squares) for STA 31 on Line A.

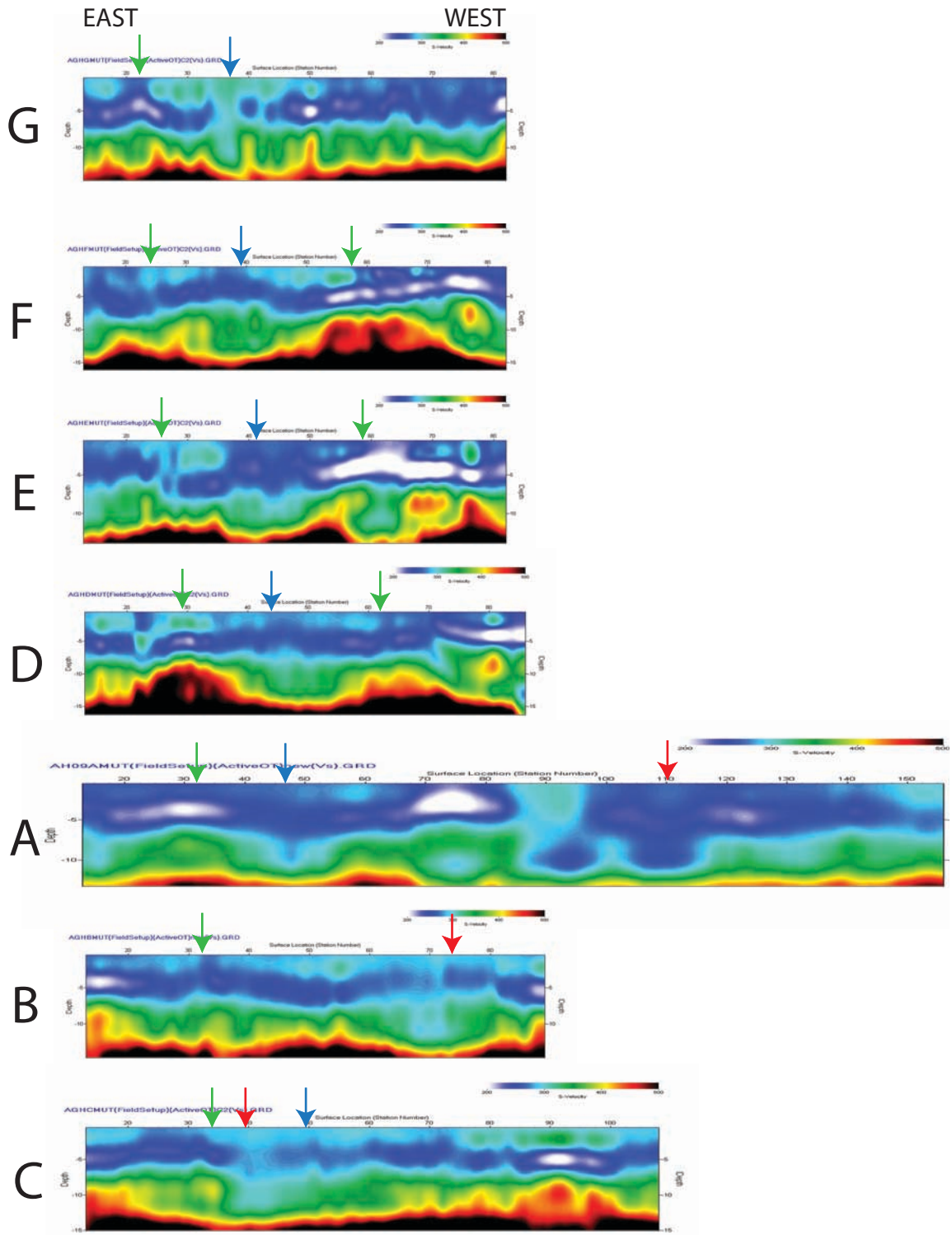


Figure 6.4: Shear-wave velocity models for Lines A-G with arrows indicating apparent trends in bedrock topography. The red arrows indicate alignment of LVZ's trending N55°E. Blue arrows indicate the alignment of LVZ's trending N10°W, and the green arrows show the position of corresponding bedrock ridges on both sides of the LVZ trend. Note that the trend of the seismic lines is N85°W. Estimated uncertainty: 5°-10°.

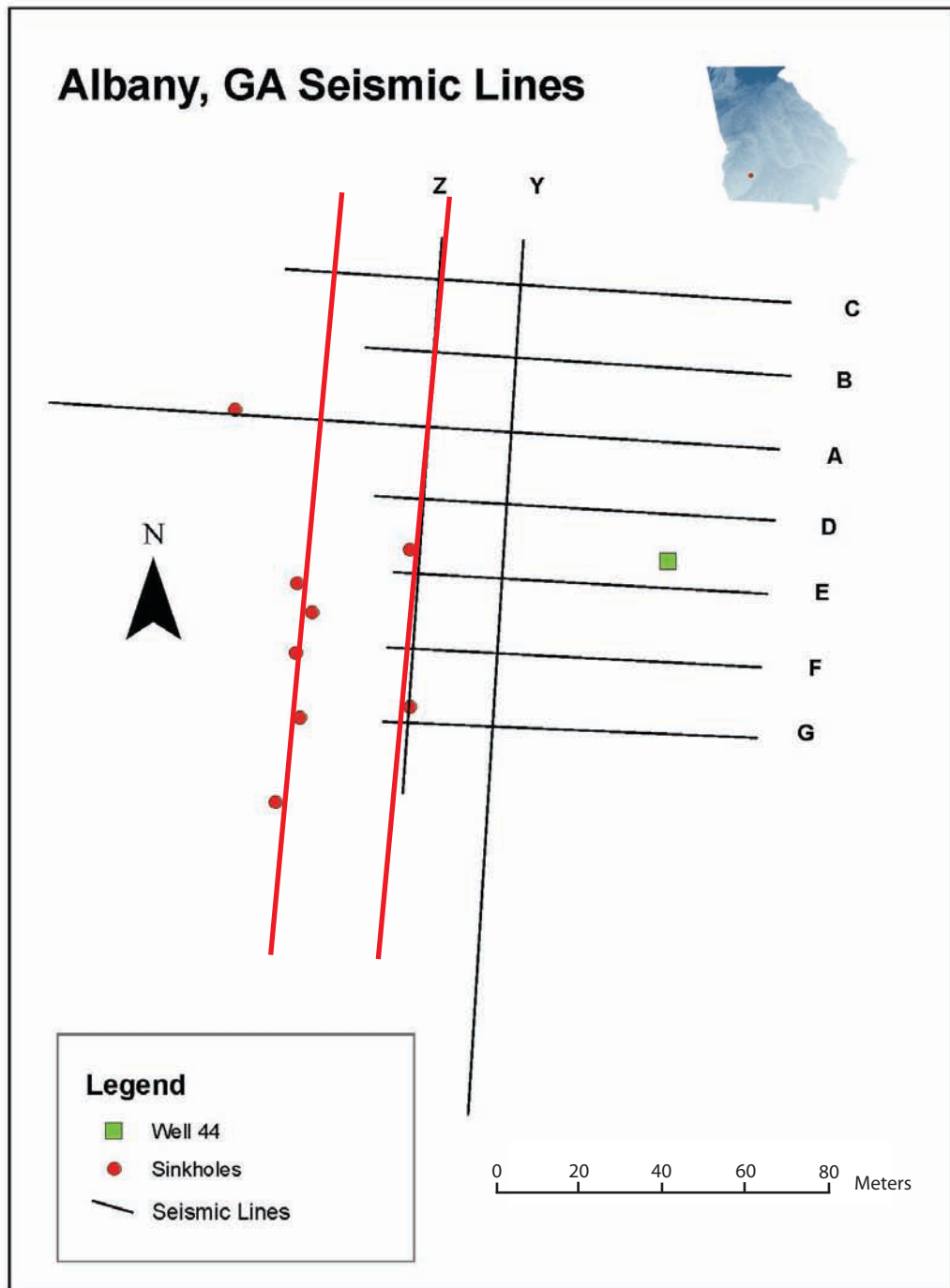


Figure 6.5: Suspected fracture trends based on sinkhole formation and the low-velocity zone at the intersection of Lines A and Z.

CHAPTER 7

CONCLUSIONS

Multi-channel Analysis of Surface Waves (MASW) was used to map bedrock topography and locate a potential subsidence feature along a suspected fracture zone in karst terrain. Surface-wave data were acquired along seven parallel lines and two perpendicular cross-lines. Active-source and passive-source seismic surveys were conducted to image depth ranges of 4, 12, and 23 meters. For the passive survey, a van moving in line with the array was used to generate lower frequency energy. The geophone spread was 46 meters, so the penetration depth and lateral resolution width was approximately 23 meters. A sledge-hammer was used as the seismic source for the active survey. The geophone spread was 23 meters, so the penetration depth and lateral resolution width was approximately 12 meters (half the array length). Half of the traces for the active survey were analyzed separately to improve lateral resolution (6 meters). Spatial windowing with subsets of traces was also used to improve the spatial resolution of suspected shear-wave velocity anomalies.

Since lateral resolution trades off with depth penetration, the shear-wave velocity models for three different depth ranges were analyzed to overcome the inherent limitations of the surface-wave technique. The passive-source models provide a broad image of the sub-surface to a depth of 23 meters, and the average depth to bedrock of 9-10 meters correlates with the borehole log for well #44. The full-spread active-source models for the uppermost 12 meters indicate lateral variations in bedrock topography

expected in karst terrain. However, the lateral resolution width is 12 meters, so smaller features are not fully resolved. The half-spread analysis significantly improves the lateral resolution for depths of approximately 4 meters.

The prominent low-velocity zone at the intersection of Lines A and Z is interpreted to be a potential subsidence feature. Distinct changes in apparent velocity across the shot gathers at this intersection are indicative of a low-velocity zone approximately 11 meters long and 8 meters wide. The anomaly is evident on the full-spread active-source model, but the image is smeared because the feature is smaller than the resolution width (12 meters). The spatial extent of the anomaly is well constrained with the half-spread analysis because the feature is larger than the resolution width (6 meters). The alignment of the LVZ with two other sinkholes at the site suggests that the feature formed along a fracture zone trending N5°E. Observed sinkhole patterns at the site and previous fracture data support this interpretation.

Shear-wave velocities were obtained for sandy-clay soils and limestone bedrock. The depth to bedrock is defined by the steep shear-wave velocity gradient at 350 m/s. Shear-wave velocities for the soil overburden range from 150-350 m/s. The velocities for fractured limestone bedrock range from 350 m/s to 700 m/s. The limestone bedrock exhibits gradational changes in shear-wave velocity due to variations in weathering and fracturing. Lenses of clay and silt within the limestone may also affect the velocity variations. Shear-wave velocities for more competent Ocala limestone range from 600-700 m/s.

REFERENCES

Arlegui, L., and J.L. Simon, 2001, Geometry and distribution of regional joint sets in a non-homogenous stress field: case study in the Ebro basin (Spain): *Journal of Structural Geology*, 23, 297-313.

Aki, K. and P.G. Richards, 2002, *Quantitative Seismology* (2nd Edition), University Science Books.

Alhadeff, S.J., J.W. Musser, A.C. Sandercock, and T.R. Dyar, 2001, *Digital Environmental Atlas of Georgia: Georgia Geologic Survey Publication CD-1*, 2 CD-ROM set.

Andrus, R.D., and K.H. Stokoe, 2000, Liquefaction resistance of soils from shear-wave velocity: *Journal of Geotechnical and Geoenvironmental Engineering*: 126, 1015-1025.

Baechle, G.T., G.P. Eberli, R.J. Weger, and J.L. Massafero, 2009, Changes in dynamic shear moduli of carbonate rocks with fluid substitution: *Geophysics*, 74, E135-E147.

Brinkmann, R., M. Parise, and D. Dye, 2008, Sinkhole distribution in a rapidly developing urban environment: Hillsborough County, Tampa Bay area, Florida: *Engineering Geology*, 99, 169-184.

Brook, G.A., and T.L. Allison, 1983, Fracture mapping and ground subsidence susceptibility modeling in covered karst terrain: Dougherty County, Georgia, *in*, P.H. Dougherty, ed., *Environmental Karst*: Geospeleo Publications.

Denizman, C., 2003, Morphometric and spatial distribution parameters of karstic depressions, lower Suwannee River basin, Florida: *Journal of Cave and Karst Studies*, 65, 29-35.

Doolittle, J.A., and M.E. Collins, 1998, Comparison of EM induction and GPR methods in areas of karst: *Geoderma*, 85, 83-102.

Engelder, T., 1987, Joints and shear fractures in rock, *in*, B.K. Atkinson, ed., *Fracture mechanics of rock*: Academic Press Geology Series, 27-65.

Ford, D. and P. Williams, 2007, *Karst hydrogeology and geomorphology*: John Wiley & Sons Ltd.

Galve, J.P., Bonachea, J., Remundo, J., Gutierrez, F., Guerrero, J., Lucha, P., Cendrero, A., Gutierrez, M., and Sanchez, J.A., 2008, Development and validation of sinkhole susceptibility models in mantled karst settings: A case study from the Ebro valley evaporate karst (NE Spain): *Engineering Geology*, 99, 185-197.

Gaswirth, S.B., D.A. Budd, and B.R. Crawford, 2006, Textural and stratigraphic controls on fractured dolomite in a carbonate aquifer system, Ocala limestone, west-central Florida: *Sedimentary Geology*, 184, 241-254.

Gordon, D.W., 2008, Ground-water conditions and studies in the Albany area of Dougherty County, Georgia, 2007: U.S. Geological Survey Open-File Report 2008-1328.

Hayes, L.R., M.L. Maslia, and W.C. Meeks, 1983, Hydrology and model evaluation of the principal artesian aquifer, Dougherty Plain, southwest Georgia: *Georgia Geologic Survey Bulletin* 97.

He, L., M. Feng, Z. He, and X. Wang, 2006, Application of EM Methods for the Investigation of Qiyueshan Tunnel, China: *Journal of Environmental and Engineering Geology*, 11, 151-156.

Hicks, D.W., G.E. Gill, and S.A. Longworth, 1987, Hydrogeology, chemical quality, and availability of ground water in the Upper Floridan Aquifer, Albany area, Georgia: U.S. Geological Survey Water-Resources Investigations Report 87-4145.

Higuera-Diaz, I.C, P.J. Carpenter, and M.D. Thompson, 2007, Identification of buried sinkholes using refraction tomography at Ft. Campbell Army Airfield, Kentucky: *Environmental Geology*, 53, 805-812.

Hyatt, J.A., and P.M. Jacobs, 1996, Distribution and morphology of sinkholes triggered by flooding following Tropical Storm Alberto at Albany, Georgia, USA: *Geomorphology*, 17, 305-316.

Ivanov, J., C.B. Park, R.D. Miller, and J. Xia, 2005, Analyzing and filtering surface-wave energy by muting shot gathers: *Journal of Environmental and Engineering Geophysics*, 10, 307-322.

Lin, C., C. Chang, and T. Chang, 2004, The use of MASW method in the assessment of soil liquefaction potential: *Soil Dynamics and Earthquake Engineering*, 24, 689-698.

Luke, B., W. Taylor, C. Calderon-Macias, X. Jin, H. Murvosh, and J. Wagoner, 2008, Characterizing anomalous ground for engineering applications using surface-based seismic methods: *The Leading Edge*, 27, 1544-1549.

Maupin, M.A., and N.L. Barber, 2005, Estimated withdrawals from principal aquifers in the United States, 2000: U.S. Geological Survey Circular 1279.

McMechan, G.A., and M.J. Yedlin, 1981, Analysis of dispersive waves by wave field transformation: *Geophysics*, 46, 869-874.

Miller, R.D., J. Xia, and C.B. Park, 2005, Seismic techniques to detect dissolution features (karst) at a proposed power-plant site, *in*, D.K. Butler, ed., *Near surface geophysics: Society of Exploration Geophysicists*, 663-679.

Nasser-Moghaddam, A., G. Cascante, C. Phillips, and D.J. Hutchinson, 2007, Effects of underground cavities on Rayleigh waves – Field and numerical experiments: *Soil Dynamics and Earthquake Engineering*, 27, 300-313.

Nazarian, S., K.H. Stokoe II, and W.R. Hudson, 1983, Use of spectral analysis of surface waves method for determination of moduli and thickness of pavement systems: *Transport Research Record*, 930, 38-45.

Nyquist, J.E., J.S. Peake, and M.J.S. Roth, 2007, Comparison of an optimized resistivity array with dipole-dipole soundings in karst terrain: *Geophysics*, 72, F139-F144.

O'Neill, A., T. Campbell, and T. Matsuoka, 2008, Lateral resolution and lithological interpretation of surface-wave profiling, *The Leading Edge*, 27, 1550-1563.

Odum, J.K., R.A. Williams, W.J. Stephenson, D.M. Worley, C. von Hillebrandt-Andrade, E. Asencio, H. Irizarry, and A. Cameron, 2007, Near-surface shear wave velocity versus depth profiles, Vs 30, and NEHRP classifications for 27 sites in Puerto Rico: USGS Open-File Report 2007-1174.

Officer, C.B., 1974, Introduction to Theoretical Geophysics: Springer-Verlag.

Parizek, R.R., 1976, On the nature and significance of fracture traces and lineaments in carbonate and other terranes, *in*, V. Yevjevich, ed., Karst hydrology and water resources; Proceedings of the U.S.-Yugoslavian Symposium, Dubrovnik, 1975, Volume 1: Water Resources Publications, 47-100.

Park, C.B., R.D. Miller, and J. Xia, 1999, Multichannel Analysis of Surface Waves: Geophysics, 64, 800-808.

Park, C.B., R. Miller, M. Brohammer, J. Xia, and J. Ivanov, 2000, Using Surfseis[©] 2000: For multichannel analysis of surface waves (MASW): Kansas Geological Survey.

Park, C.B., R.D. Miller, N. Ryden, J. Xia, and J. Ivanov, 2005, Combined use of active and passive surface waves: Journal of Environmental and Engineering Geology, 10, 323-334.

Park, C.B., R.D. Miller, J. Xia, and J. Ivanov, 2007, Multichannel analysis of surface waves (MASW) - active and passive methods: *The Leading Edge*, 26, 60-64.

Pollack, H.N., 1963, Effect of delay time and number of delays on the spectra of ripple-fired shots: *Earthquake Notes*, 34, 1-12.

Randazzo, A.F., 1997, The sedimentary platform of Florida: Mesozoic to Cenozoic, *in*, A.F. Randazzo, and D.S. Jones, eds., *The geology of Florida*: University Press of Florida, 39-56.

Rix, G.J., and E.A. Leipski, 1991, Accuracy and resolution of surface wave inversion, *in*, S.K. Bhatia, and G.W. Blaney, eds., *Recent advances in instrumentation, data acquisition and testing in soil dynamics*: American Society of Civil Engineers, 17-32.

Schrott, L. and O. Sass, 2008, Application of field geophysics in geomorphology: Advances and limitations exemplified by case studies: *Geomorphology*, 93, 55-73.

Stewart, L.M., D. Warner, and B.J. Dawson, 1999, Hydrogeology and water quality of the Upper Floridan Aquifer, western Albany area, Georgia: USGS Water-Resources Investigations Report 99-4140.

Stokoe, K.H., II, G.W. Wright, A.B. James, and M.R. Jose, 1994, Characterization of geotechnical sites by SASW method, *in*, R.D. Woods, ed., Geophysical characterization of sites, ISSMFE Technical Committee #10: Oxford Publications.

Tam, V.T., F. De Smedt, O. Batelaan, and A. Dassargues, 2004, Study on the relationship between lineaments and borehole specific capacity in a fractured and karstified limestone area in Vietnam: *Hydrogeology Journal*, 12, 662-673.

Thierry, P., N. Debeblia, and A. Bitri, 2005, Geophysical and Geological characterization of karst hazards in urban environments: application to Orleans (France): *Bulletin of Engineering Geology and the Environment*, 64, 139-150.

Vernon, B.O., 1951, *Geology of Citrus and Levy Counties, Florida*: Geological Bulletin 33, Florida Geological Survey.

Waltham, T., F. Bell, and M. Culshaw, 2005, *Sinkholes and subsidence: karst and cavernous rocks in engineering and construction*: Praxis Publishing Ltd.

Whitaker, A.E., and T. Engelder, 2005, Characterizing stress fields in the upper crust using joint orientation distributions: *Journal of Structural Geology*, 27, 1778-1787.

Xia, J., R.D. Miller, and C.B. Park, 1999, Estimation of near-surface shear-wave velocity by inversion of Rayleigh waves: *Geophysics*, 64(3), 691-700.

Xia, J., R.D. Miller, X. Yixian, L. Yinhe, C. Chao, L. Jiangping, J. Ivanov, and C. Zeng, 2009, High Frequency Rayleigh-Wave Method: *Journal of Earth Science*, 20, 563-579.

APPENDIX A

PROCESSING DETAILS

Eavesdropper

The 'edmt' command in Eavesdropper was used to mute bad traces while preserving the station positions in the shot gathers. This procedure was utilized for the active and passive data sets to eliminate noisy traces. Trace one for each shot record was not edited because it generated a floating point error within Surfseis (Figure A1).

The geometry was encoded for the shot gathers based on the source-sequence number and recording channel number.

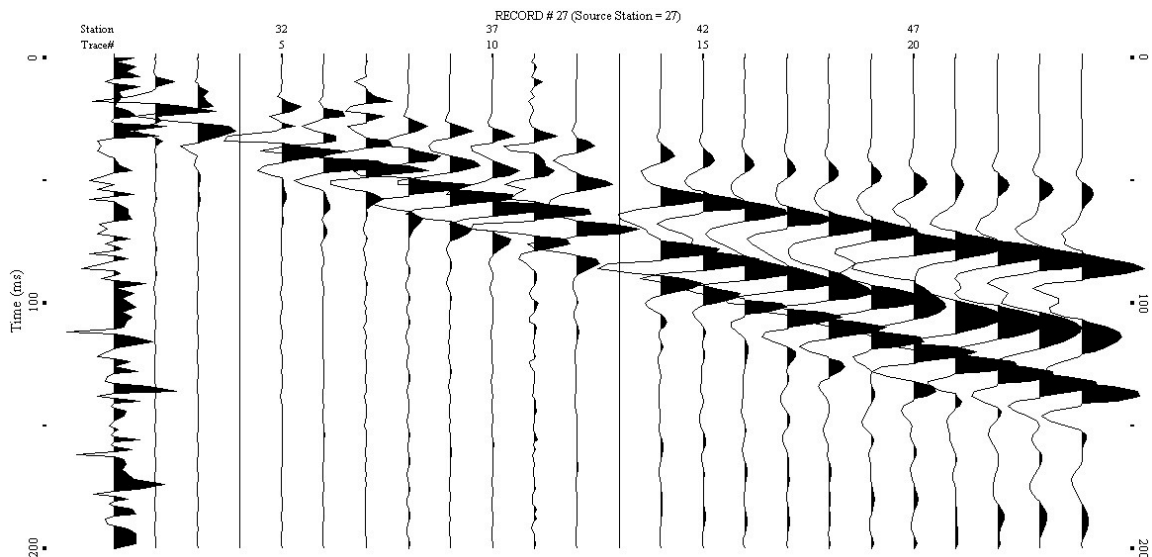


Figure A1: Shot gather showing noisy first trace. Notice that trace 4 and 13 are muted.

Surfseis: Dispersion 1

Dispersion 1 can be used to create an output file containing muted shot gathers.

The following steps illustrate the processing flow.

- 1) Select input seismic data file (*.DAT) for processing
- 2) Image: Parameter Dialog Box: Time/Trace: Adjust the display time range to 0-200 ms
enlarge this section of the seismogram
- 3) Process: MUTE (right click): Select top mute and mild tapering (~10000 ms). Choose output file name and check 'Append Output' box.
- 4) MUTE (left click): Use the mouse to define mute setting. Double-click to mute, and move to the next record. The program will save muted shot gathers to the specified output file. Open the output file with Dispersion 2 for subsequent processing.

Surfseis: Dispersion 2

- 1) Open input file (*.DAT) of original shot gathers or muted gathers.
- 2) Select output file name
- 3) Process Parameters
 - a) Select appropriate frequency and phase velocity ranges for the overtone record.
 - b) Contrast level refers to the relative emphasis of the dominant mode in comparison to other energy on the overtone plot. Low contrast (1-2) is initially recommended to display energy associated with higher mode surface waves.
 - c) Algorithm: The 'Normal' algorithm was used with Dispersion (2). Figures A2 and A3 show the overtone images generated using different algorithms.

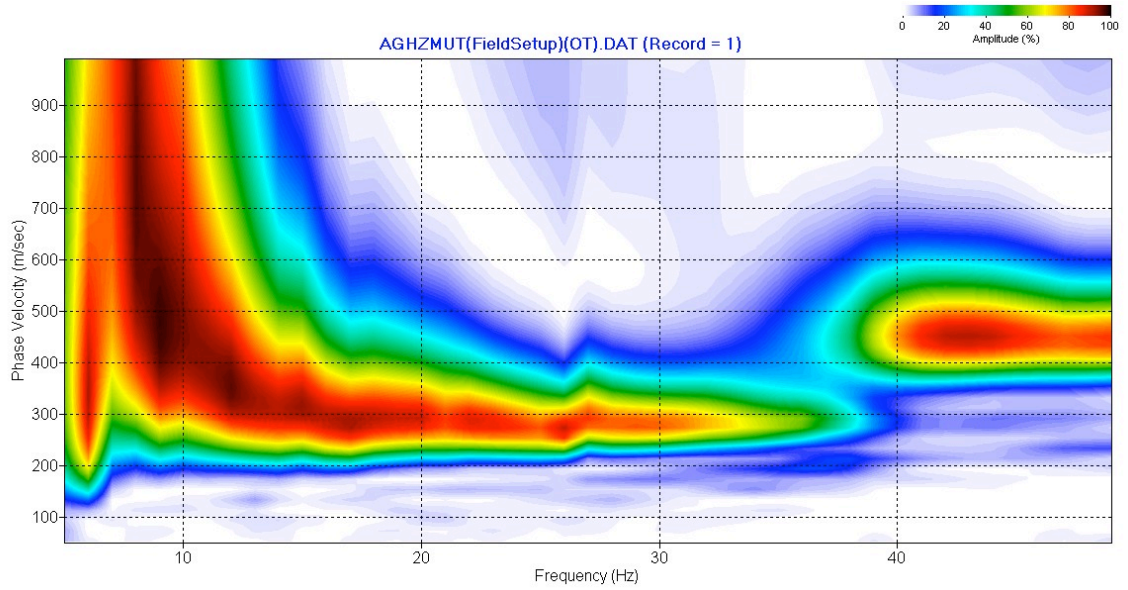
d) For passive source files only: Searching angle

1) De-select searching quadrants if van moved in-line with array

2) Off-line distance: 0

3) Select direction of In-line wave propagation

A)



B)

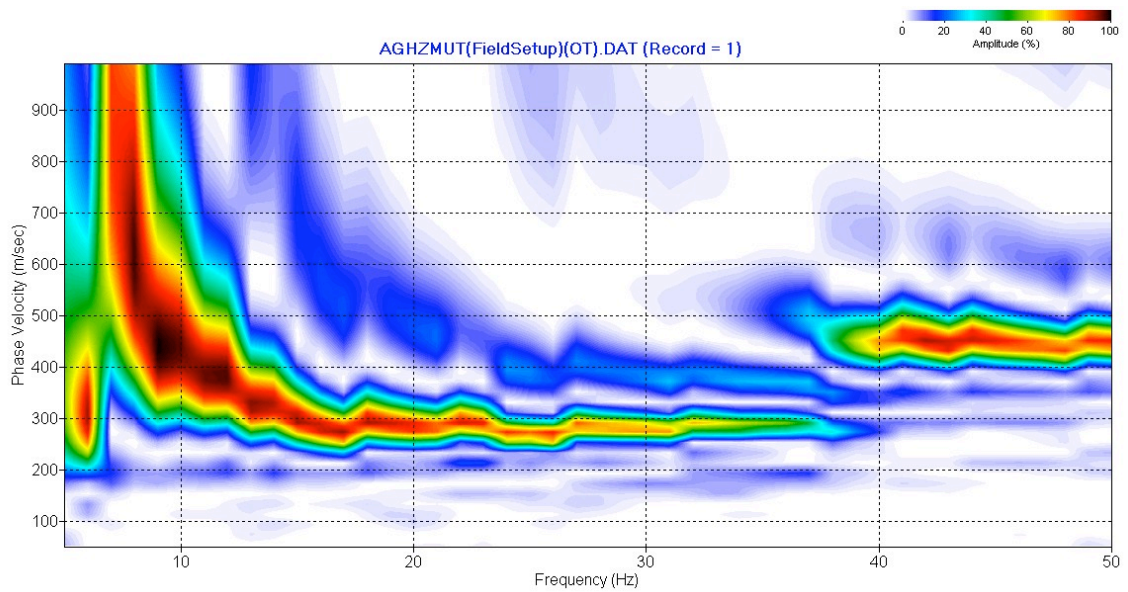
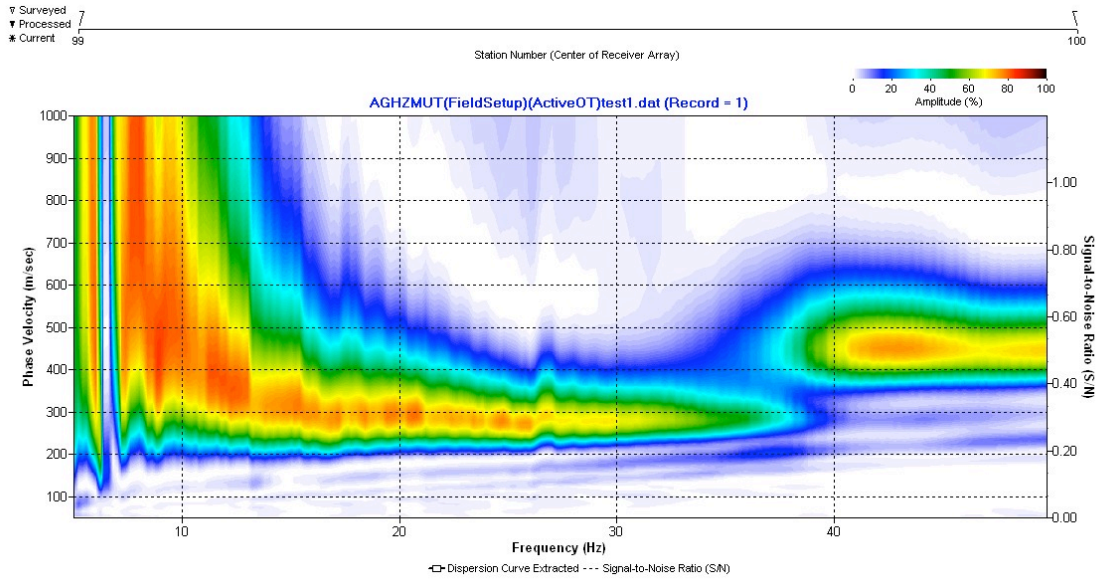


Figure A2: Overtone images (amplitude contour plots) generated with Dispersion 1; (A) approximate algorithm, (B) normal algorithm.

A)



B)

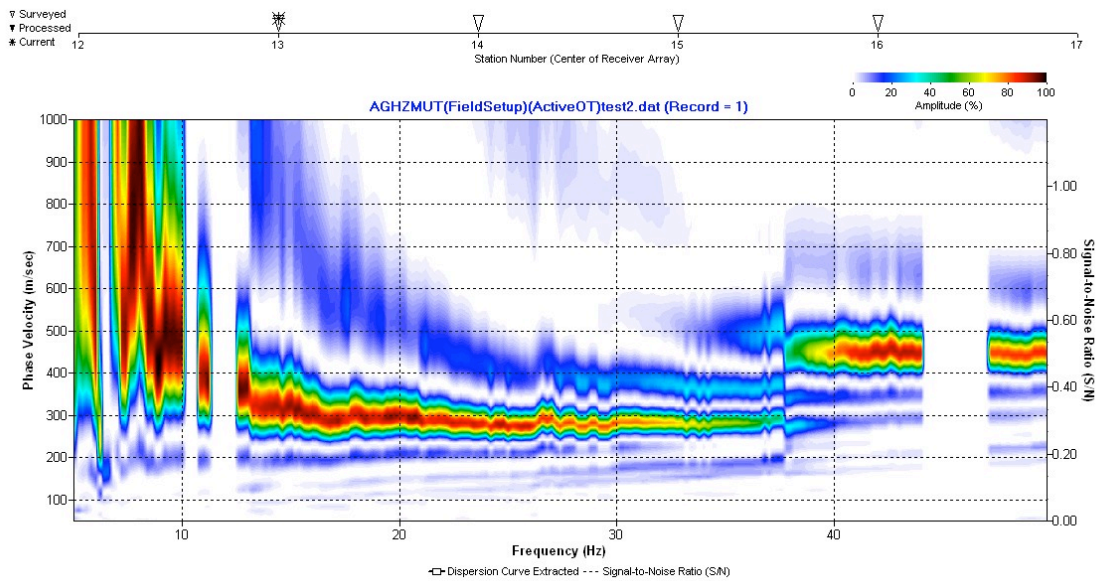


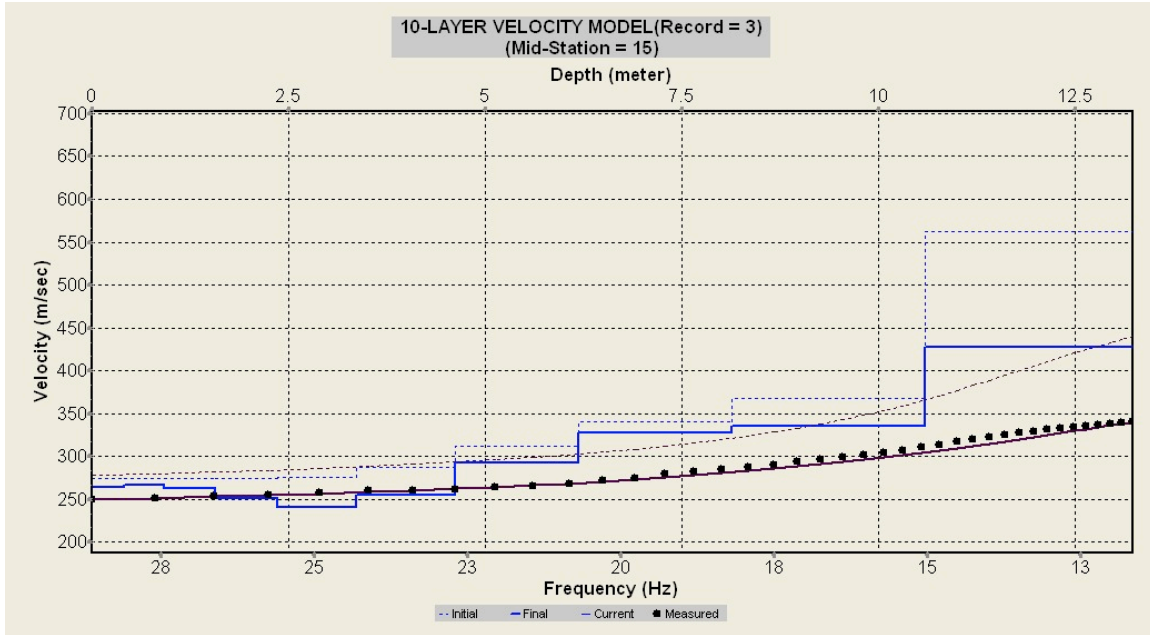
Figure A3: Overtone images (amplitude contour plots) generated with Dispersion 2; (A) normal algorithm, (B) advanced algorithm.

APPENDIX B

1-D SHEAR WAVE VELOCITY MODELS FOR INTERSECTION POINTS

Figures B1-B13 below show comparisons of the two 1-D shear wave velocity models for the intersection point of two perpendicular seismic lines.

A)



B)

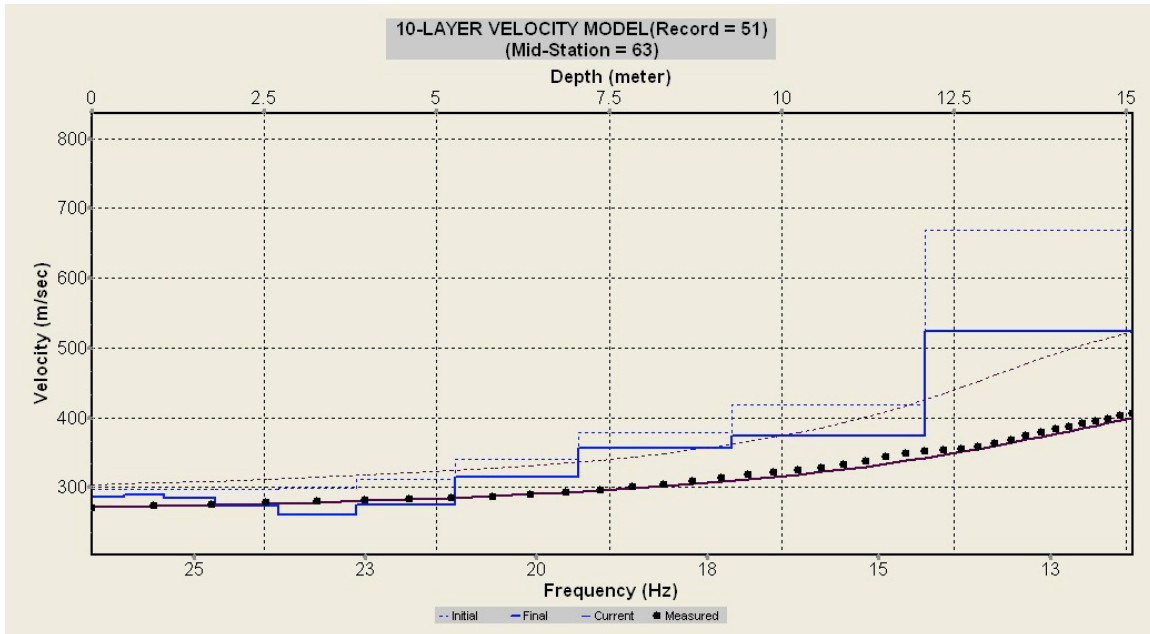
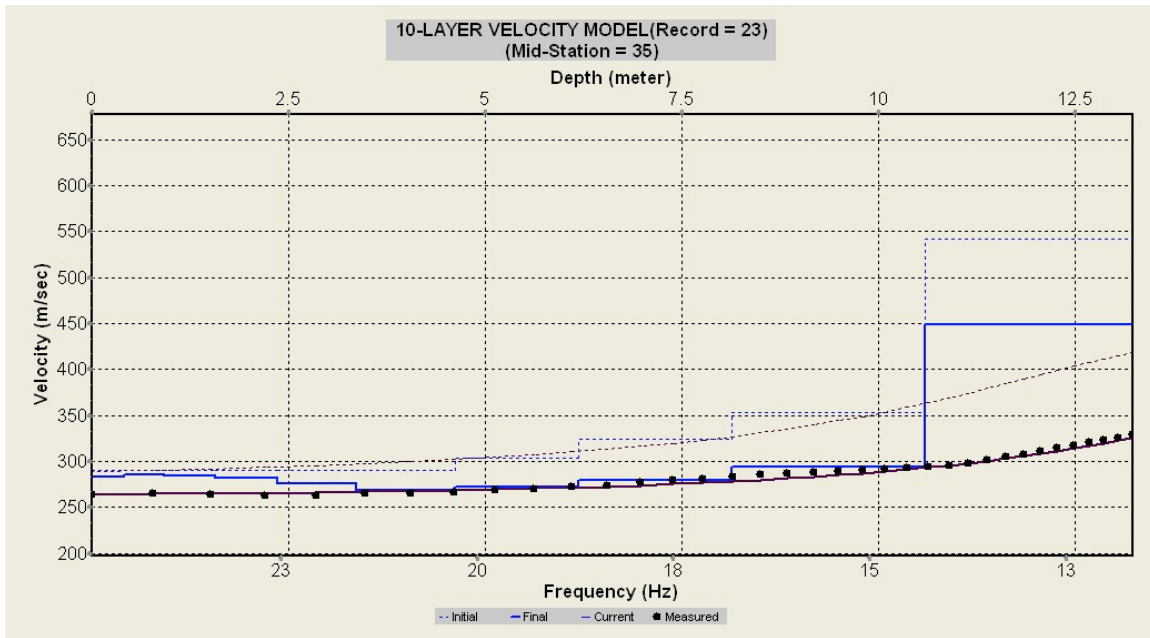


Figure B1: 1-D shear-wave velocity models for the intersection of Line Y and C; (A) STA Y15, (B) STA C63.

A)



B)

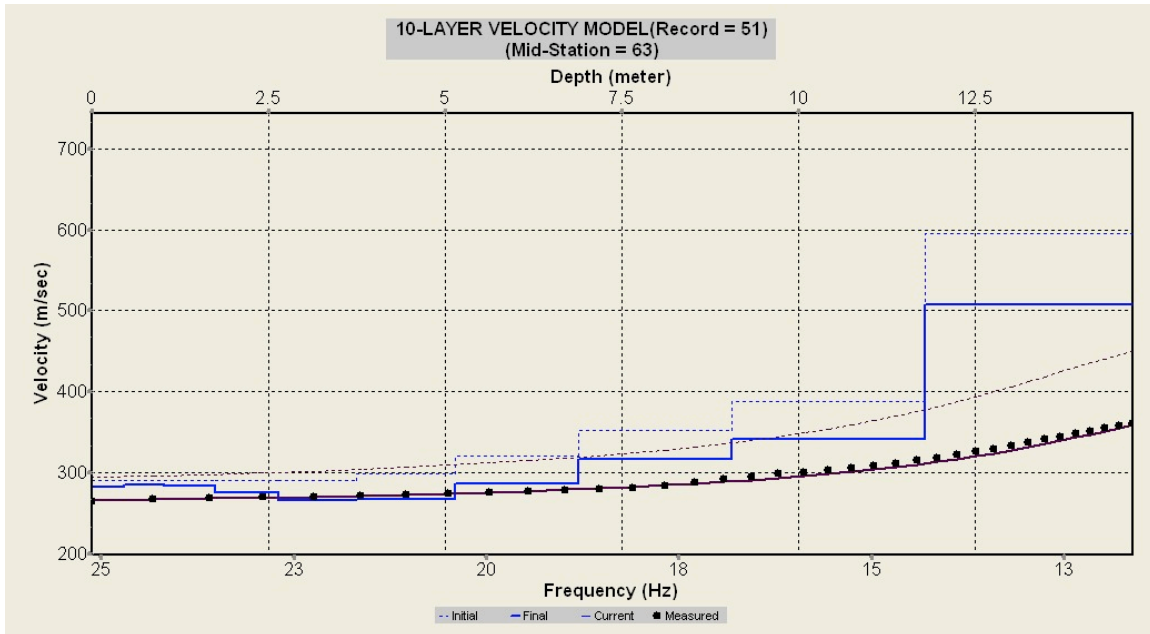
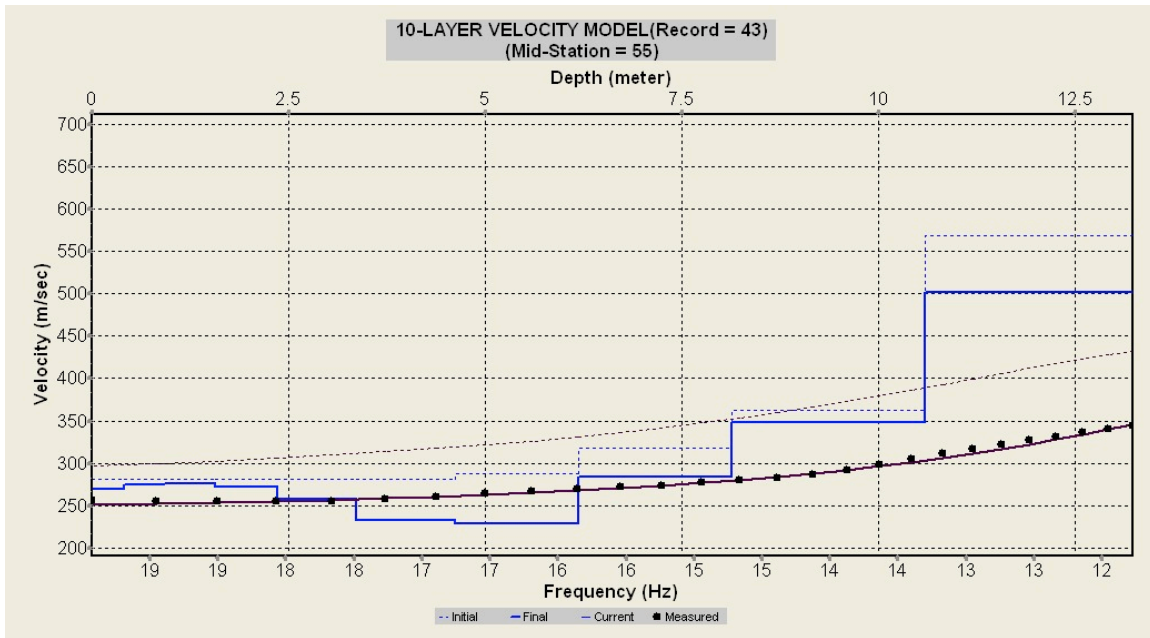


Figure B2: 1-D shear-wave velocity models for the intersection of Lines Y and B; (A) STA Y35, (B) STA B63.

A)



B)

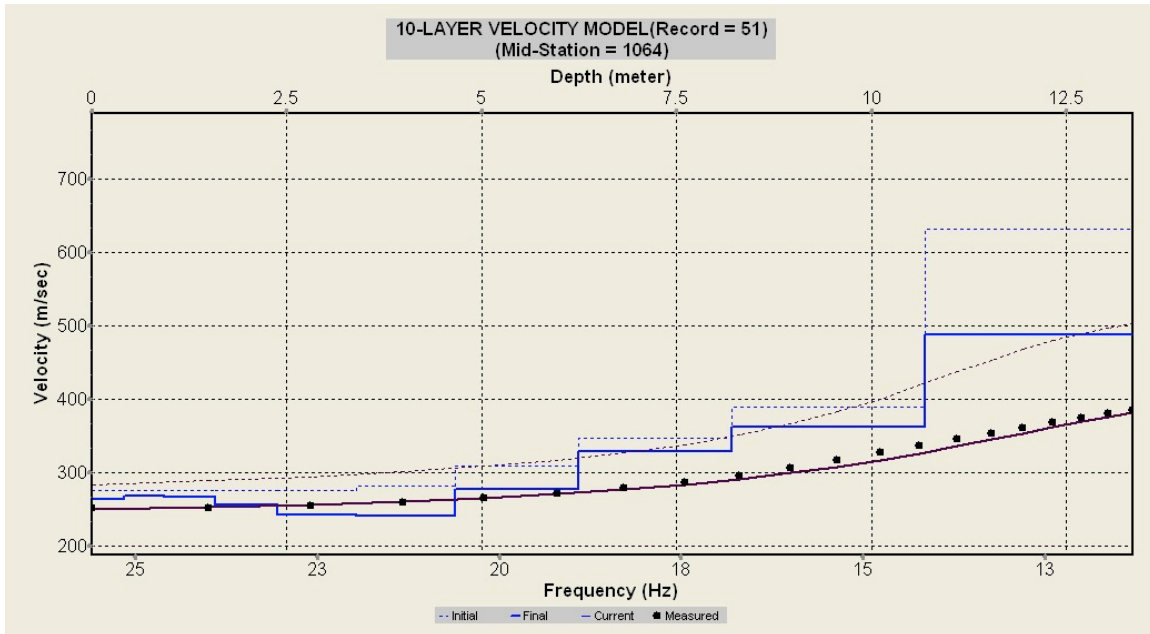
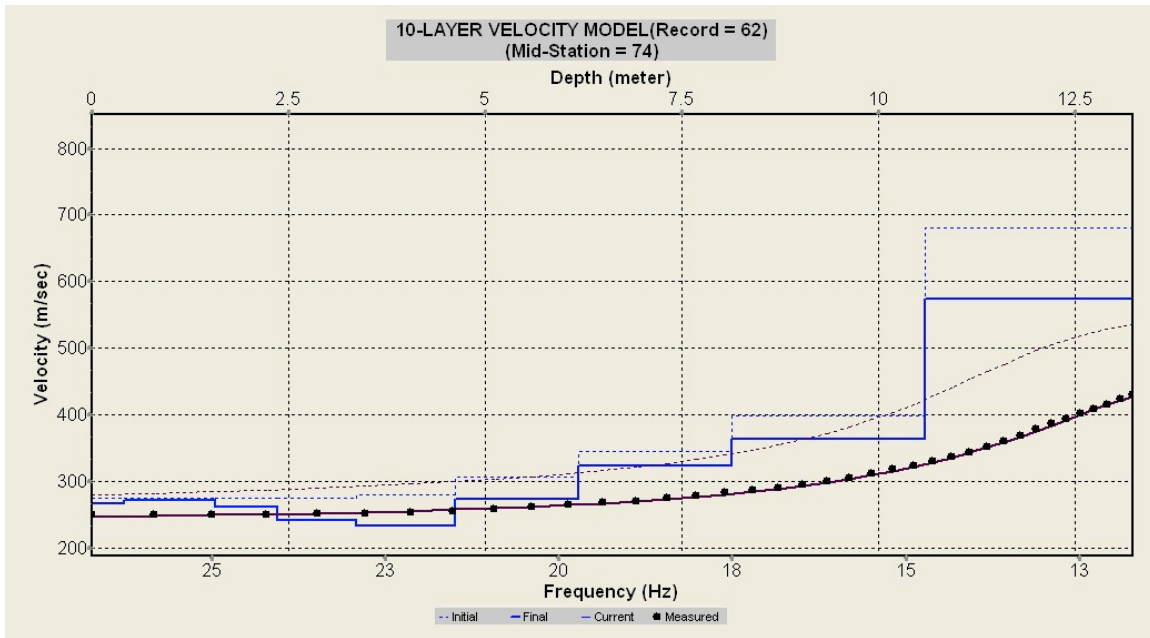


Figure B3: 1-D shear-wave velocity models for the intersection of Lines Y and A; (A) STA Y55, (B) STA A64.

A)



B)

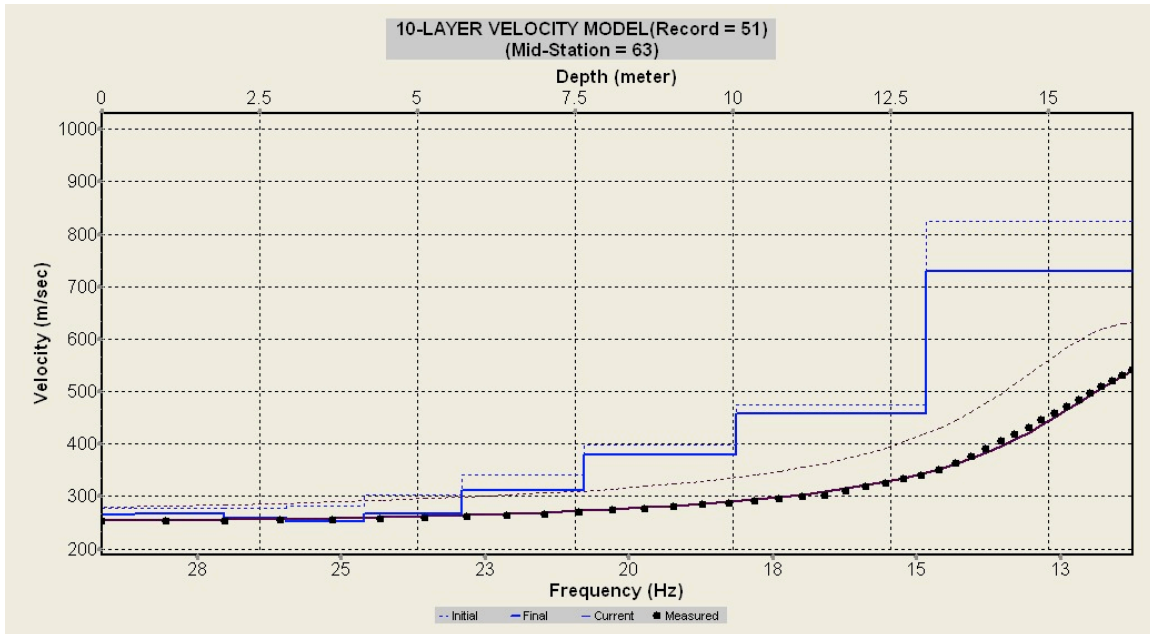
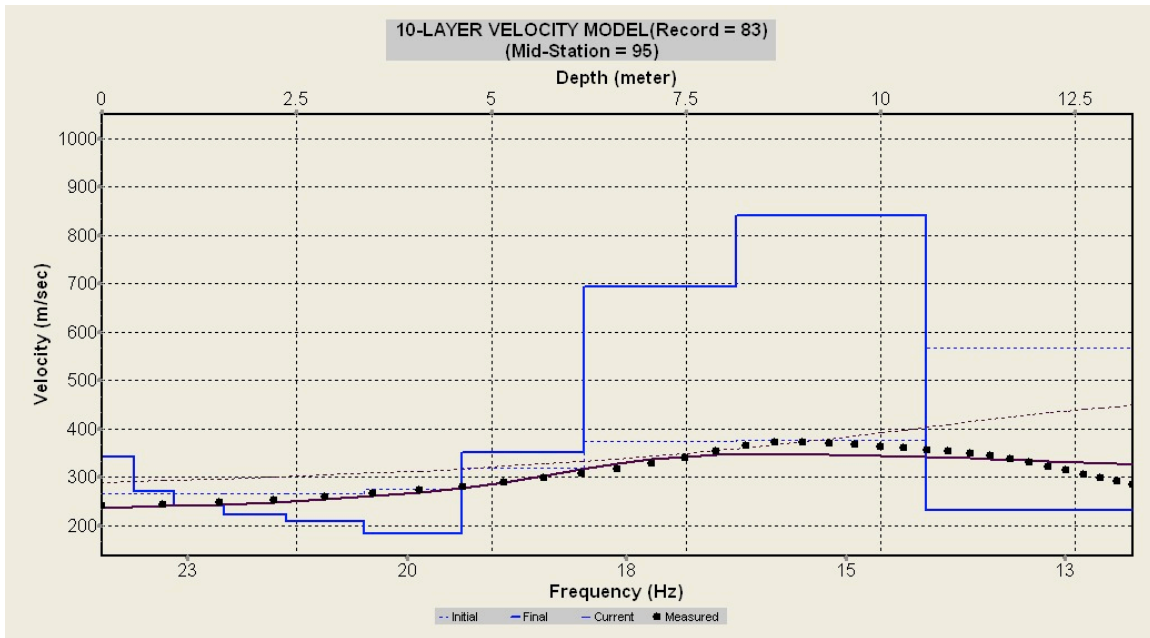


Figure B4: 1-D shear-wave velocity models for the intersection of Lines Y and D; (A) STA Y74, (B) STA D63.

A)



B)

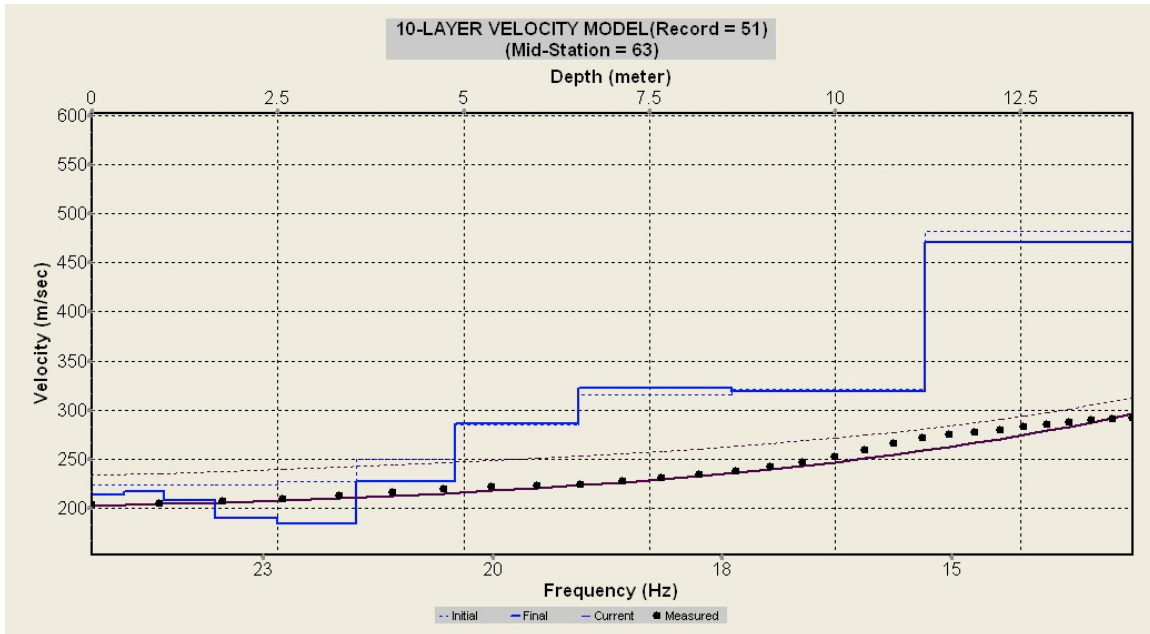
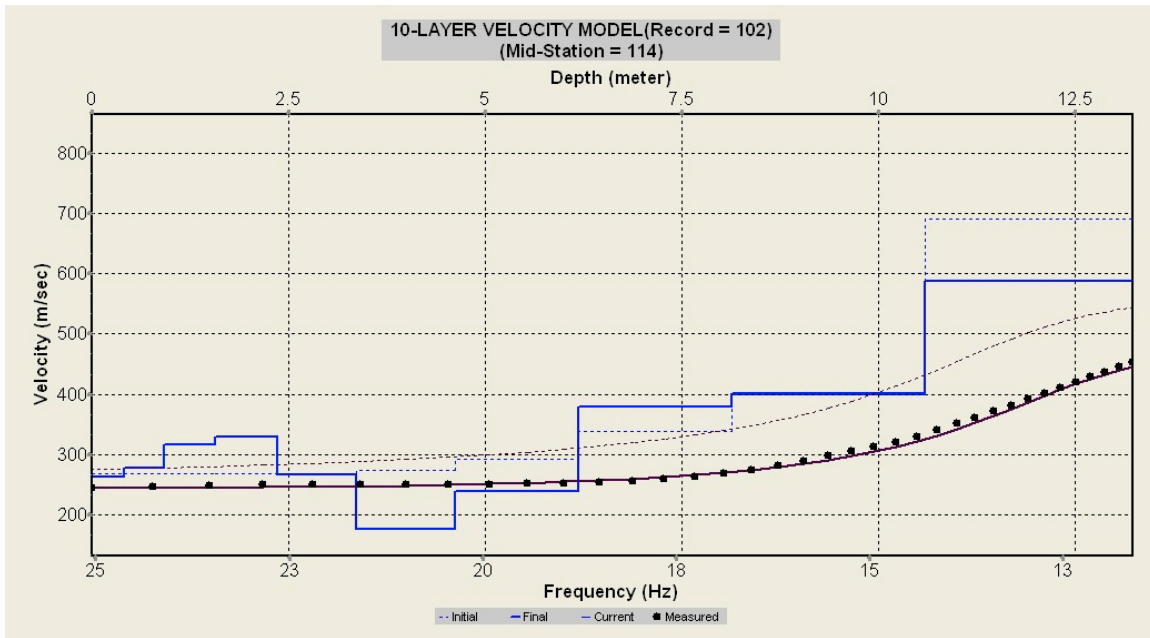


Figure B5: 1-D shear-wave velocity models for the intersection of Lines Y and E; (A) STA Y95, (B) STA E63.

A)



B)

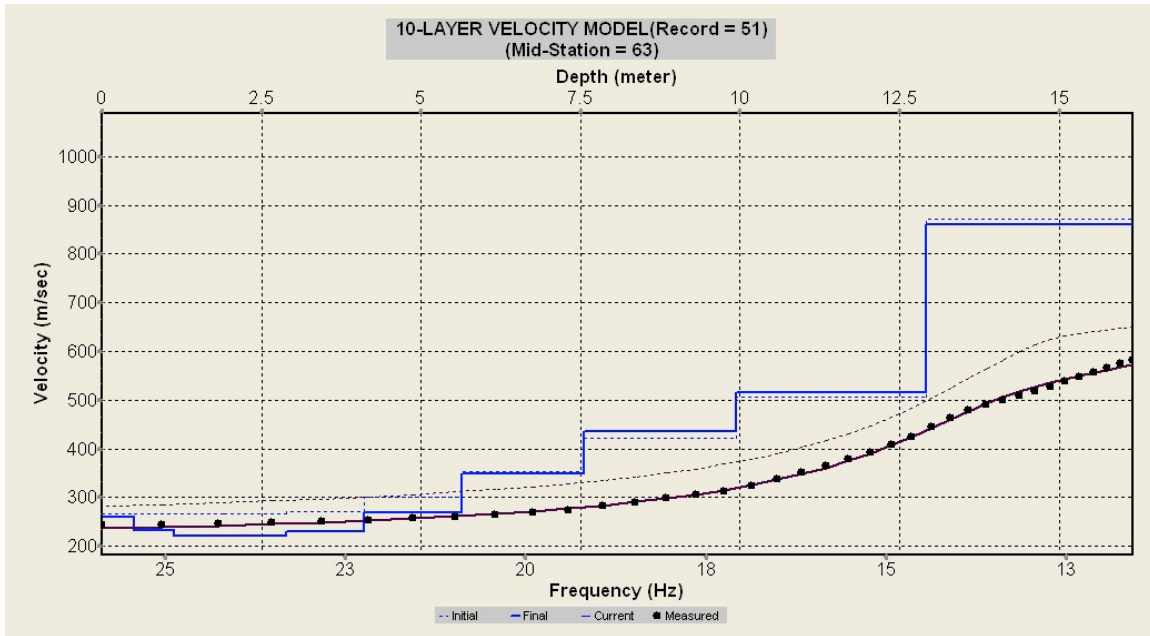
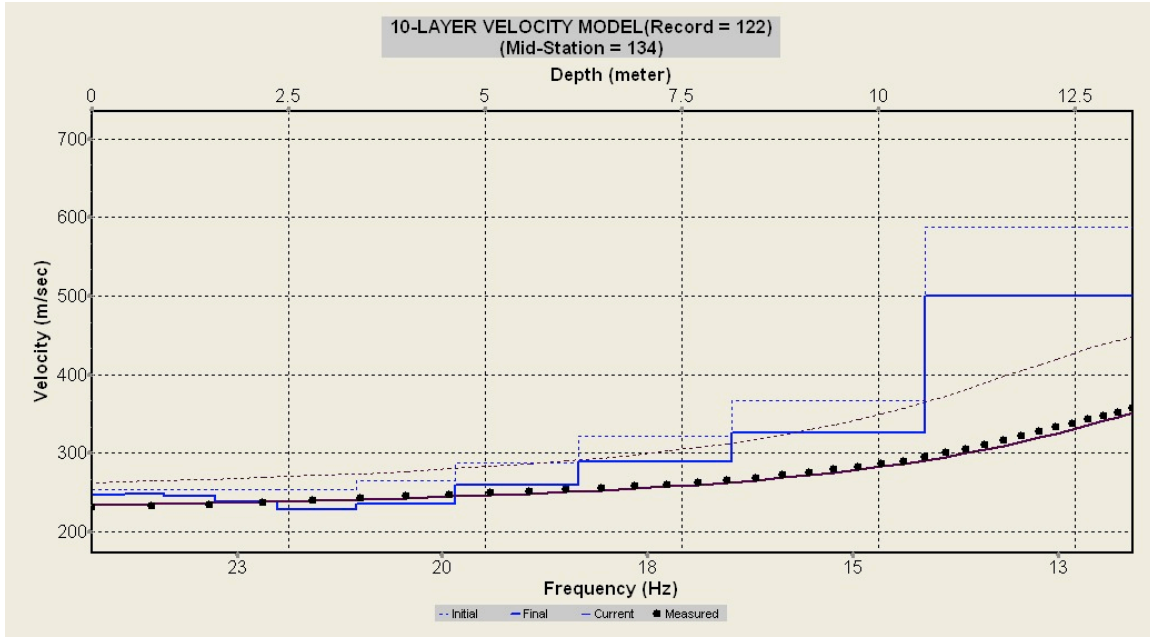


Figure B6: 1-D shear-wave velocity models for the intersection of Lines Y and F; (A) STA Y114, (B) STA F63.

A)



B)

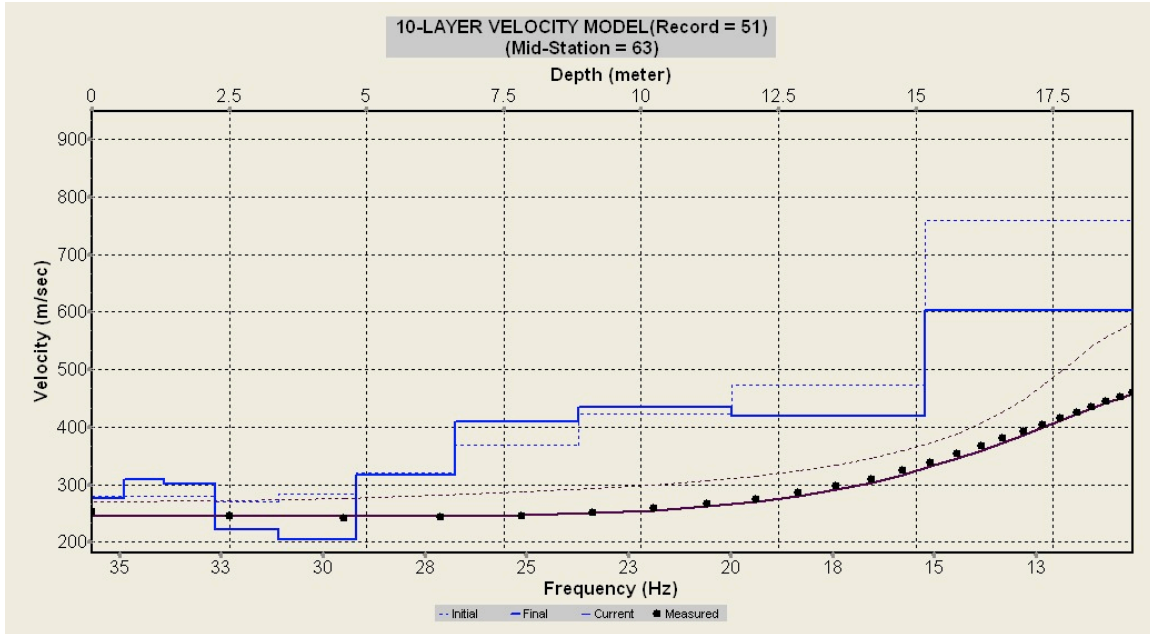
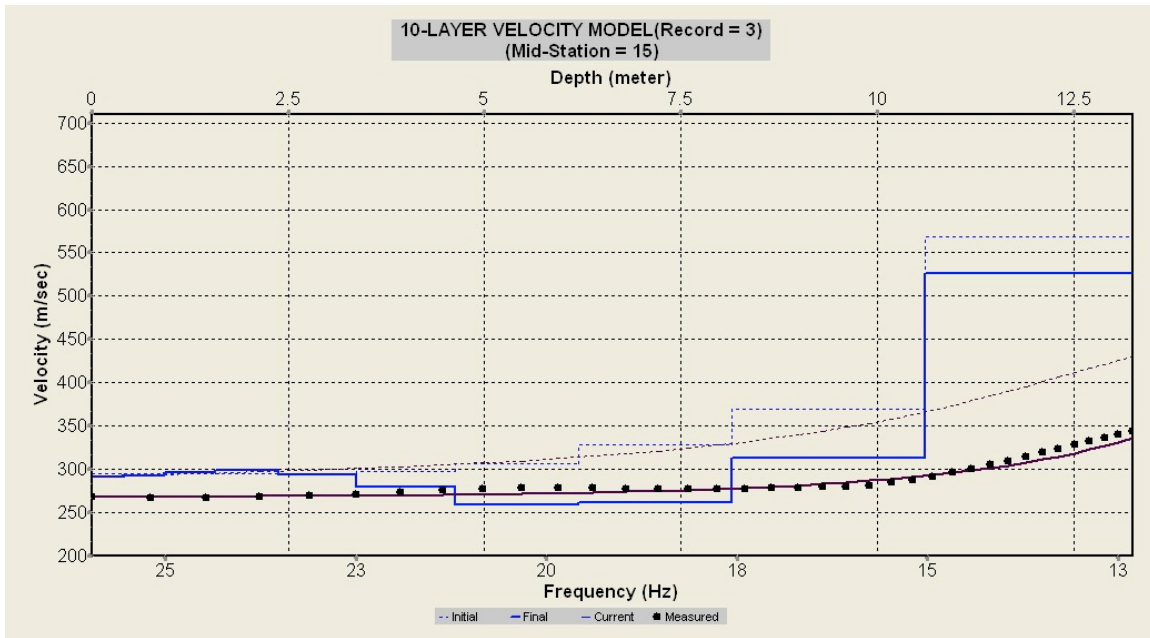


Figure B7: 1-D shear-wave velocity models for the intersection of Lines Y and G; (A) STA Y134, (B) STA G63.

A)



B)

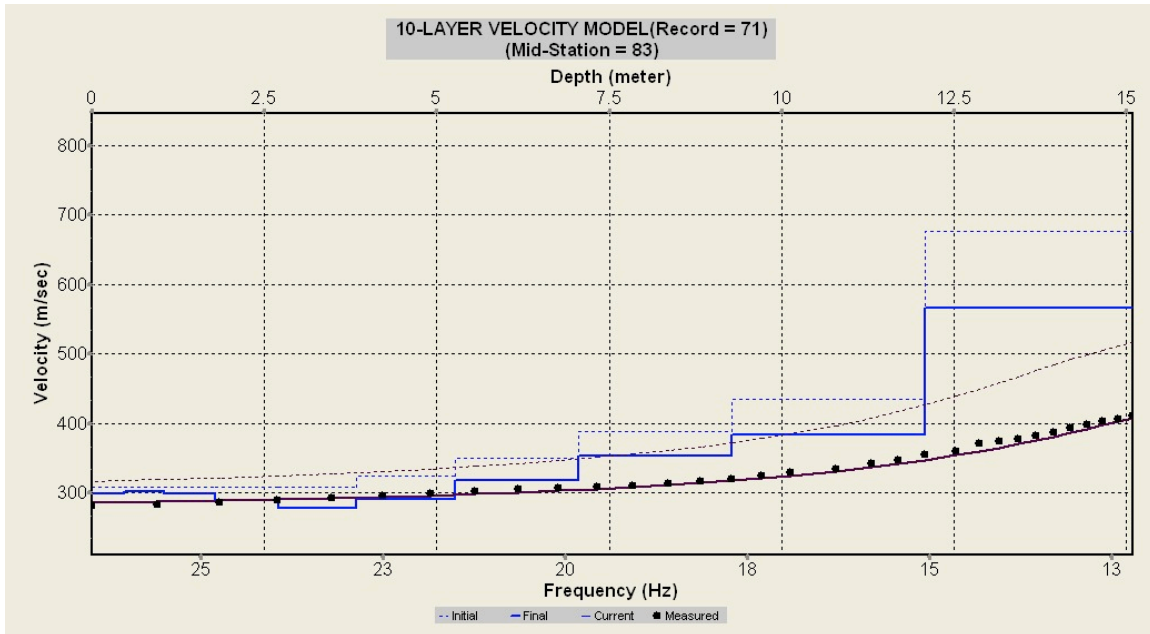
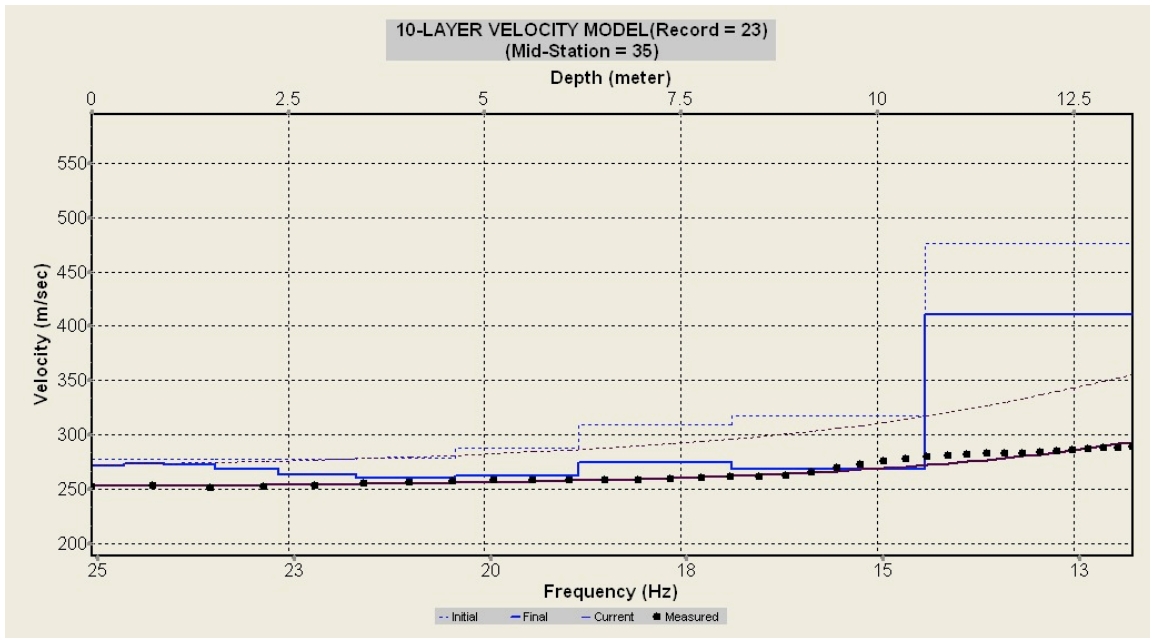


Figure B8: 1-D shear-wave velocity models for the intersection of Lines Z and C; (A) STA Z15, (B) STA C83.

A)



B)

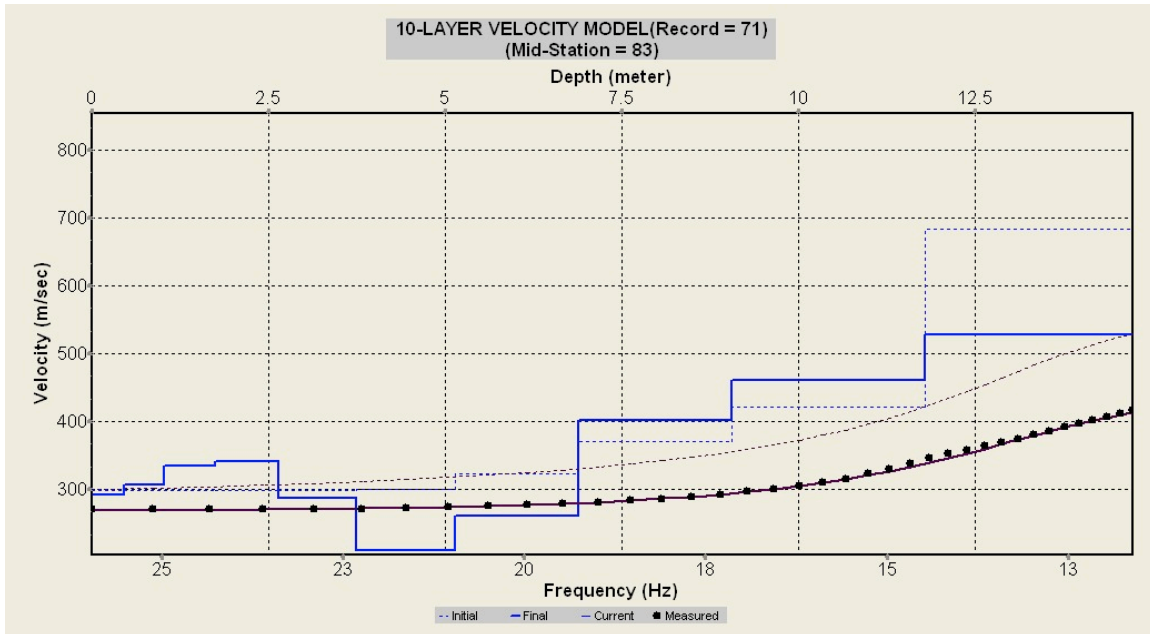
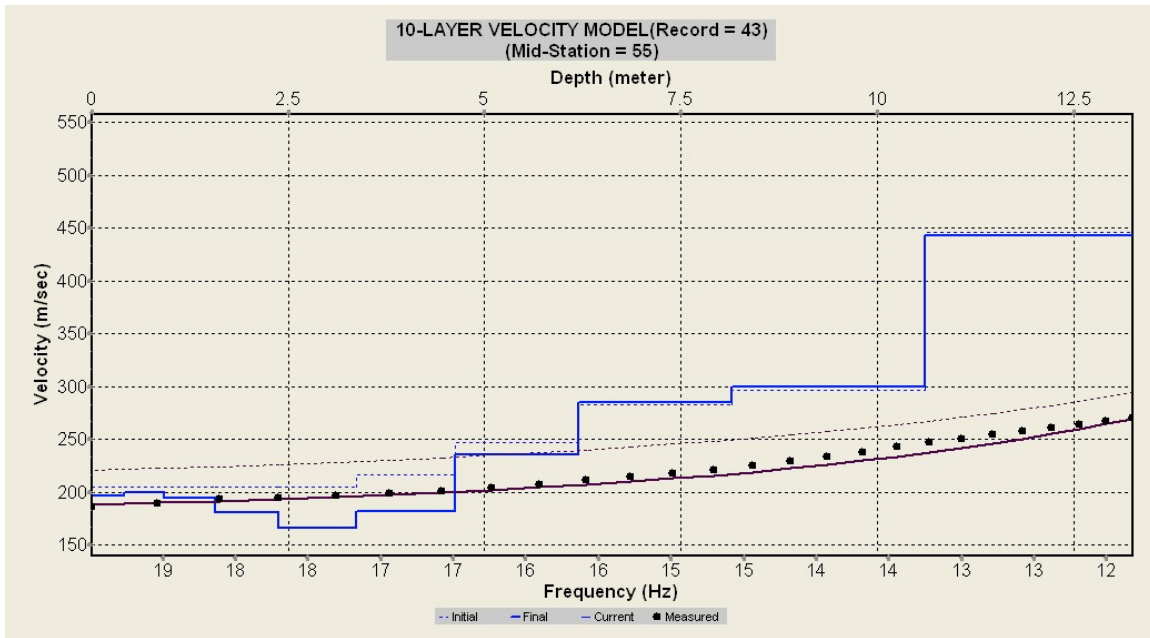


Figure B9: 1-D shear-wave velocity models for the intersection of Lines Z and B; (A) STA Z35, (B) STA B83.

A)



B)

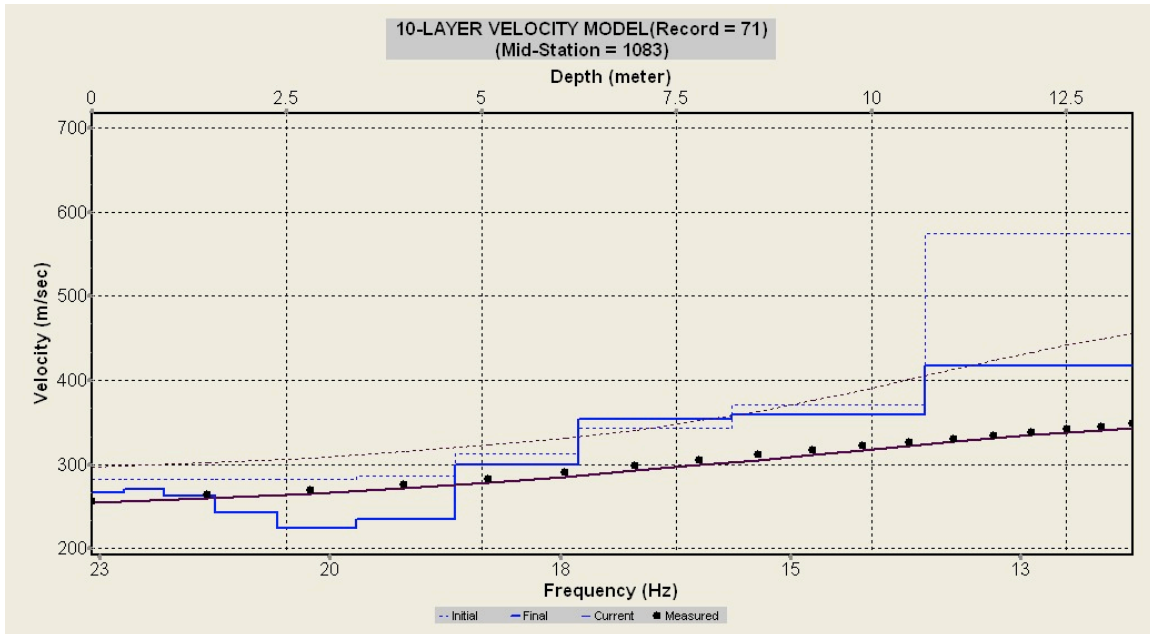
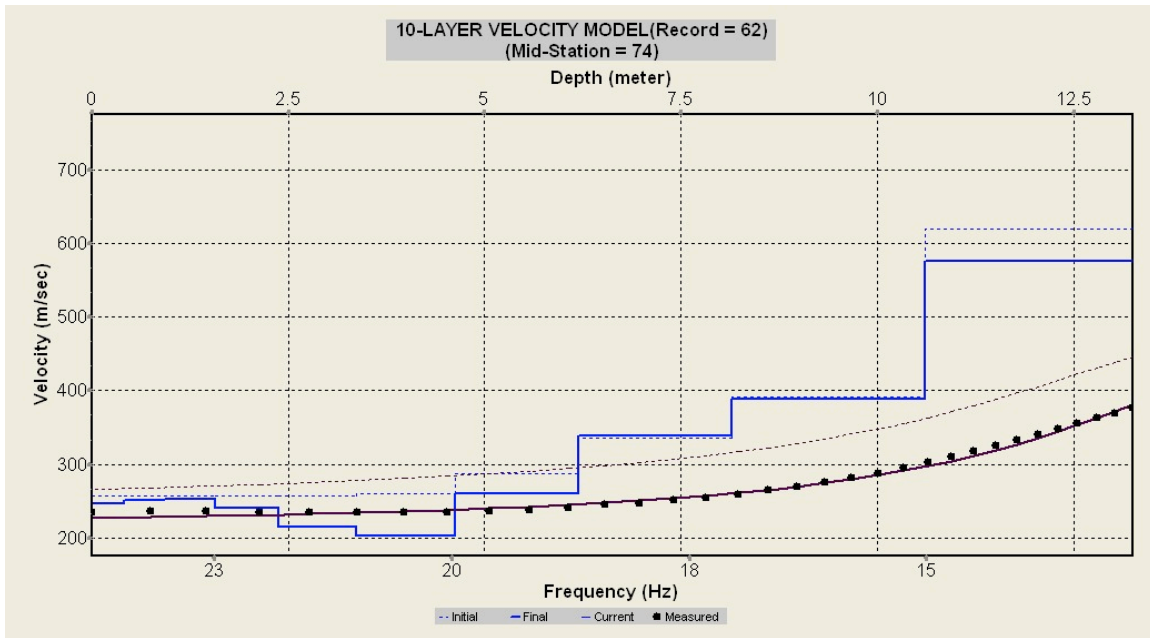


Figure B10: 1-D shear-wave velocity models for the intersection of Lines Z and A; (A) STA Z55, (B) STA A83.

A)



B)

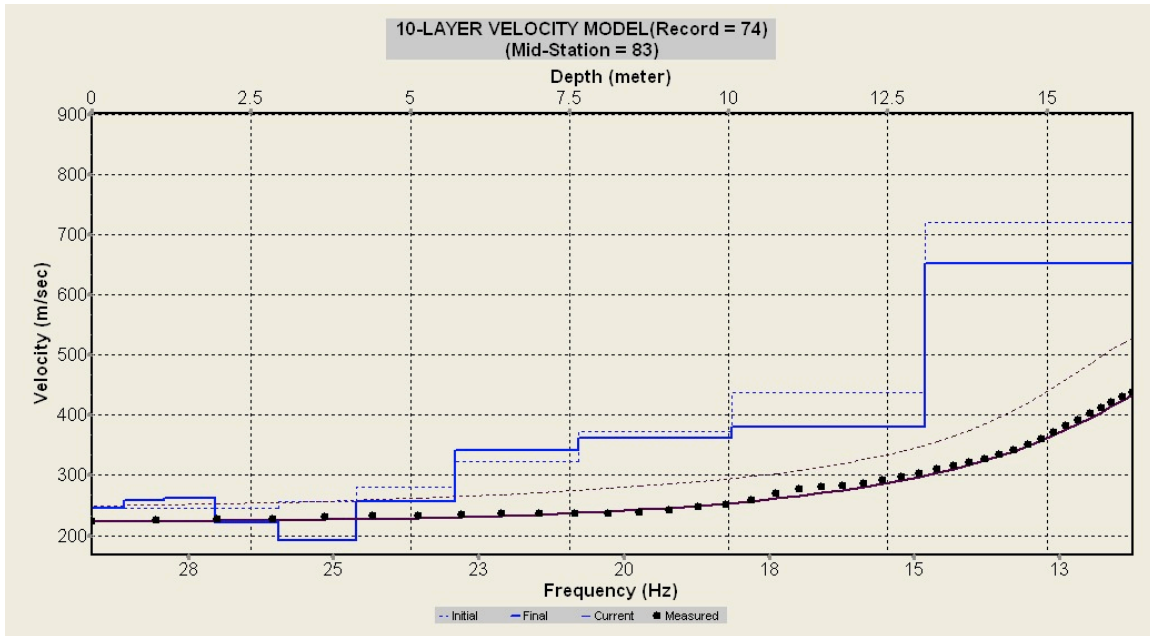
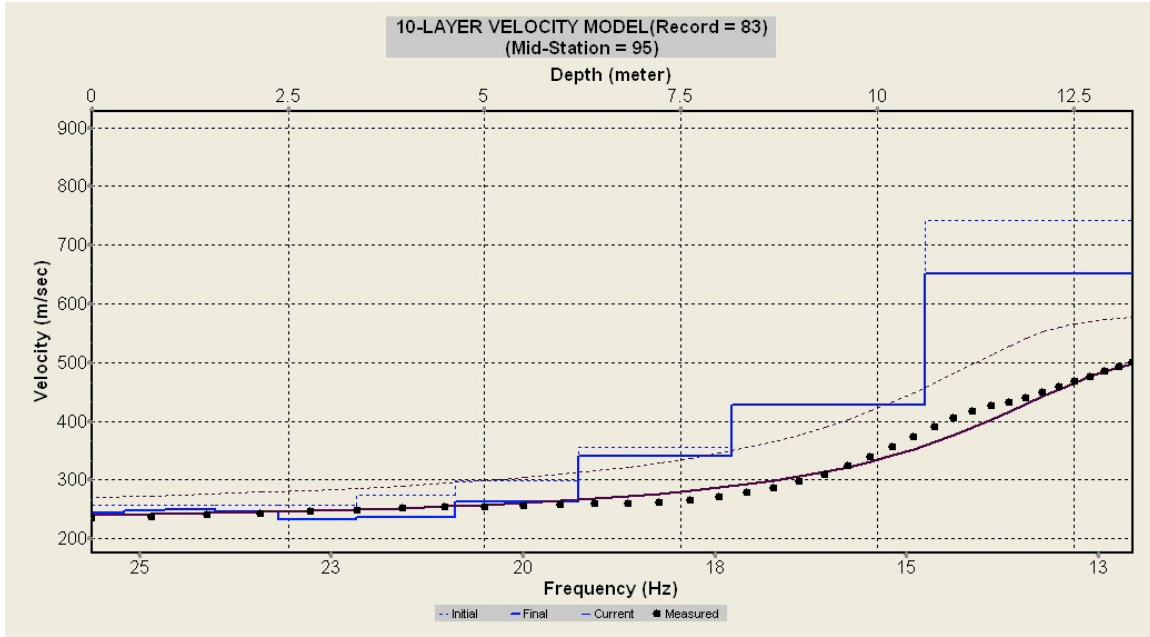


Figure B11: 1-D shear-wave velocity models for the intersection of Lines Z and D; (A) STA Z74, (B) STA D83.

A)



B)

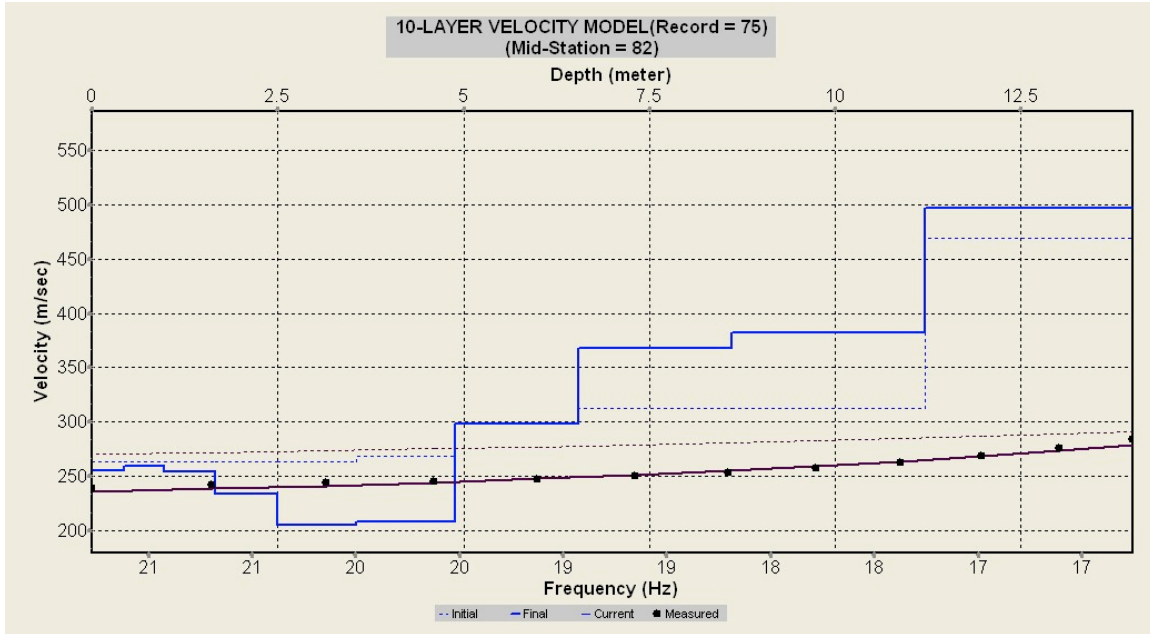
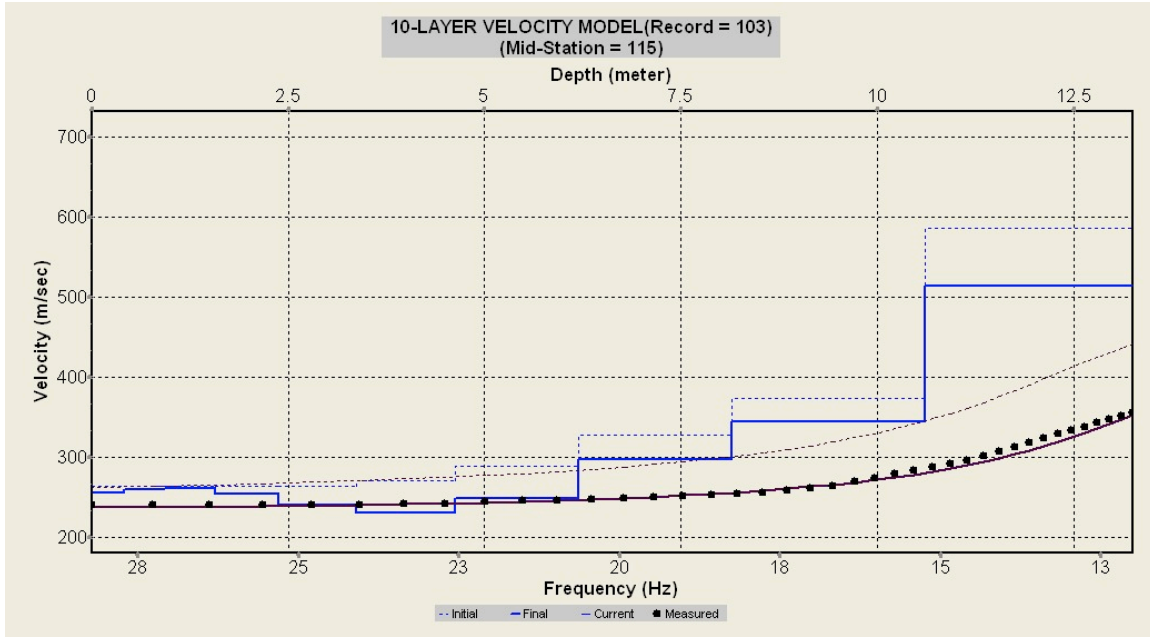


Figure B12: 1-D shear-wave velocity models for the intersection of Lines Z and E; (A) STA Z95, (B) STA E82.

A)



B)

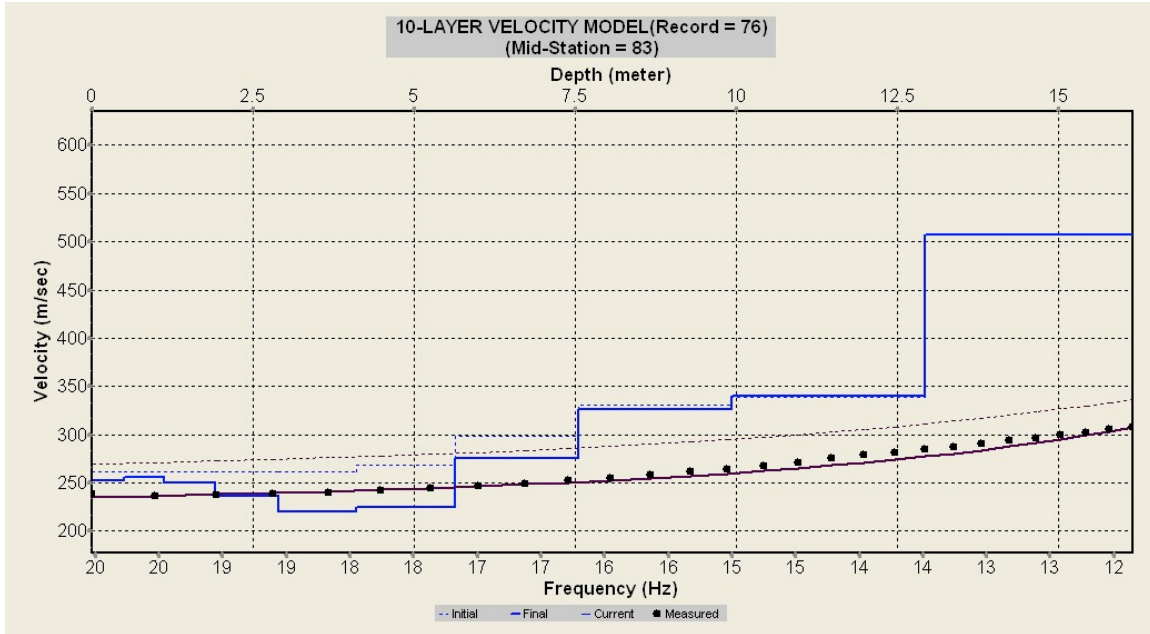


Figure B13: 1-D shear-wave velocity models for the intersection of Lines Z and F; (A) STA Z115, (B) STA F83.